NASA Contractor Report 198534

Reynolds-Averaged Navier-Stokes Studies of Low Reynolds Number Effects on the Losses in a Low Pressure Turbine

Daniel J. Dorney
Western Michigan University
Kalamazoo, Michigan

September 1996

Prepared for
Lewis Research Center
Under Grant NAG3–1668

National Aeronautics and
Space Administration

Contents

List of Tables

List of Figures

NOMENCLATURE

e_t - Total energy
M - Mach number
P - Static pressure
q - Magnitude of the velocity
Re - Inlet reference Reynolds number
T - Static temperature
u, v - x, y components of velocity
α - Absolute flow angle
β - Relative flow angle
ρ - Density
τ - Shear stress
Ω - Rotor rotational speed

SUBSCRIPTS

k - Kinetic energy
rel - Relative reference frame quantity
t - Stagnation quantity
T - Turbulent quantity
w - Wall quantity
x, y - Partial derivative with respect to x, y
ϵ - Turbulent dissipation

ABSTRACT

Experimental data from jet-engine tests have indicated that unsteady blade-row interaction effects can have a significant impact on the efficiency of low-pressure turbine stages. Measured turbine efficiencies at takeoff can be as much as two points higher than those at cruise conditions. Preliminary studies indicate that Reynolds number effects may contribute to the lower efficiencies at cruise conditions. In the current study, numerical experiments have been performed to quantify the Reynolds number dependence of unsteady wake/separation bubble interaction on the performance of a low-pressure turbine.

INTRODUCTION

The need for an improved understanding of efficiency variations in multiple blade row turbines has motivated engineers to assess the effects of unsteady aerodynamic interaction on the performance of turbomachinery components. The two principal types of aerodynamic interaction are usually referred to as potential-flow and wake interaction. Potential-flow interaction results from the variations in the velocity potential or pressure fields associated with the blades of a neighboring row, and their effect upon the blades of a given row moving at a different rotational speed. This type of interaction is of serious concern when the axial spacing between adjacent blade rows is small or the axial flow Mach number is high. Wake interaction is the effect upon the flow through a downstream blade row of the vortical and entropic wakes shed by one or more upstream rows.

The focus of the current effort is to use a viscous, unsteady Navier-Stokes analysis to study the effects of Reynolds number variation on the interaction of blade wakes and separation bubbles in a low-pressure turbine blade passage. The change in the efficiency as a function of Reynolds number and separation bubble behavior has been investigated.

NUMERICAL PROCEDURE

Governing Equations

The field equations considered in this investigation are the time-dependent Navier-Stokes equations. These equations can be written in non-dimensional form, and in terms of body-fitted coordinates, as

$$Q_\tau + \left(F_i + Re^{-1}F_v\right)_\xi + \left(G_i + Re^{-1}G_v\right)_\eta = 0 \tag{1}$$

where the subscripts i refer to inviscid quantities, the subscripts v refer to viscous quantities, the subscripts ξ and η refer to derivatives with respect to the body-fitted coordinate directions, and Re is the Reynolds number. The vector of conserved variables is

$$Q = J\bar{Q} \tag{2}$$

and the inviscid flux vectors are

$$F_i = J(\xi_t\bar{Q} + \xi_x\bar{F}_i + \xi_y\bar{G}_i) \tag{3}$$

$$G_i = J(\eta_t\bar{Q} + \eta_x\bar{F}_i + \eta_y\bar{G}_i) \tag{4}$$

The Jacobian of the transformation (from physical Cartesian (x, y) to computational curvilinear (ξ, η) coordinates) and the other metric quantities are given by

$$J = x_\xi y_\eta - y_\xi x_\eta \tag{5}$$

$$\xi_x = y_\eta / J, \quad \xi_y = -x_\eta / J, \quad \eta_x = -y_\xi / J, \quad \eta_y = x_\xi / J \tag{6}$$

In the Cartesian coordinate frame, the conserved variable and inviscid flux vectors are defined as

$$\begin{aligned} \bar{Q} &= [\rho, \rho u, \rho v, e_t]^T \\ \bar{F}_i &= \left[\rho u, \rho u^2 + P, \rho uv, (e_t + P)u\right]^T \\ \bar{G}_i &= \left[\rho v, \rho uv, \rho v^2 + P, (e_t + P)v\right]^T \end{aligned} \tag{7}$$

where ρ is the density, u and v are the Cartesian velocity components, P is the thermodynamic pressure, and e_t is the total internal energy.

The governing equations can be simplified by incorporating the thin-layer assumption [1]. The thin-layer assumption assumes that the viscous flux terms parallel to a solid surface are negligible with respect to the viscous terms normal to the surface. Thus, for two-dimensional turbomachinery applications, the viscous terms in the direction normal to the blade surface (η direction) are retained,

$$Q_\tau + (F_i)_\xi + \left(G_i + Re^{-1} G_v\right)_\eta = 0 \tag{8}$$

The viscous flux vector, G_v, in Eqn. 8 is given by

$$G_v = - \begin{bmatrix} 0 \\ K_1 u_\eta + K_2 \eta_x \\ K_1 v_\eta + K_2 \eta_y \\ K_1 \left[P_r^{-1} (\gamma - 1)^{-1} (a^2)_\eta \right. \\ \qquad \left. + (q^2/2)_\eta\right] + K_2 K_3 \end{bmatrix} \tag{9}$$

$$\begin{aligned} K_1 &= \mu \left(\eta_x{}^2 + \eta_y{}^2\right) \\ K_2 &= \frac{\mu}{3} \left(\eta_x u_\eta + \eta_y v_\eta\right) \\ K_3 &= u\eta_x + v\eta_y \\ q^2 &= u^2 + v^2 \end{aligned} \tag{10}$$

where μ is the dynamic viscosity, P_r is the Prandtl number, and a is the speed of sound. In the current study, both the thin-layer and full Navier-Stokes equations have been utilized.

Solution Algorithm

The implicit numerical procedure used in this study, consists of a time-marching finite-difference scheme [2, 3, 4]. The procedure is second-order temporally accurate and third-order

spatially accurate. The inviscid fluxes are discretized according to either the scheme developed by Chakravarthy and Osher [5] or that of Roe [6]. The viscous fluxes are discretized using standard central differences. An alternating direction, approximate-factorization technique is used to compute the time-rate changes in the primary variables. Newton sub-iterations are used at each global time step to increase stability and reduce linearization errors. For typical unsteady simulations, two Newton sub-iterations are performed at each time step. The grid topology for the numerical procedure consists of O- and H-type overlaid grids.

BOUNDARY CONDITIONS

Inlet, Exit, and Surface Boundary Conditions

The inlet, exit, and surface boundary conditions used in this study are based on a characteristic analysis of the linearized Euler equations. For viscous flows, it is assumed that the computational inlet and exit are in regions where the flow is predominantly inviscid, and the characteristic boundary conditions are retained. No-slip boundary conditions are enforced at solid surfaces for viscous flows, along with either a specified wall temperature or heat flux distribution.

In the computational procedure, quasi-two-dimensional characteristic boundary conditions are solved implicitly along with the interior of the computational domain. After each time step, fully two-dimensional unsteady boundary conditions can be explicitly applied at the inlet and exit boundaries to improve solution accuracy. Further information describing the inlet, exit, and surface boundary conditions can be found in Giles [7] and Dorney and Davis [3].

Zonal Boundary Conditions

In the numerical analysis, the use of overlaid grids requires the application of zonal boundary conditions. Dirichlet conditions, in which the time rate change in the conserved vector Q is set to zero, are imposed at the overlaid boundaries of the O- and H-type grids. The flow variables of Q at the zonal boundaries are explicitly updated after each time step by interpolating values from the adjacent grid. Because of the explicit application of the zonal boundary conditions, large time steps necessitate the use of more than one Newton sub-iteration to maintain time accuracy. The accuracy of the information transfer between adjacent grids can also be enhanced by increasing the amount of overlap between the O- and H-grids. The zonal boundary conditions are non-conservative, but the current implementation has been shown to yield satisfactory results even for transonic and supersonic flows [3, 8]. Further information describing the zonal boundary conditions can be found in Rai [4, 9].

TURBULENCE AND TRANSITION MODELS

Two turbulence models are utilized in the numerical procedure; an algebraic model and a model based on the solution of two partial differential equations. Several correlations are available in the analysis for predicting natural and bubble transition.

Baldwin-Lomax Model

In the algebraic, two-layer Baldwin-Lomax (B-L) turbulence model, the eddy viscosity is described by [1]

$$\mu_T = \begin{cases} \mu_{T\text{inner}} & s \leq s_{\text{crossover}} \\ \mu_{T\text{outer}} & s > s_{\text{crossover}} \end{cases} \tag{11}$$

where s is the distance normal to the solid surface and $s_{crossover}$ is the smallest value at which $\mu_{T_{inner}} = \mu_{T_{outer}}$.

In the inner region, the eddy viscosity is calculated using the Prandtl-Van Driest formulation

$$\mu_{T_{inner}} = \rho l^2 |\omega|^2 \tag{12}$$

where l is the mixing length given by

$$l = ks\left[1 - \exp(-y^+/A^+)\right] \tag{13}$$

and k and A^+ are constants. While formulae exist for modifying k and A^+ for the presence of pressure gradients and surface roughness (see Granville [10] for a review), constant values are used here for simplicity. The magnitude of the vorticity, $|\omega|$, can be written in two-dimensions, for example, as

$$|\omega| = |u_y - v_x| \tag{14}$$

and y^+ is the law-of-the-wall coordinate

$$y^+ = \frac{\sqrt{\rho_w \tau_w} s}{\mu_w} \tag{15}$$

In the outer region the eddy viscosity is calculated using

$$\mu_{T\text{outer}} = K C_{cp} \rho F_{\text{wake}} F_{\text{Kleb}}(s) \tag{16}$$

where K is the Clauser constant, C_{cp} is an additional constant, and F_{wake} is described by

$$F_{\text{wake}} = \min\left(s_{\max} F_{\max}, C_{\text{wk}} s_{\max} {q_{\text{dif}}}^2 / F_{\max}\right) \tag{17}$$

The term $F_{\max}$ is the maximum value of $F(s)$ along a given computational grid line normal to the surface and

$$F(s) = s|\omega|\left[1 - \exp\left(-y^+/A^+\right)\right] \tag{18}$$

The Klebanoff intermittency factor, $F_{\text{Kleb}}(s)$ is given by

$$F_{\text{Kleb}}(s) = \left[1 + 5.5((sC_{\text{Kleb}})/s_{\max})^6\right]^{-1} \tag{19}$$

and q_{dif} is the difference between the maximum and minimum total velocity in the profile. The constants used in the current implementation of the B-L turbulence model are

$$\begin{aligned} A^+ &= 26 \quad C_{cp} = 1.6 \\ C_{\text{Kleb}} &= 0.3 \quad C_{\text{wk}} = 0.25 \\ k &= 0.4 \quad K = .0168 \end{aligned} \tag{20}$$

Several researchers have developed correlations to modify the constants listed above [11, 12], but these relations are usually case-dependent and require significant adjustment by the user.

One modification that has been made to the B-L model is to apply a smoothing function to the predicted turbulent field for separated flow fields. Prudent use of the smoothing function has been found to eliminate non-physical gradients in the turbulence field [13].

The B-L model has two limitations which are of great consequence in turbomachinery simulations. First, the B-L model was designed for steady flow fields and does not contain time dependent terms (*i.e.,* convection effects cannot be modeled). Thus, the results of unsteady simulations using the B-L model must be interpreted with care. Second, the B-L model is not dependent on the free stream turbulence level. The free stream turbulence level can have a significant impact on the boundary layer and secondary flow development in turbomachines.

$k-\epsilon$ Model

The two-equation $k-\epsilon$ model, originally developed by Jones and Launder [14, 15], uses transport equations (based on the Navier-Stokes equations) for the kinetic energy (k) and turbulent dissipation (ϵ). The $k-\epsilon$ equations include the convection and upstream history of the turbulence, overcoming the major deficiencies of the B-L model.

The $k-\epsilon$ equations can be written in two dimensions as

$$\frac{\partial A}{\partial t}+\frac{\partial B}{\partial x}+\frac{\partial C}{\partial y}=\frac{1}{Re}\left(\frac{\partial M}{\partial x}+\frac{\partial N}{\partial y}++S\right) \tag{21}$$

where

$$A=\begin{bmatrix}\rho k\\ \rho e\end{bmatrix}\quad B=\begin{bmatrix}\rho uk\\ \rho ue\end{bmatrix} \tag{22}$$

$$C=\begin{bmatrix}\rho vk\\ \rho ve\end{bmatrix} \tag{23}$$

$$M=\begin{bmatrix}\mu_k\frac{\partial k}{\partial x}\\ \mu_\epsilon\frac{\partial \epsilon}{\partial x}\end{bmatrix}\quad N=\begin{bmatrix}\mu_k\frac{\partial k}{\partial y}\\ \mu_\epsilon\frac{\partial \epsilon}{\partial y}\end{bmatrix} \tag{24}$$

$$S=\begin{bmatrix}P-\rho\epsilon Re\\ C_1\frac{\epsilon}{k}P-C_2\rho\frac{\epsilon^2}{k}Re\end{bmatrix} \tag{25}$$

and

$$\mu_k = (\mu+\mu_T/\sigma_k) \tag{26}$$

$$\mu_\epsilon = (\mu+\mu_T/\sigma_\epsilon) \tag{27}$$

$$\tag{28}$$

P represents the production of kinetic energy and can be written in simplified form as [16]

$$P=\mu_T\left({u_x}^2+{u_y}^2\right) \tag{29}$$

The turbulent viscosity is related to the kinetic energy and turbulent dissipation by

$$\mu_T = C_\mu \rho \frac{k^2}{\epsilon} \tag{30}$$

and the constants in the model are usually given by [16, 17, 18]: $\sigma_k = 1.0$, $\sigma_\epsilon = 1.3$, $C_1 = 1.35$, $C_2 = 1.80$ and $C_\mu = 0.09$. The $k - \epsilon$ equations are integrated in time using the same numerical technique as that used for the Navier-Stokes equations.

The equations above represent the high Reynolds number form of the $k-\epsilon$ equations. The equations must be augmented by a near-wall treatment for determining the flow characteristics in the vicinity of solid surfaces. This is usually accomplished using low Reynolds number corrections (*e.g.,* Refs. [15, 19, 20, 21, 22, 23]) or wall functions (*e.g.,* Refs. [16, 17, 24, 25]). For the simulations presented in this study, the low Reynolds number correction of Chien [20] was utilized.

Although the $k - \epsilon$ model includes more relevant physics than the B-L model, it does have certain drawbacks which should be noted. First, there are 5 constants which must be specified (more if low Reynolds number corrections are used). Second, boundary conditions must be specified at the inlet, exit and solid walls. Perhaps the most troublesome boundary conditions are at the inlet, where the free stream turbulence level and a length scale are normally specified. While reasonable estimates can be made for free stream turbulence level, the appropriate length scale is difficult to measure experimentally and requires significant intuition on the part of the user [26, 27].

Transition Models

There has been a considerable amount of interest over the past decade in developing reliable transition models which provide accurate results in zero, favorable and adverse pressure gradients. Several research groups are actively involved in developing transition models for turbomachinery applications based on a combination of analytical, experimental and computational work [28, 29, 30, 31, 32, 33]. Although these newer correlations show great promise, the majority of industrial codes still incorporate simpler transition models.

The current numerical procedure contains four different models for predicting the location of natural transition. The four models represent correlations of data from flat plate experiments, and therefore yield varying results depending on the curvature of the blades. In all the models, the onset of transition is calculated by determining when the local Reynolds number (based on the momentum thickness) exceeds a specified value.

Hall and Gibbings Model

The momentum thickness Reynolds number signifying the start of transition in the model developed by Hall and Gibbings [34] is given by

$$Re_\theta = 190 + exp(6.88 - 1.03\tau) \tag{31}$$

where τ is the free stream turbulence level measured as a percentage of the free stream velocity. This transition model is valid for zero pressure gradients and turbulence levels up to approximately 9 percent.

Seyb and Singh Model

The momentum thickness Reynolds number indicating the beginning of transition based on the model of Seyb [35] and Singh [36] is determined by

$$Re_\theta = \frac{1000}{1.2 + 0.7\tau} + 10\left(\frac{0.09 + \lambda_\theta}{0.0106 + 0.036\tau}\right)^{2.62} \tag{32}$$

where λ_θ is the pressure gradient parameter defined by

$$\lambda_\theta = \frac{\theta^2}{\nu}\frac{dU_\infty}{ds} \tag{33}$$

In Eqn. 33, θ is the boundary layer momentum thickness, ν is the kinematic viscosity, U_∞ is the velocity at the edge of the boundary layer, and s is a distance parameter measured from the leading edge stagnation point.

Dunham Model

The momentum thickness Reynolds number corresponding to the start of transition in the model developed by Dunham [37] is

$$Re_\theta = [0.27 + 0.73exp(-0.8\tau)]\left(550 + \frac{680}{1 + \tau - 21\lambda_\theta}\right) \tag{34}$$

The Dunham model has been widely used, including the study presented in Ref. [38].

Abu-Ghannam and Shaw Model

The momentum thickness Reynolds number indicating the beginning of transition based on the work of Abu-Ghannam and Shaw [39] is given by

$$Re_\theta = 163 + exp\left[F(\lambda_\theta) - \frac{F(\lambda_\theta)}{6.91}\tau\right] \tag{35}$$

where

$$F(\lambda_\theta) = \quad 6.91 + 12.75\lambda_\theta + 63.64(\lambda_\theta)^2 \quad \lambda_\theta < 0 \tag{36}$$

$$F(\lambda_\theta) = \quad 6.91 + 2.48\lambda_\theta - 12.27(\lambda_\theta)^2 \quad \lambda_\theta > 0 \tag{37}$$

The Abu-Ghannam and Shaw model has been successfully used in several turbomachinery studies, including Refs. [40] and [41]. Note, all the transition simulations in this study were performed using the Abu-Ghannam and Shaw model.

For all the transition models, the end of the transition region (*i.e.*, fully turbulent flow) is identified by the position where the local Reynolds number, Re_L, exceeds the following value [39]

$$Re_L = 31.8(Re_\theta)^{1.6} \tag{38}$$

where the momentum thickness Reynolds number is equal to its value at the start of transition. In the region between the beginning and end of transition the intermittency factor, σ, is varied according to the theory of Dwahan and Narasimha [42]

$$\sigma = 0 \qquad x \leq x_{trb} \tag{39}$$

$$\sigma = 1 - exp(-4.64\xi^2) \qquad x_{trb} < x < x_{tre} \tag{40}$$

$$\sigma = 1 \qquad x \geq x_{tre} \tag{41}$$

where x_{trb} denotes the beginning of transition, x_{tre} denotes the end of transition, and

$$\xi = \frac{x - x_{trb}}{x_{tre} - x_{trb}} \tag{42}$$

In cases where separation bubble separation occurs, the correlation developed by Roberts is implemented [43, 44]. All the transition models described in this section were developed from two-dimensional data and are therefore suspect in three-dimensional flow simulations; there are currently no reliable correlations for general three-dimensional turbomachinery flow fields.

NUMERICAL SIMULATIONS

The geometry studied in this investigation is the Pratt & Whitney "PAK B" geometry. The characteristics of this cascade include:

- $T_1 = 530°$R, $P_1 = 14.7$psia
- $M_1 = 0.0897$ (based on a Q-1D analysis), $M_2 = 0.15$
- $\alpha_1 = 35°$, $\alpha_2 = -60°$ (measured from the axial direction)
- $P_2/P_{t1} \approx .9844$ (based on a Q-1D analysis)
- $Re = 27,000 - 200,000$ based on the chord and the inlet flow variables
- Pitch-to-chord ratio = .88558
- Adiabatic walls

Laminar, turbulent, and transitional simulations have been performed to better understand the role of low Reynolds number effects on unsteady separation bubbles.

Baseline PAK B Cascade Simulations

Two computational grids were used in the cascade simulations; the coarser grid contained 251×51 (streamwise×tangential) points in the O-grid and 180×45 points in the H-grid for a total of 20,901 grid points. The average value of y^+, the non-dimensional distance of the first grid point above the surface, was approximately equal to 0.17. The finer computational grid was generated with 281×51 points in the O-grid and 240×45 in the H-grid for a total of 25,131 computational grid points.The average value of y^+ was again about $y^+ = 0.17$. A comparison of the coarse and fine computational grids is presented Table 1. Typical simulations require 0.00029 seconds of CPU time per grid point per iteration on a DEC 3000-300 workstation.

$Re = 40,000$, B-L, Turbulent Flow

Figure 2 illustrates the surface pressure distributions predicted using the coarse and fine grids. The two solutions show fair agreement, with small differences noticeable on the pressure surface and upstream of the throat on the suction surface. Figure 3 contains the surface isentropic Mach number distributions from the coarse and fine-grid simulations. The design Mach number distribution is also included in Fig. 3. The results of the fine-grid simulation show very good agreement with the design data. The coarse grid solution exhibits very good agreement with the design data on the suction surface of the blade, but slightly underpredicts the Mach number on the pressure surface upstream of approximately 65% of the axial chord. The predicted turbulent skin friction distributions are shown in Fig. 4. The fine-grid skin friction distribution is nearly identical to the coarse-grid distribution, including the suction surface separation location. The momentum thickness distributions from the two simulations were also similar. Unless otherwise noted, subsequent figures will contain fine-grid results.

Table 2 contains a comparison of the average inlet and exit quantities from the coarse and fine-grid simulations. Note, the low-speed nature of the flow causes minor changes in the inlet or exit Mach number/stagnation quanitities to have a significant impact on the predicted losses.

$Re = 40,000$, Laminar Flow

Both the coarse and fine-grid laminar flow solutions exhibited a large, unsteady suction-surface separation region. The boundary layer velocity profiles were investigated at different locations to ascertain that an adequate number of grid points were contained in the boundary layer. Figure 5 illustrates velocity profiles at 5% and 65% of the axial chord along the suction surface. Near the leading edge the boundary layer region contains 16 grid points, while near the separation point the boundary layer contains 25 grid points. Figure 6 shows velocity profiles at 5% and 75% of the axial chord along the pressure surface. Similar to the suction surface, the boundary layer near the leading edge contains 16 grid points and the boundary layer near the trailing edge contains approximately 25 grid points. The resolution of the boundary layer appears to be adequate over the entire blade surface. Therefore, the suction surface unsteady flow separation is probably not caused by an insufficient number of grid points.

Figures 7 and 8 illustrate instantaneous Mach number and entropy contours, respectively, from the fine-grid simulation. Figures 7 and 8 are similar to the results of the coarse-grid simulation. Figure 9 and 10 show the pressure and skin friction envelopes, respectively. The amplitude of the unsteadiness along the suction surface (see Fig. 9) and the time-averaged separation location (see Fig. 10) were nearly identical to the coarse-grid results.

Table 2 contains the time-averaged inlet and exit flow quantities from the coarse and fine-grid laminar flow simulations.

$Re = 40,000$, B-L, Transitional Flow

Coarse and fine-grid simulations were performed with the onset of transition prescribed to be at 88% of the axial chord on the suction surface. The transition region extended over 5% of the axial chord. The beginning and end of transition were determined by time-averaging the unsteady transition locations predicted using the Abu-Ghannam/Shaw transition model [39].

Figures 11 and 12 contain instantaneous Mach number and entropy contours, respectively, from the fine-grid simulation. Fixing the transition location eliminates the unsteadiness observed when the position is allowed to vary with time. In addition, the convection of the airfoil wake appears to be more accurately resolved using the refined grid (see Fig. 12). The time-averaged surface isentropic Mach number distributions predicted in the coarse and fine-grid simulations are shown in Fig. 13. The design Mach number distribution is also included in the figure. The coarse and fine-grid solutions are similar and exhibit excellent agreement with the experimental data. Figure 14 illustrates the skin-friction envelopes for the transition flow conditions. Again, the coarse and fine-grid solutions show very good agreement.

$Re = 120,000$, B-L, Transitional Flow

Figure 15 illustrates the predicted and design distributions of the surface (isentropic) Mach number for $Re = 120,000$. The predicted results in Fig. 15 were obtained using the average values of the transition locations predicted by the Abu-Ghannam and Shaw model; the suction surface transition location was set at $x_{tr} = 0.88$ and the pressure surface transition location was specified to be at $x_{tr} = 0.25$. The predicted and design Mach number distributions exhibit close agreement. Figure 16 contains entropy contours for the simulation with fixed transition. The flow field does not display the unsteady shedding from the suction surface displayed at $Re = 40,000$. In addition, the wakes remain undisturbed as they are convected to the exit boundary. The baseline inlet and exit flow quantities, as well as the cascade loss, are presented in Table 3.

$Re = 200,000$, B-L, Transitional Flow

A history of the suction surface transition locations predicted using the Abu-Ghannam and Shaw transition model is shown in Fig. 17. The average transition location is at approximately 80% of the axial chord ($x_{tr} = 0.80$). Thus, the location of transition on the suction surface is 8% upstream of where it was predicted at $Re = 120,000$. The variations in the location of transition shown in Fig. 17 appear to be time-periodic. Since no unsteady shedding was observed in the flow field, the Abu-Ghannam and Shaw transition model may be getting trapped in a limit cycle. The transition location on the pressure surface of the blade was predicted to be at the leading edge (i.e., the flow on the pressure surface is completely turbulent). A comparison of the predicted (using fixed transition) and design surface Mach number distributions are illustrated in Fig. 18. The two sets of data show good agreement, with only small discrepancies visible on the pressure surface near 25% of the axial chord. Similar to the $Re = 120,000$ results, the entropy contours (see Fig. 19) do not indicate unsteady shedding from the suction surface of the blade. The baseline inlet and exit flow quantities, as well as the cascade loss, are presented in Table 3.

Effects of Turbulence Modeling Parameters - $k - \epsilon$

A series of simulations have been performed for the PAK B isolated cascade geometry using the $k - \epsilon$ turbulence model and a free stream turbulence level of $Tu = 3.0\%$. The Reynolds number was set at $Re = 80,000$. The simulations utilized the turbulence field predicted using the Baldwin-Lomax model as the initial solution. Figure 20 contains the skin friction distributions predicted using the B-L turbulence model [47], and the $k - \epsilon$

model with different values of the free stream turbulent viscosity. Setting the free stream turbulent viscosity equal to unity creates too much dissipation and the skin friction behaves in a laminar manner, as evidenced by a large separated flow region on the suction surface of the airfoil. Increasing the free stream turbulent viscosity to a non-dimensional value of 10.0 decreases the dissipation, and the skin friction distribution shows good agreement with the results obtained using the B-L model. The results suggest that the predicted results are strongly dependent on the free stream value of the turbulent viscosity (and consequently ϵ). Figure 21 displays a comparison of the momentum thickness distributions predicted using the two turbulence models. The results obtained using the $k-\epsilon$ model with $\mu_{t_\infty} = 10.0$ show fair agreement with the results obtained using the B-L model. The $k-\epsilon$ model produces a greater momentum thickness on the pressure surface, while the B-L model produces a greater momentum thickness on the suction surface. Figures 22-24 show the Mach number, entropy and turbulent viscosity contours, respectively, predicted using the $k-\epsilon$ model with $\mu_{T_\infty} = 10.0$. The contours are much smoother then those predicted using the B-L model, especially those for the turbulent viscosity. Figure 25 illustrates the predicted and design distributions of the surface (isentropic) Mach number. The predicted results and the design data exhibit good agreement.

The simulations with using $\mu_{T_\infty} = 10.0$ were repeated with the free stream turbulence level increased to $Tu = 6.0\%$. Figures 26 and 27 illustrate comparisons of the skin friction and momentum thickness distributions, respectively, with free stream turbulence levels of 3.0% and 6.0%. The skin friction distributions from the two simulations are similar (see Fig. 26), except that $Tu = 6.0\%$ produces slightly smaller values over the first 50% of the axial chord on the suction surface. The momentum thickness distributions are comparable on the suction surface of the airfoil (see Fig. 27). In the cove region on the pressure surface, however, the lower free stream turbulence level generates a much larger momentum thickness. Figures 28-30 show the Mach number, entropy and turbulent viscosity contours, respectively. The three figures are similar to those obtained for $Tu = 3.0\%$ (see Figs. 22-24), which suggests that the solution is more dependent on the initial free stream value of ϵ than on the free stream turbulence level.

PAK B Cascade Wake-Passing Simulations

$Re = 40,000$, LSRR Stator Wake, B-L, Transitional Flow

To accurately model the flow physics of a turbine stage, a wake definition was obtained from a numerical simulation for the first-stage stator of the Large Scale Rotating Rig (LSRR) turbine [48]. In the unsteady numerical simulations utilizing the LSRR stator wake, the perturbations in the velocity components, pressure and density have been included in the definition of the unsteady inlet boundary conditions.

The LSRR stator geometry was rotated 32 degrees for use in the current investigation (see Fig. 31), such that the flow would be turned approximately 135 degrees by the combination of the stator and the PAK B turbine blade. The wake velocity profile generated by the numerical simulation for the stator is shown in Fig. 32. The wake width is approximately 25% of the stator gap, and the wake deficit is approximately 10% of the free stream velocity. The unsteady simulations were performed assuming one upstream stator wake for every two rotor blade passages (*i.e.,* interblade phase angle of $\sigma = \pi$), and the reduced temporal frequency was set to $k = 5$. One unsteady simulation was performed with a fixed value for the transition location on each surface of the blade, and one simulation was performed using the Abu-Ghannam and Shaw model to predict the location of natural transition [39] and

Roberts correlation to predict bubble transition [43, 44].

Figure 33 illustrates perturbation (*i.e.,* instantaneous minus time-averaged) vorticity contours for the simulation with a fixed location for transition. The vorticity associated with the stator wake is generally smaller than the values in the viscous layer near the blade, but it can still be used to highlight the path of the wake upstream of the blade row. Because the pressure and density are allowed to vary through the wake, the entropy can be used to track the movement of the wakes through the entire blade passage. Figures 34 and 35 illustrate instantaneous entropy contours from the simulations with fixed and predicted (floating) transition, respectively. The stretching of the wake between the pressure and suction surfaces of adjacent blades is evident in the blade passages. The interaction between the stator and blade wakes downstream of the blade passages is also discernible. Comparing Figs. 34 and 35, it is observed that the simulation with floating transition exhibits more unsteadiness in, and downstream of, the blade passage.

The predicted skin friction envelopes from the two unsteady simulations are shown in Figs. 36 and 37, respectively. The results using floating transition (see Fig. 37) exhibit more unsteadiness along the suction surface of the blade than the results with fixed transition. Moreover, the results for fixed transition indicate that the flow downstream of the time-averaged separation point intermittently reattaches, while the results for floating transition do not show reattachment during any portion of the wake-passing cycle. Along the majority of the pressure surface the two solutions show good agreement. Differences are noticeable near 25% of the chord, where the case with floating transition appears to be closer to separation, and near the trailing edge where the case with floating transition displays more unsteadiness.

Figures 38 and 39 contain the momentum thickness envelopes from the simulations with fixed and floating transition, respectively. The predicted results for the pressure surface are similar in both simulations, except that the simulation with floating transition shows smaller values near 25% of the chord (corresponding the differences in the skin friction distributions noted above). Along the suction surface of the blade the simulation with floating transition shows more unsteadiness, especially near the trailing edge.

The variation in the flow angle exiting the blade row is illustrated in Fig. 40. The case with fixed transition produced a periodic variation of approximately 0.35 degrees in the exit flow angle. The simulation with floating transition generated an exit flow angle variation of almost 1 degree, and was only marginally periodic.

In the simulation with floating transition, the temporal variation of the transition locations were recorded (see Figs. 41 and 42). In both figures, a value of 0 corresponds to the leading edge and a value of 1.0 corresponds to the trailing edge. Along the suction surface of the blade (see Fig. 41), the transition point is located at, or near, the trailing edge for the majority of the wake passing cycle. During portions of the cycle, the transition location moves forward to approximately 75% of the axial chord. When transition was predicted upstream of the trailing edge, it was due to bubble transition. Along the pressure surface of the blade (see Fig. 42), the location of transition varied between 25% of the chord and the trailing edge. Similar to the suction surface results, bubble transition was observed at all times along the pressure surface of the blade. When transition was predicted near 25% of the chord, it was due to cove separation. An interesting phenomenon was observed when transition was predicted upstream of the trailing edge. For several time steps bubble transition would be predicted at a given location. During this time, the eddy viscosity added to the flow reduced or eliminated the separation bubble. After the separation bubble disappeared the transition model did not detect transition until the trailing edge, allowing the separation bubble to develop once more. This cycle was repeated several times (see Fig. 43). A similar

process was also observed on the suction surface of the blade.

Table 4 contains the average inlet and exit flow quantities from the baseline simulation, and the two simulations utilizing the LSRR stator wake. The time-averaged Mach numbers and flow angles show very good agreement with the baseline results. The time-averaged losses from both unsteady simulations are greater than the baseline loss. In addition, the losses predicted using floating transition are greater than those predicted using fixed transition.

$Re = 120,000$, LSRR Stator Wake, B-L, Transitional Flow

Figures 44 and 45 illustrate instantaneous entropy contours from the simulations with fixed and predicted (floating) transition, respectively. The stretching of the wakes between the pressure and suction surfaces of adjacent blades is evident in the blade passages. Downstream of the blade passage there are two distinct wakes, the one specified at the computational inlet and the one generated by the PAK B blade row. Comparing Figs. 44 and 45 it is observed that the two solutions are similar, except that the simulation with fixed transition exhibits somewhat more unsteadiness near the blade trailing edge. Note, in the simulation using the Abu-Ghannam and Shaw model the location of the suction surface transition point moved from 88% of the chord to the trailing edge, while the pressure surface transition location moved from 25% of the chord to the leading edge.

The predicted unsteady skin friction envelope for the simulation with a fixed transition location is shown in Fig. 46. The skin friction exhibits a moderate amount of unsteadiness along the suction surface of the blade up to approximately 88% of the chord, where transition occurs. Downstream of transition a larger amount of unsteadiness is observed. In a time-averaged sense the flow along the suction surface of the blade remains attached, but intermittent flow separation is detected from approximately 73% of the axial chord (just downstream of the throat) to the trailing edge. Along the pressure surface of the blade, the flow contains cove separation from approximately 10% to 35% of the chord. The skin friction displays little unsteadiness along the pressure surface, except in the separated flow region.

Figure 47 contains the skin friction envelope for the simulation in which transition was predicted. The skin friction shows a considerable amount of unsteadiness over the entire suction surface of the blade. Unlike the simulation with fixed transition, there is no intermittent flow separation on the suction surface. The time-averaged flow on the pressure surface of the blade remains attached, but intermittent separation is again observed in the cove region. The differences observed in the skin friction distributions illustrated in Figs. 46 and 47 are probably due to the movement of the suction and pressure surface transition points in the simulation in which transition was predicted.

Figure 48 contains the unsteady momentum thickness envelope from the simulation with a fixed transition location. There is very little unsteadiness on the suction surface upstream of the intermittent separation point. Much larger values of the momentum thickness are present from the approximately 75% of the axial chord to the trailing edge. The momentum thickness shows significant excursions around the time-averaged values along the pressure surface of the blade. The largest values on the pressure surface correspond to the region of cove separation discussed above.

The unsteady momentum thickness envelope for the simulation with floating transition is shown in Fig. 49. The unsteadiness about the time-averaged values gradually increases with distance from the leading edge along the suction surface of the airfoil. The minimum, maximum, and time-averaged values are all greater than the corresponding values for a fixed transition location because the flow has become laminar over the entire suction surface.

Large levels of unsteadiness are observed on the pressure surface, especially in the cove region. Overall, however, the pressure surface values are smaller than the corresponding values for fixed transition.

The temporal variation in the exit flow angle is illustrated in Fig. 50. Both flow angle distributions exhibit some high-frequency unsteadiness (perhaps due to trailing-edge vortex shedding and/or the movement of the transition location), in addition to unsteadiness at the wake-passing frequency. The average exit flow angle from the simulation with floating transition is approximately 0.5 degrees greater than that for fixed transition.

Table 5 contains the average inlet and exit flow quantities from the baseline simulation (fixed transition), and the two simulations utilizing the LSRR stator wake. The time-averaged Mach numbers and flow angles from the unsteady simulation with fixed transition show very good agreement with the baseline results. The time-averaged loss from the unsteady simulation with fixed transition, however, is over 20% less than in the baseline simulation. The unsteady simulation with floating transition displays less turning and higher losses than either of the other two simulations.

$Re = 200,000$, LSRR Stator Wake, B-L, Transitional Flow

Figures 51 and 52 illustrate instantaneous entropy contours from the simulations with fixed and predicted (floating) transition, respectively. The two solutions compare favorably throughout the blade row. Note, in the simulation using the Abu-Ghannam and Shaw model the location of the suction surface transition point moved from 80% of the chord to the trailing edge, while the pressure surface transition location remained at the leading edge.

The predicted unsteady skin friction envelope for the simulation with a fixed transition location is shown in Fig. 53. Also included in Fig. 53 is the baseline skin friction distribution. The skin friction remains relatively constant along the suction surface of the blade up to approximately 65% of the chord, where it rapidly increases. This location corresponds to the throat of the blade passage. From approximately 70% of the chord to the trailing edge the skin friction gradually decreases. The baseline and time-averaged distributions are nearly identical over the entire suction surface of the blade, although the nature of the distributions differs from that seen at lower Reynolds numbers. No flow separation occurs along the suction surface of the blade. Along the pressure surface of the blade the skin friction approaches zero, but the flow does not separate. The skin friction displays little unsteadiness along the pressure surface of the airfoil.

Figure 54 contains the skin friction envelope for the simulation in which transition was predicted, along with the corresponding baseline results. The skin friction shows a considerable amount of unsteadiness over the entire suction surface of the blade. In addition, the baseline and time-averaged solutions are significantly different, which may be caused by the movement of transition to the trailing edge in the unsteady simulation. The baseline distributions displayed in Figs. 53 and 54 show good agreement up to the throat, but are different downstream of the throat. Allowing transition to float in the baseline simulation caused the generation of a separation bubble just downstream of the throat. No separation is detected on either surface of the airfoil in the unsteady simulation.

Figures 55 and 56 contain the unsteady momentum thickness envelopes for the simulations with fixed and floating transition, respectively. In Fig. 55 the suction surface values remain relatively constant, with little unsteadiness, up to the throat of the passage. Downstream of the throat the momentum thickness increases, as do the excursions around the time-averaged values. There is significant unsteadiness in the momentum thickness on the

pressure surface, especially in the cove region of the airfoil. In general, the momentum thickness values shown in Fig. 55 are smaller than those for $Re = 120,000$ (see Fig. 48). In Fig. 56, the suction surface distribution exhibits more unsteadiness than with fixed transition (see Fig. 55). The time-averaged values of the momentum thickness on the suction surface are greater than those shown in Fig. 55, which is expected because the transition point has been shifted to the trailing edge. The pressure surface momentum thickness distribution agrees closely with that for fixed transition because in both cases the flow is fully turbulent.

A time history of the exit flow angle is illustrated in Fig. 57. The two distributions show very good agreement, although there is somewhat more high-frequency unsteadiness in the simulation with fixed transition.

Table 6 contains the average inlet and exit flow quantities from the baseline simulation (fixed transition), and the two simulations utilizing the LSRR stator wake. The time-averaged Mach numbers and flow angles from both unsteady simulations show very good agreement with the baseline results. The time-averaged loss from the unsteady simulation with fixed transition is approximately 8% less than in the baseline simulation, while the loss in the unsteady simulation with floating transition is approximately 13% less than in the baseline simulation.

PAK B Turbine Stage Simulations - $Re = 27,000$-$Re = 200,000$

A turbine stage was produced using the PAK B geometry for both the vane and rotor airfoils. A 1-vane/2-rotor blade count ratio was assumed, and the axial gap between the vane and blade was specified to be 30% of the rotor chord. Figure 58 shows the computational grid topology, which contains 75,393 grid points. The rotational speed of the rotor was specified such that the time-averaged relative frame flow angle entering the rotor passage was approximately equal to that used in the isolated blade row simulations ($\beta_2 = 35^o$).

A matrix of numerical simulations have been performed for the PAK B turbine stage configuration described above. Turbulent, floating transition and fixed transition simulations have been performed for Reynolds numbers of $Re = 27,000$, $Re = 40,000$, $Re = 60,000$, $Re = 80,000$, $Re = 120,000$ and $Re = 200,000$ based on the inlet flow conditions. These Reynolds numbers correspond to a range of $Re = 40,000$ and $Re = 300,000$ based on the exit flow conditions. The simulations were performed using both the B-L and $k - \epsilon$ turbulence models. To facilitate interpretation of the results, Tables 7-12 contain the time-averaged flow quantities at the inlet and exit of each blade row for the turbulent and transitional simulations at each Reynolds number. All solutions were time-averaged over two blade-passing cycles, although the extent of flow separation and the tabulated results suggest that the solution may need to be averaged over additional blade-passing cycles. Note, the efficiencies show considerable scatter; this is due in part to the low Mach number flow (small changes in P_t or T_t equates to large changes in the efficiency) and the need for more blade-passing cycles in the time-averaging process.

Figures 59-61 illustrates the vane and rotor flow turning angles for fully turbulent, floating transition and fixed transition flow assumptions (using the Baldwin-Lomax turbulence model) as a function of the Reynolds number. Figure 62 contains the variation of the vane and rotor suction-side transition locations as a function of the Reynolds number. The turning angles and transition locations are directly related to the size of the suction-surface separation bubbles. The transition from laminar to turbulent flow always occurred as bubble transition, not natural transition. In addition, for all the cases tested the time-averaged suction-surface transition location was close to the trailing edge (indicating laminar flow

over the majority of the suction surface). The skin friction envelopes corresponding to the turbulent and transitional solutions at the five Reynolds numbers are shown in Figs. 63-84, respectively. The momentum thickness distributions for the different test conditions are shown in Figs. 85-106, respectively.

Samples of instantaneous entropy and Mach number contours from turbulent flow simulations at $Re = 40,000$ and $Re = 120,000$ are shown in Figs. 107-110.

CONCLUSIONS

A numerical study of the losses associated with low Reynolds number flow has been conducted for a turbine cascade and turbine stage. Laminar, transitional and turbulent flow simulations were performed (over a range of Reynolds numbers) using algebraic and two-equation turbulence models, as well as algebraic transition models. The predicted results indicate increased losses as the Reynolds number is decreased, and highlight the need for improved turbulence and transition modeling. In addition, at the lower Reynolds numbers (less than approximately $Re = 60,000$)

- the flow field is inherently unsteady
- the algebraic turbulence model begins to break down and requires significant user intervention
- the algebraic transition models can get trapped in limit cycles

References

[1] Baldwin, B. S. and Lomax, H., "Thin-Layer Approximation and Algebraic Model for Separated Turbulent Flows," AIAA Paper 78-257, January, 1978.

[2] Dorney, D. J., and Verdon, J. M., "Numerical Simulations of Unsteady Cascade Flows," *ASME Journal of Turbomachinery*, Vol. 116, No. 4, October 1994, pp. 665-675.

[3] Dorney, D. J., and Davis, R. L., "Numerical Simulations of Unsteady Transonic Flows in Turbomachines," AIAA Paper 94-2833, 1994.

[4] Rai, M. M., "Three-Dimensional Navier-Stokes Simulations of Turbine Rotor-Stator Interaction," *AIAA Journal of Propulsion and Power* Vol. 5, 1989, pp. 307-319.

[5] Chakravarthy, S. R., and Osher, S., "Numerical Experiments with the Osher Upwind Scheme for the Euler Equations," AIAA Paper 82-0975, 1982.

[6] Roe, P. L., "Approximate Riemann Solvers, Parameter Vectors, and Difference Schemes," *Journal of Computational Physics*, Vol. 43, 1981, pp. 357-372.

[7] Giles, M. B., "Nonreflecting Boundary Conditions for Euler Equation Calculations," *AIAA Journal*, Vol. 28, No. 12, December, pp. 2050-2058, 1990.

[8] Steinke, R. J., "Application of a Two-Dimensional Unsteady Viscous Analysis Code to a Supersonic Throughflow Fan Stage," NASA TM 4141, 1989.

[9] Rai, M. M., "An Implicit, Conservative, Zonal-Boundary Scheme for Euler Equation Calculations," AIAA Paper 85-0488, 1985.

[10] Granville, P. S., "A Modified Van Driest Formula for the Mixing Length of Turbulent Boundary Layers in Pressure Gradients," *ASME Journal of Fluids Engineering*, Vol. 111, March, 1989, pp. 94-97.

[11] York, B. and Knight, D., "Calculation of Two-Dimensional Turbulent Boundary Layers Using the Baldwin-Lomax Model," *AIAA Journal*, Vol. 23, No. 12, 1985, pp. 1849-1850.

[12] Sakowski, B., Darling, D., Roach, R., and van de Wall, A., "Evaluation and Application of the Baldwin-Lomax Turbulence Model in Two-Dimensional, Unsteady, Compressible Boundary Layers With and Without Separation in Engine Inlets," AIAA Paper 92-3676, 1992.

[13] Dorney, D. J., "Reynolds-Averaged Navier-Stokes Studies of Low Reynolds Number Effects on the Losses in a Low Pressure Turbine," Progress Report 9, NAG3-1668, March 25, 1996.

[14] Jones, W. P. and Launder, B. E., "The Prediction of Laminarization With a Two-Equation Model of Turbulence," *International Journal of Heat and Mass Transfer*, Vol. 15, 1972, pp. 301-314.

[15] Jones, W. P. and Launder, B. E., "The Calculation of Low-Reynolds-Number Phenomena With a Two-Equation Model of Turbulence," *International Journal of Heat and Mass Transfer*, Vol. 16, 1973, pp. 1119-1130.

[16] Gorski, J. J., Ota, D. K., and Chakravarthy, S. R., "Calculation of Three Dimensional Cavity Flow Fields," AIAA Paper 87-0117, 1987.

[17] Sondak, D. L., Pletcher, R. H., and Van Dalsem, W. R., "Wall Functions for the $k-\epsilon$ Turbulence Model in General Nonorthogonal Curvilinear Coordinates," Iowa State University Report HTL-55, CFD-25, May, 1992.

[18] Towne, C. E., Schwab, J. R., Bui, T. T., "Proteus Two-Dimensional Navier-Stokes Computer Code - Version 2.0; Volume 1 - Analysis Description," NASA TM 106336, October, 1993.

[19] Lam, C. K. G. and Bremhorst, K., "A Modified Form of the $k-\epsilon$ Model for Predicting Wall Turbulence," *ASME Journal of Fluids Engineering*, Vol. 103, September, 1981, pp. 456-460.

[20] Chien, K.-Y., "Predictions of Channel and Boundary-Layer Flows with a Low-Reynolds-Number Turbulence Model," *AIAA Journal*, Vol. 20, January, 1982, pp. 33-38.

[21] Patel, V. C., Rodi, W., and Scheuer, G., "Turbulence Models for Near-Wall and Low-Reynolds Number Flows: A Review," *AIAA Journal*, Vol. 23, 1985, pp. 1309-1319.

[22] Nagano, Y. and Hishida, M., "Improved Form of the $k-\epsilon$ Model for Wall Turbulent Shear Flows," *ASME Journal of Fluids Engineering,* Vol. 109, June, 1987, pp. 156-160.

[23] Kral, L. D., Mani, M., and Ladd, J. A., "On the Application of Turbulence Models for Aerodynamic and Propulsion Flow Fields," AIAA Paper 96-0564, 1996.

[24] Gorski, J. J., "A Near Wall Formulation for the $k-\epsilon$ Equations of Turbulence," AIAA Paper 86-0556, 1986.

[25] Speziale, C. G., Abid, R., and Anderson, E. C., "A Critical Evaluation of Two-Equation Models for Near Wall Turbulence," AIAA Paper 90-1481, 1990.

[26] Chima, R. V., "A $k-\omega$ Turbulence Model for Quasi-Three-Dimensional Turbomachinery Flows," AIAA Paper 96-0248, 1996.

[27] Kunz, R. F. and Lakshminarayana, B., "Three-Dimensional Navier-Stokes Computation of Turbomachinery Flows Using an Explicit Numerical Procedure and a Coupled $k-\epsilon$ Turbulence Model," *ASME Journal of Turbomachinery,* Vol. 114, 1991, pp. 627-636.

[28] Walker, G. J. and Gostelow, J. P., "Effects of Adverse Pressure Gradients on the Nature and Length of Boundary Layer Transition," *ASME Journal of Turbomachinery,* Vol. 112., April, 1990, pp. 196-205.

[29] Hodson, H. P., "Modeling Unsteady Transition and Its Effects on Profile Loss," *ASME Journal of Turbomachinery,* Vol. 112, October, 1990, pp. 691-701.

[30] Addison, J. S. and Hodson, H. P., "Unsteady Transition in an Axial Flow Turbine: Part 1 - Measurements on the Turbine Rotor," *ASME Journal of Turbomachinery*, Vol. 112, 1990, pp. 206-214.

[31] Addison, J. S. and Hodson, H. P., "Unsteady Transition in an Axial Flow Turbine: Part 2 - Cascade Measurements and Modeling," *ASME Journal of Turbomachinery*, Vol. 112, 1990, pp. 215-221.

[32] Gostelow, J. P. and Blunden, A. R., "Investigations of Boundary Layer Transition in an Adverse Pressure Gradient," ASME Paper 88-GT-298, 1988.

[33] Walker, G. J., "Transitional Flow on Axial Turbomachine Blading," AIAA Paper 87-0010, 1987.

[34] Hall, D. J., and Gibbings, J. C., "Influence of Stream Turbulence and Pressure Gradient Upon Boundary Layer Transition," *IMechE Journal of Engineering Science*, Vol. 14, No. 2, 1972, pp. 134-146.

[35] Seyb, N. J., "A Simplified and Practical Method of Determining the External Heat-Transfer Coefficient Round a Turbine Blade," ARC Report 29298, 1967.

[36] Singh, U. K., *The Effect of Viscosity on the Flow Past Aerofoils in a Cascade,* Ph.D. thesis, Liverpool University, Liverpool, England, 1974.

[37] Dunham, J., "Predictions of Boundary Layer Transition on Turbomachinery Blades," AGARD-AG-164, 1972, pp. 57-71.

[38] Barnett, M., Hobbs, D. E., and Edwards, D. E., "Inviscid Viscous Interaction Analysis of Compressor Cascade Performance," ASME Paper 90-GT-15, 1990.

[39] Abu-Ghannam, B. J., and Shaw, R., "Natural Transition of Boundary Layers - The Effects of Turbulence, Pressure Gradient, and Flow History," *IMechE Journal of Mechanical Engineering Science*, Vol. 22, No. 5, 1980, pp. 213-228.

[40] Cho, N.-H., Liu, X., Rodi, W., and Schonung, B., "Calculation of Wake-Induced Unsteady Flow in a Turbine Cascade," ASME Paper 92-GT-306, 1992.

[41] Dorney, D. J., "A Comparative Study of Four Algebraic Transition Models," *SAE Journal of Aerospace Engineering*, Vol. 103, Section 1, 1994, pp. 112-119.

[42] Dwahan, S., and Narasimha, R., "Some Properties of Boundary Flow During Transition from Laminar to Turbulent Motion," *Journal of Fluid Mechanics*, Vol. 3, 1958, pp. 418-436.

[43] Roberts, W. B., *A Study of the Effect of Reynolds Number and Laminar Separation Bubbles on the Flow Through an Axial Compressor Cascade*, Ph.D. thesis, The von Karman Institute, Brussels, Belgium, 1973.

[44] Roberts, W. B., "Calculation of Laminar Separation Bubbles and Their Effect on Airfoil Performance," AIAA Paper 79-0285, 1979.

[45] Dorney, D. J., "Reynolds-Averaged Navier-Stokes Studies of Low Reynolds Number Effects on the Losses in a Low Pressure Turbine," Progress Report 7, NAG3-1668, September 18, 1995.

[46] White, F. M., *Viscous Fluid Flow*, McGraw Hill and Co., New York, 1974.

[47] Dorney, D. J., "Reynolds-Averaged Navier-Stokes Studies of Low Reynolds Number Effects on the Losses in a Low Pressure Turbine," Progress Report 8, NAG3-1668, December 10, 1995.

[48] Dring, R. P., Joslyn, H. D., Hardin, L. W., and Wagner, J. H., "Turbine Rotor-Stator Interaction," *ASME Journal of Engineering for Power*, Vol. 104, October, 1982, pp. 729-742.

	Coarse Grid	Fine Grid
O-grid	251×51	281×51
H-grid	180×45	240×45
Total grid points	20,901	25,131
y^+_{avg}	0.1732	0.1734

Table 1: Coarse and fine grid topologies

	Design	Turbulent (coarse)	Turbulent (fine)	Laminar (coarse)	Laminar (fine)	Transitional (coarse)	Transitional (fine)
M_1	0.0897	0.0935	0.0927	0.0905	0.0907	0.0930	0.0934
M_2	0.1500	0.1459	0.1440	0.1450	0.1474	0.1470	0.1468
α_1	35.00°	35.00°	35.00°	35.01°	35.00°	34.99°	35.00°
α_2	-60.00°	-58.20°	-58.00°	-58.27°	-58.65°	-58.32°	-58.27°
$\Delta P_t/P_{t1}$	–	0.00085	0.00122	0.00098	0.00063	0.00076	0.00082

Table 2: Average inlet and exit flow quantities for PAK B blade at $Re = 40,000$

	$Re = 120,000$	$Re = 200,000$
M_1	0.0941	0.0946
M_2	0.1482	0.1480
α_1	35.01°	35.00°
α_2	-58.36°	-58.19°
$\Delta P_t/q_2$	0.03087	0.02632

Table 3: Inlet and exit flow quantities for the PAK B blade at $Re = 120,000; 200,000$

	Baseline (without wake)	Time-Averaged Fixed Transition	Time-Averaged Floating Transition
M_1	0.0935	0.0935	0.0935
M_2	0.1468	0.1476	0.1465
α_1	35.00°	35.02°	34.99°
α_2	-58.27°	-58.49°	-58.19°
$\Delta P_t/q_2$	0.04699	0.04806	0.04978

Table 4: Inlet and exit flow quantities for the PAK B blade at $Re = 40,000$, transitional, LSRR stator wake

	Baseline (without wake)	Time-Averaged Fixed Transition	Time-Averaged Floating Transition
M_1	0.0941	0.0942	0.0943
M_2	0.1482	0.1486	0.1466
α_1	35.01^o	35.01^o	34.96^o
α_2	-58.36^o	-58.45^o	-57.94^o
$\Delta P_t/q_2$	0.03087	0.02359	0.04299

Table 5: Inlet and exit flow quantities for the PAK B turbine blade at $Re = 120,000$

	Baseline (without wake)	Time-Averaged Fixed Transition	Time-Averaged Floating Transition
M_1	0.0946	0.0947	0.0947
M_2	0.1480	0.1482	0.1482
α_1	35.00^o	34.99^o	34.97^o
α_2	-58.19^o	-58.15^o	-58.19^o
$\Delta P_t/q_2$	0.02632	0.02431	0.02298

Table 6: Inlet and exit flow quantities for the PAK B turbine blade at $Re = 200,000$

	Time-Averaged Fixed Transition	Time-Averaged Floating Transition	Time-Averaged Turbulent	Time-Averaged $k-\epsilon$
M_1	0.0921	0.0890	0.0904	0.0785
M_2	0.1472	0.1449	0.1421	0.1219
M_3	0.0958	0.0928	0.0920	0.0783
$\tilde{M}_2$	0.0972	0.0945	0.0923	0.0796
$\tilde{M}_3$	0.1466	0.1436	0.1425	0.1215
α_1	-35.00^o	-35.00^o	-35.00^o	-35.00^o
α_2	57.32^o	58.02^o	57.44^o	55.79^o
α_3	-35.16^o	-35.11^o	-34.31^o	-27.12^o
β_2	34.16^o	34.40^o	33.08^o	22.91^o
β_3	-57.88^o	-58.22^o	-57.84^o	-58.13^o
$\Delta\alpha_{12}$	92.32^o	93.02^o	92.44^o	90.79^o
$\Delta\beta_{23}$	92.04^o	92.62^o	90.92^o	81.04^o
η_{tt}	0.942	0.894	0.873	0.781

Table 7: Inlet and exit flow quantities for the PAK B turbine stage at $Re = 27,000$

	Time-Averaged Fixed Transition	Time-Averaged Floating Transition	Time-Averaged Turbulent	Time-Averaged $k-\epsilon$
M_1	0.0844	0.0848	0.0897	0.0863
M_2	0.1338	0.1357	0.1409	0.1322
M_3	0.0840	0.0858	0.0914	0.0836
$\tilde{M}_2$	0.0839	0.0859	0.0909	0.0831
$\tilde{M}_3$	0.1344	0.1366	0.1422	0.1338
α_1	-35.00^o	-35.00^o	-35.00^o	-35.01^o
α_2	58.27^o	58.17^o	57.71^o	57.70^o
α_3	-32.84^o	-33.95^o	-34.67^o	-32.53^o
β_2	32.20^o	32.33^o	33.29^o	30.64^o
β_3	-58.43^o	-58.74^o	-58.15^o	-58.35^o
$\Delta\alpha_{12}$	93.27^o	93.17^o	92.71^o	92.74^o
$\Delta\beta_{23}$	90.63^o	91.07^o	91.44^o	88.99^o
η_{tt}	0.826	0.847	0.925	0.791

Table 8: Inlet and exit flow quantities for the PAK B turbine stage at $Re = 40,000$

	Time-Averaged Fixed Transition	Time-Averaged Floating Transition	Time-Averaged Turbulent	Time-Averaged $k-\epsilon$
M_1	0.0930	0.0919	0.0918	0.0926
M_2	0.1493	0.1480	0.1452	0.1465
M_3	0.0972	0.0954	0.0942	0.0928
$\tilde{M}_2$	0.0990	0.0976	0.0952	0.0960
$\tilde{M}_3$	0.1482	0.1470	0.1449	0.1426
α_1	-35.00^o	-35.00^o	-35.00^o	-35.00^o
α_2	57.40^o	57.62^o	57.40^o	57.60^o
α_3	-35.59^o	-35.20^o	-34.73^o	-33.20^o
β_2	34.88^o	34.81^o	33.89^o	34.69^o
β_3	-57.90^o	-57.94^o	-57.77^o	-57.08^o
$\Delta\alpha_{12}$	92.40^o	92.62^o	92.40^o	92.60^o
$\Delta\beta_{23}$	92.78^o	92.75^o	91.66^o	91.77^o
η_{tt}	0.952	0.949	0.911	0.907

Table 9: Inlet and exit flow quantities for the PAK B turbine stage at $Re = 60,000$

	Time-Averaged Fixed Transition	Time-Averaged Floating Transition	Time-Averaged Turbulent	Time-Averaged $k-\epsilon$
$\bar{M}_1$	0.0947	0.0922	0.0905	0.0910
$\bar{M}_2$	0.1507	0.1476	0.1424	0.1441
$\bar{M}_3$	0.1000	0.0958	0.0919	0.0920
$\tilde{M}_2$	0.1021	0.0971	0.0922	0.0936
$\tilde{M}_3$	0.1514	0.1470	0.1427	0.1424
α_1	$-35.00°$	$-35.00°$	$-35.00°$	$-35.00°$
α_2	$57.00°$	$57.70°$	$57.71°$	$57.91°$
α_3	$-35.81°$	$-35.87°$	$-34.58°$	$-34.04°$
β_2	$35.04°$	$34.98°$	$33.79°$	$34.54°$
β_3	$-57.51°$	$-58.24°$	$-58.01°$	$-57.68°$
$\Delta\alpha_{12}$	$92.00°$	$92.70°$	$92.71°$	$92.91°$
$\Delta\beta_{23}$	$92.55°$	$93.22°$	$91.80°$	$92.22°$
η_{tt}	0.961	0.947	0.882	0.887

Table 10: Inlet and exit flow quantities for the PAK B turbine stage at $Re = 80,000$

	Time-Averaged Fixed Transition	Time-Averaged Floating Transition	Time-Averaged Turbulent	Time-Averaged $k-\epsilon$
$\bar{M}_1$	0.0890	0.0902	0.0903	0.0949
$\bar{M}_2$	0.1410	0.1431	0.1419	0.1522
$\bar{M}_3$	0.0907	0.0923	0.0919	0.0997
$\tilde{M}_2$	0.0903	0.0923	0.0916	0.1025
$\tilde{M}_3$	0.1419	0.1437	0.1429	0.1507
α_1	$-35.00°$	$-35.00°$	$-35.00°$	$-35.00°$
α_2	$58.25°$	$58.24°$	$57.82°$	$56.71°$
α_3	$-35.11°$	$-35.53°$	$-34.88°$	$-35.89°$
β_2	$34.40°$	$34.90°$	$33.88°$	$34.67°$
β_3	$-58.51°$	$-58.49°$	$-58.17°$	$-57.63°$
$\Delta\alpha_{12}$	$93.25°$	$93.24°$	$92.82°$	$91.71°$
$\Delta\beta_{23}$	$92.91°$	$93.39°$	$92.05°$	$92.30°$
η_{tt}	0.929	0.947	0.934	0.987

Table 11: Inlet and exit flow quantities for the PAK B turbine stage at $Re = 120,000$

	Time-Averaged Fixed Transition	Time-Averaged Floating Transition	Time-Averaged Turbulent	Time-Averaged $k-\epsilon$
M_1	—	—	0.0949	0.0985
M_2	—	—	0.1509	0.1567
M_3	—	—	0.0993	0.1061
$\tilde{M}_2$	—	—	0.1011	0.1096
$\tilde{M}_3$	—	—	0.1498	0.1568
α_1	—	—	-35.00^o	-35.00^o
α_2	—	—	56.88^o	57.67^o
α_3	—	—	-35.29^o	-36.33^o
β_2	—	—	34.48^o	34.65^o
β_3	—	—	-57.38^o	-57.21^o
$\Delta\alpha_{12}$	—	—	91.88^o	92.67^o
$\Delta\beta_{23}$	—	—	91.86^o	91.86^o
η_{tt}	—	—	0.989	0.981

Table 12: Inlet and exit flow quantities for the PAK B turbine stage at $Re = 200,000$

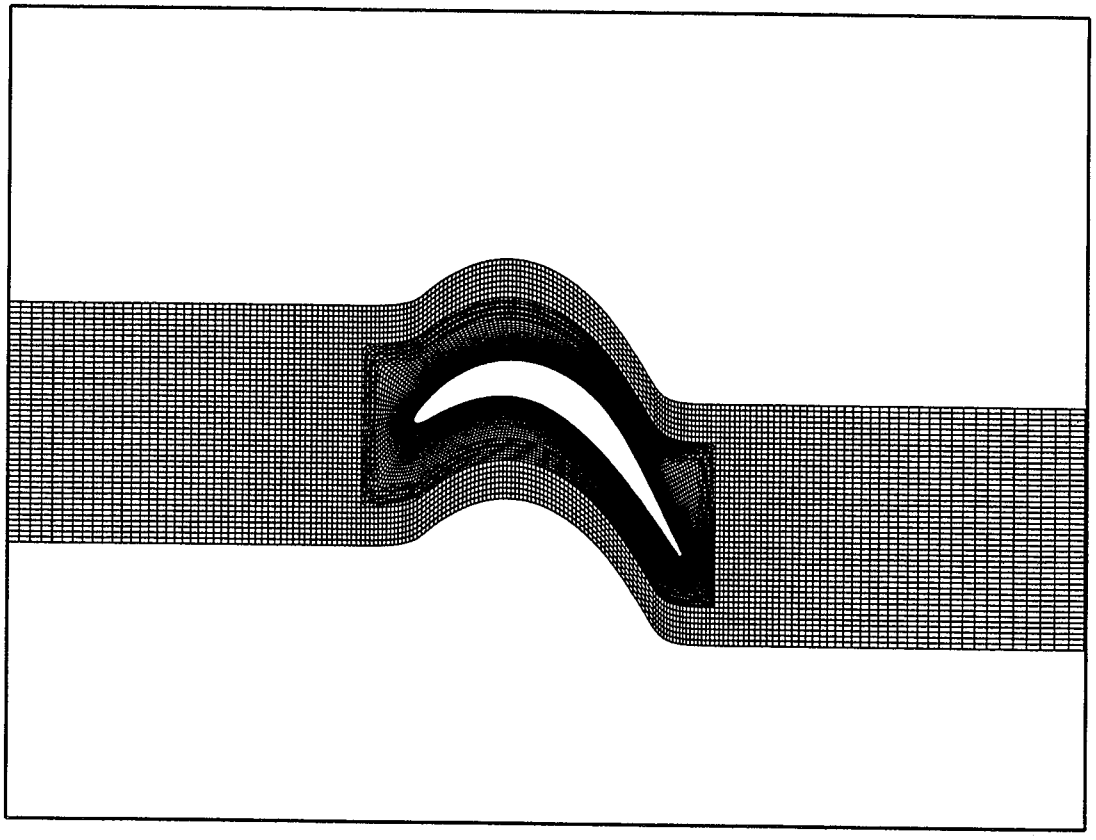

Figure 1: Computational grid for the PAK B cascade

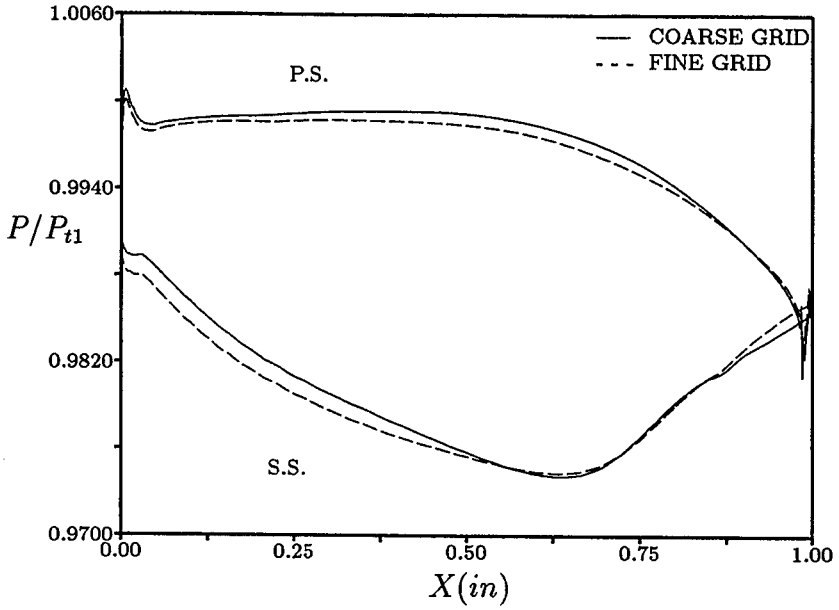

Figure 2: Surface pressure distribution for PAK B turbine - $Re = 40,000$, turbulent

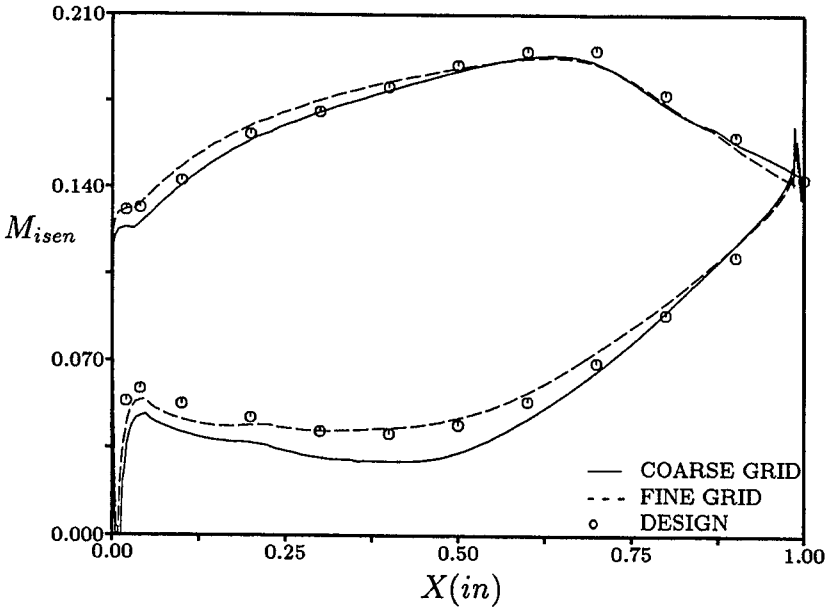

Figure 3: Surface (isentropic) Mach number distribution for PAK B turbine - $Re = 40,000$, turbulent

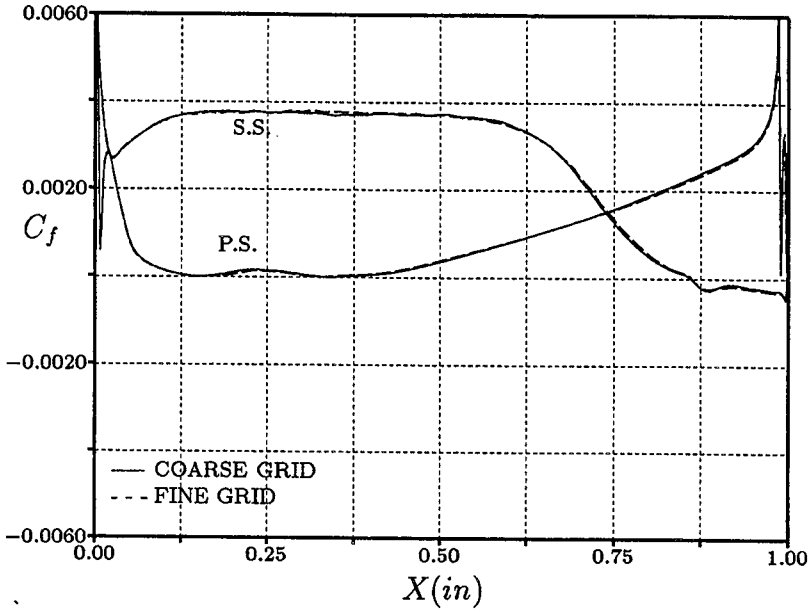

Figure 4: Skin friction distribution for PAK B turbine - $Re = 40,000$, turbulent

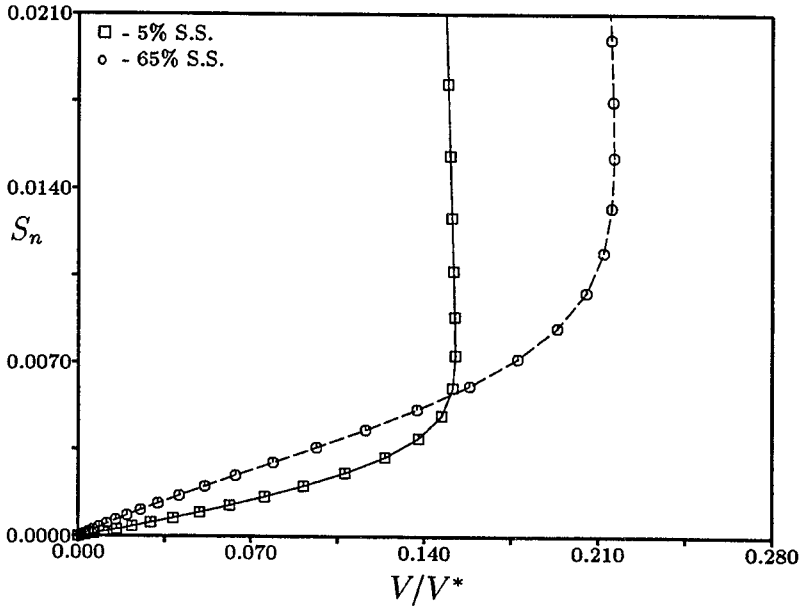

Figure 5: Suction surface velocity profiles for PAK B turbine - $Re = 40,000$, laminar

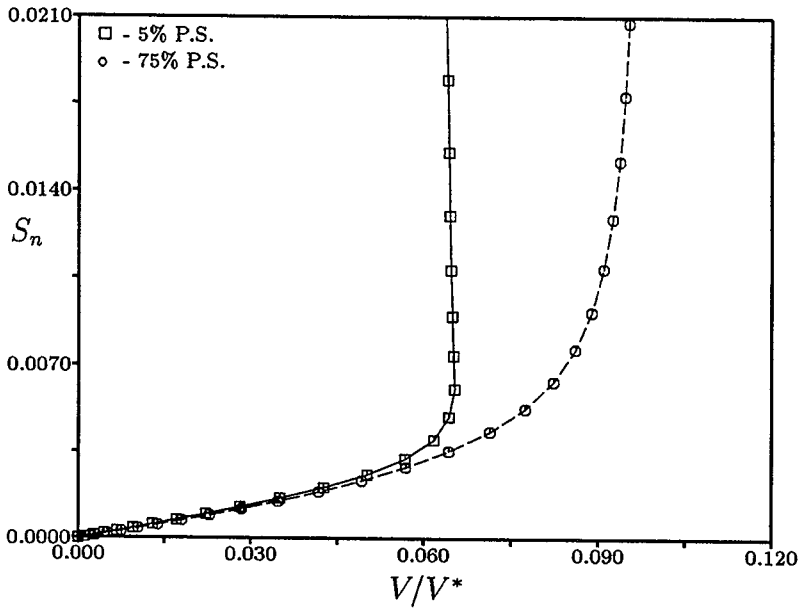

Figure 6: Pressure surface velocity profiles for PAK B turbine - $Re = 40,000$, laminar

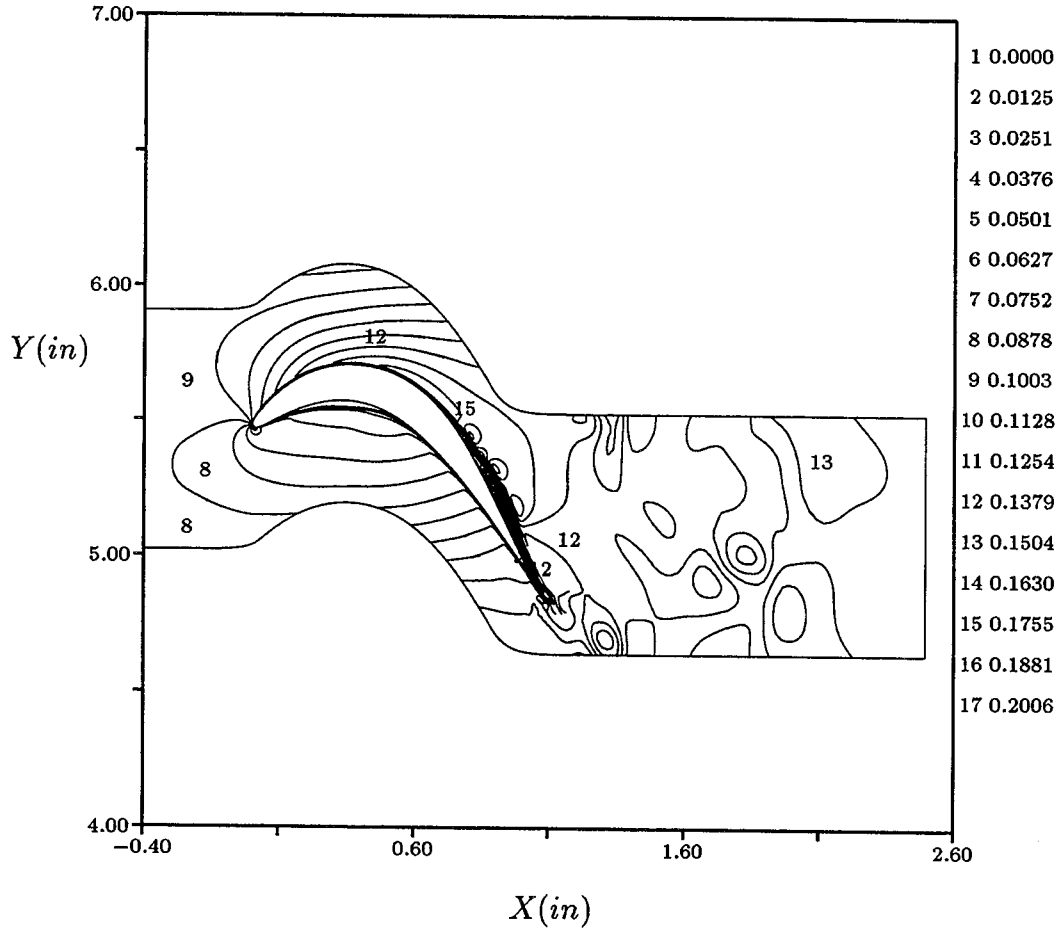

Figure 7: Instantaneous Mach number contours for PAK B turbine - $Re = 40,000$, laminar

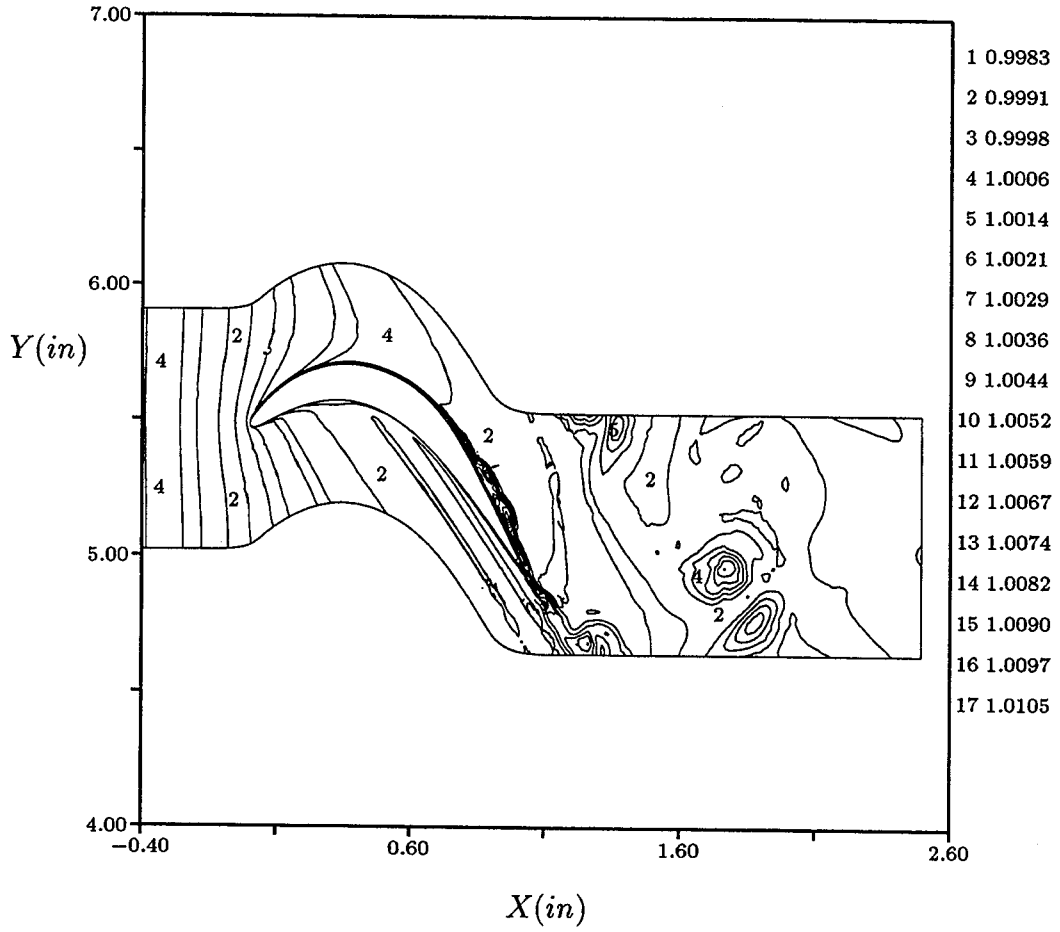

Figure 8: Instantaneous entropy contours for PAK B turbine - $Re = 40,000$, laminar

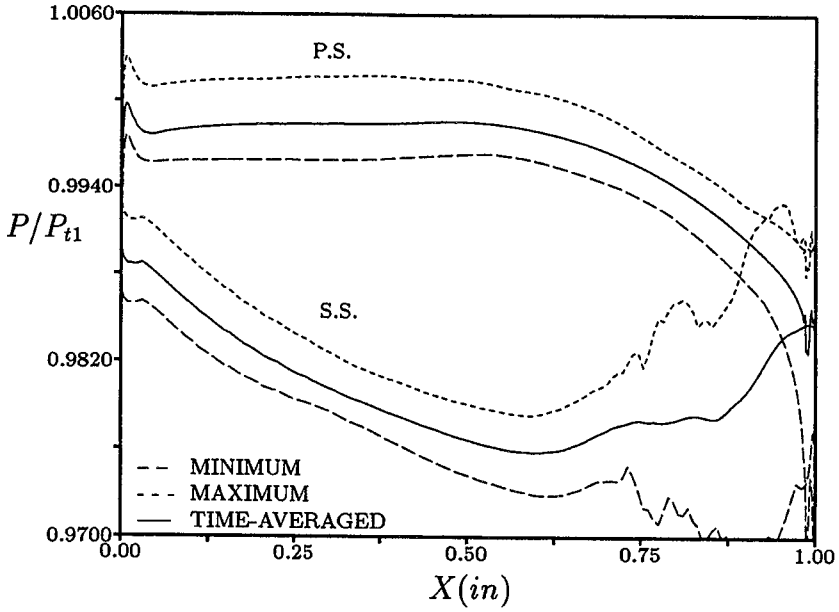

Figure 9: Surface pressure envelope for PAK B turbine - $Re = 40,000$, laminar

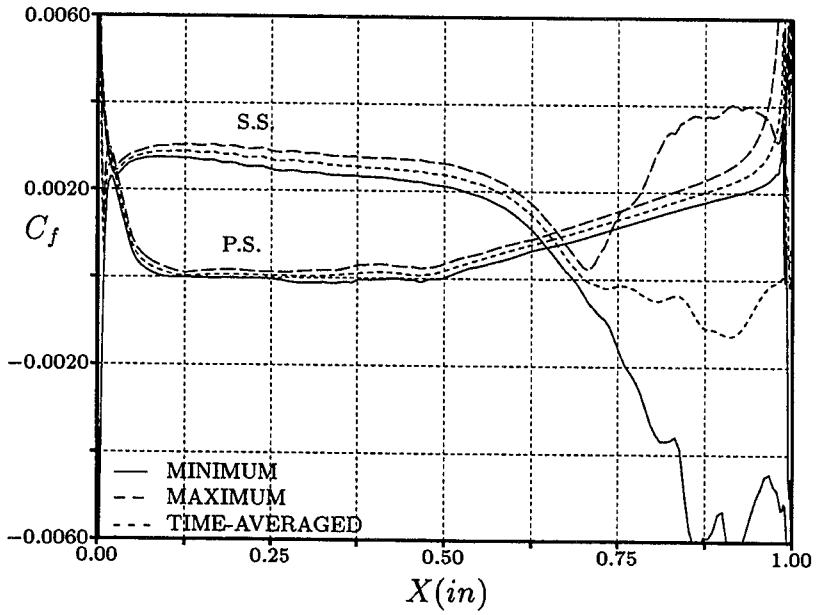

Figure 10: Skin-friction envelope for PAK B turbine - $Re = 40,000$, laminar

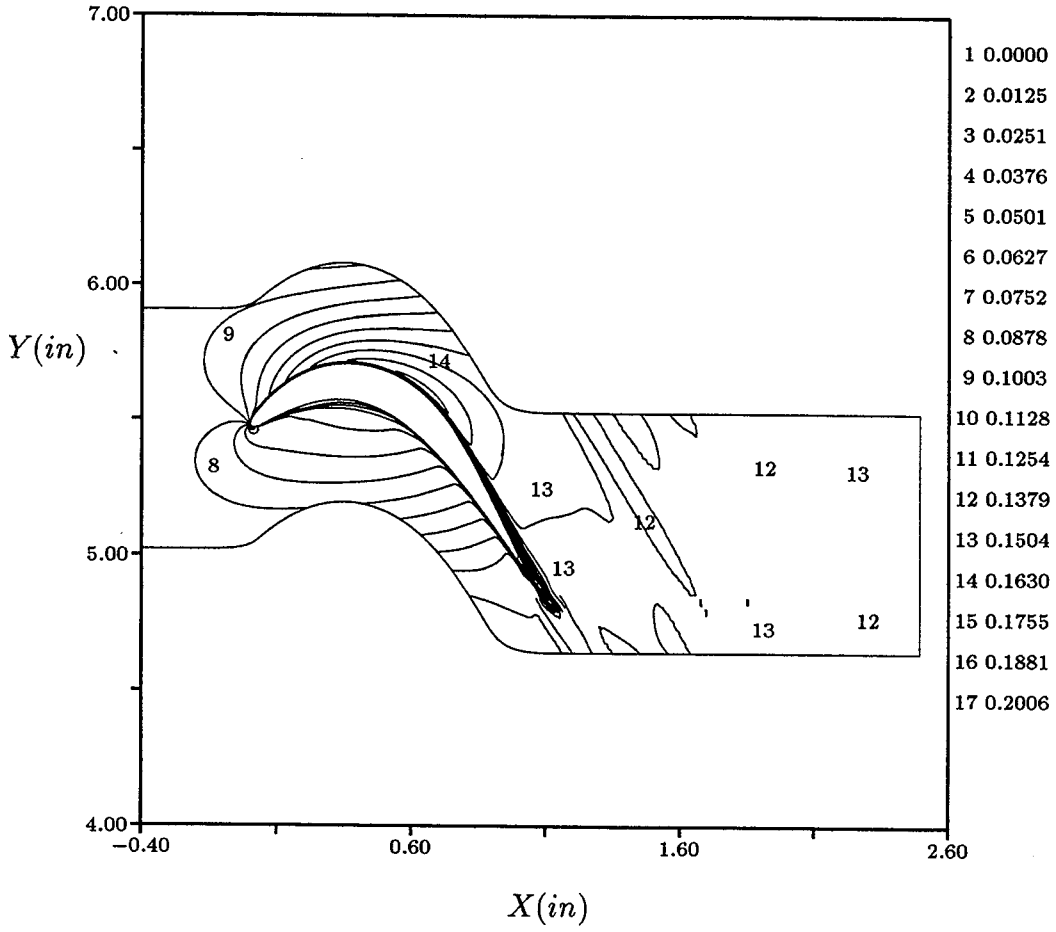

Figure 11: Instantaneous Mach number contours for PAK B turbine - $Re = 40,000$, transitional

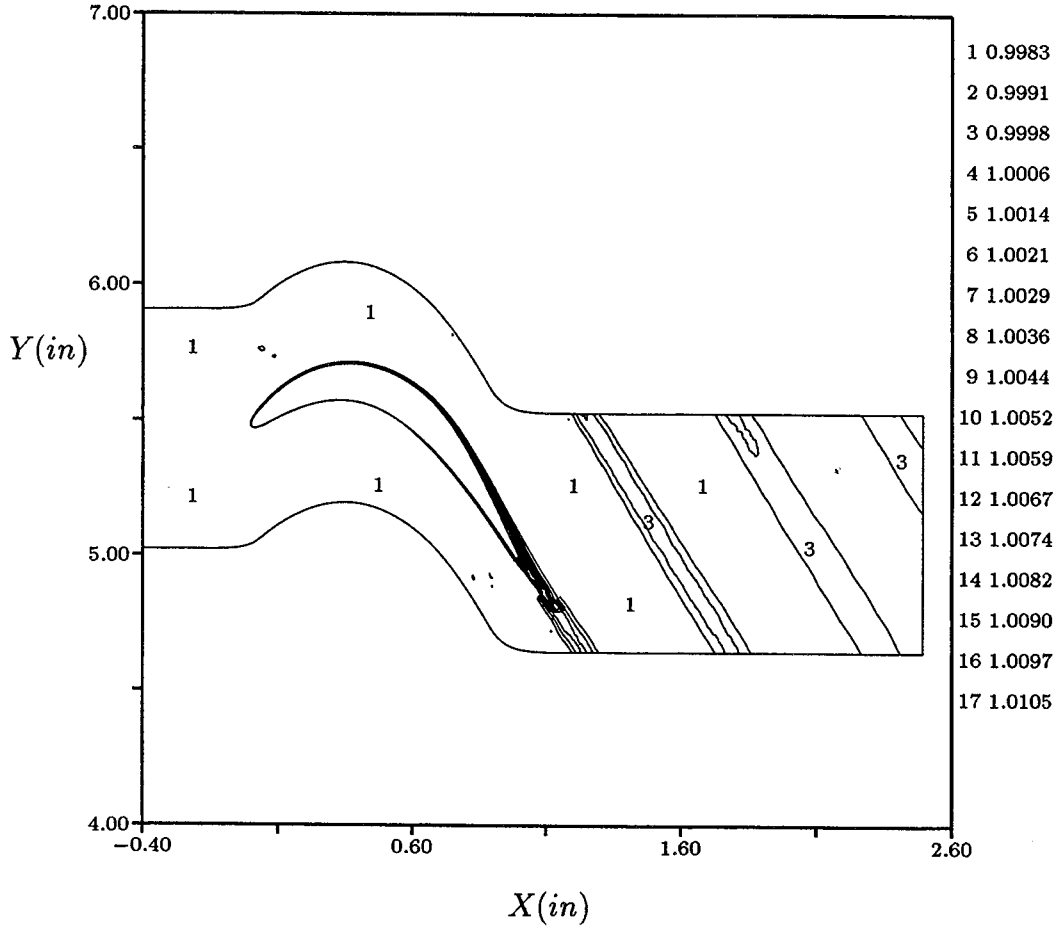

Figure 12: Instantaneous entropy contours for PAK B turbine - $Re = 40,000$, transitional

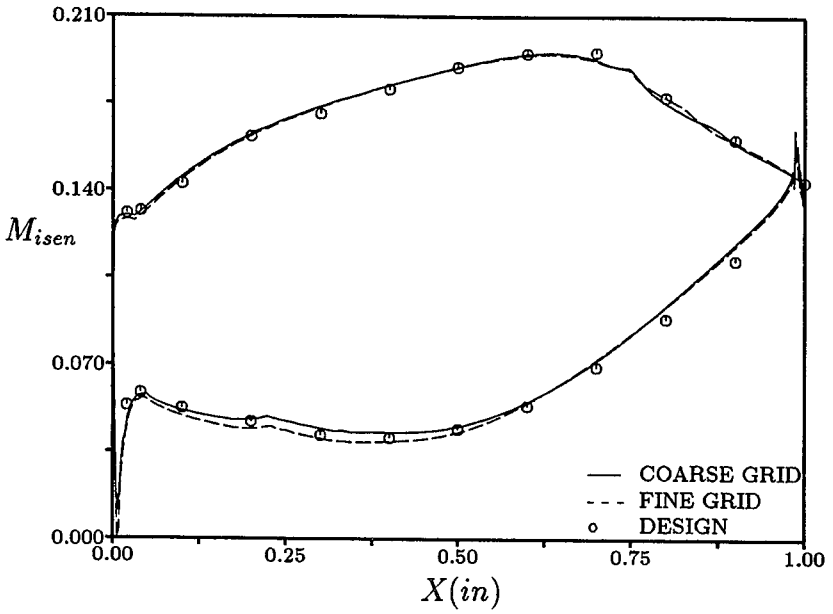

Figure 13: Surface (isentropic) Mach number distribution for PAK B turbine - $Re = 40,000$, transitional

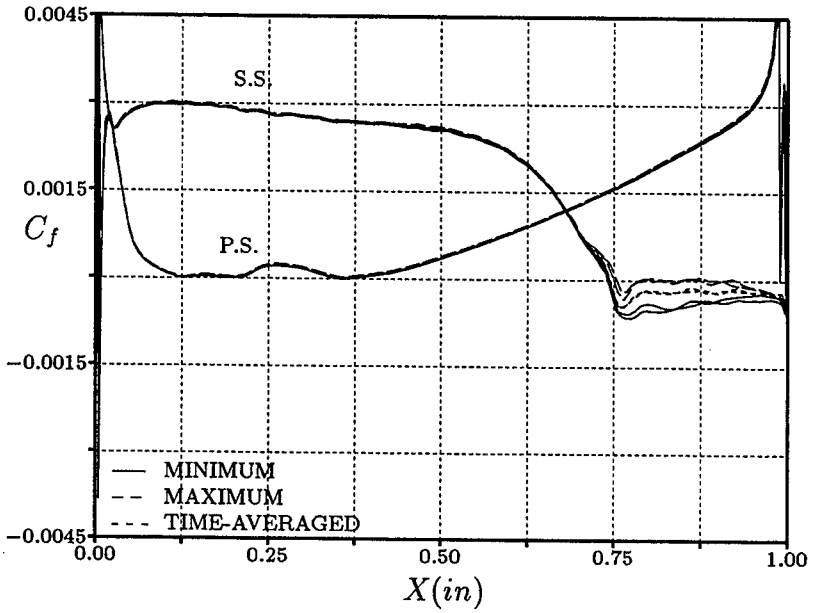

Figure 14: Skin friction distribution for PAK B turbine - $Re = 40,000$, transitional

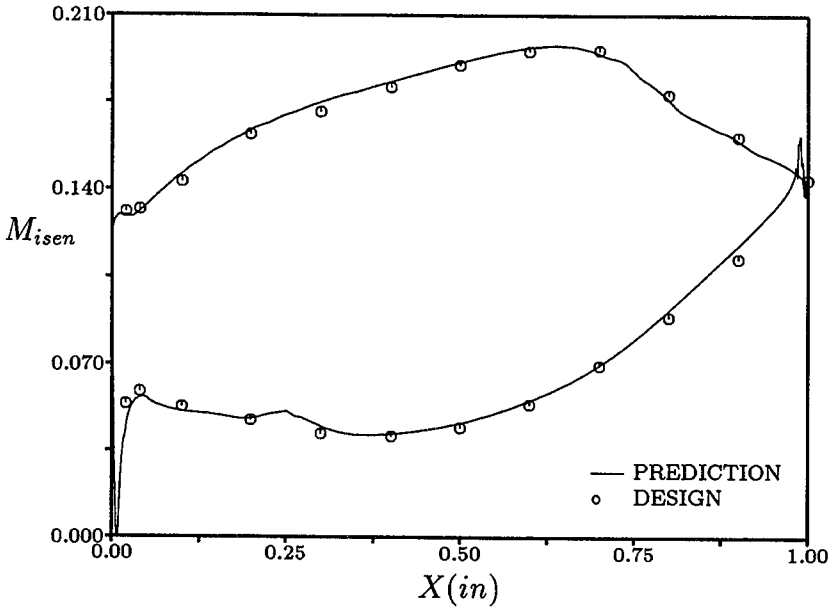

Figure 15: Surface (isentropic) Mach number distribution for the PAK B turbine blade - $Re = 120,000$, fixed transition

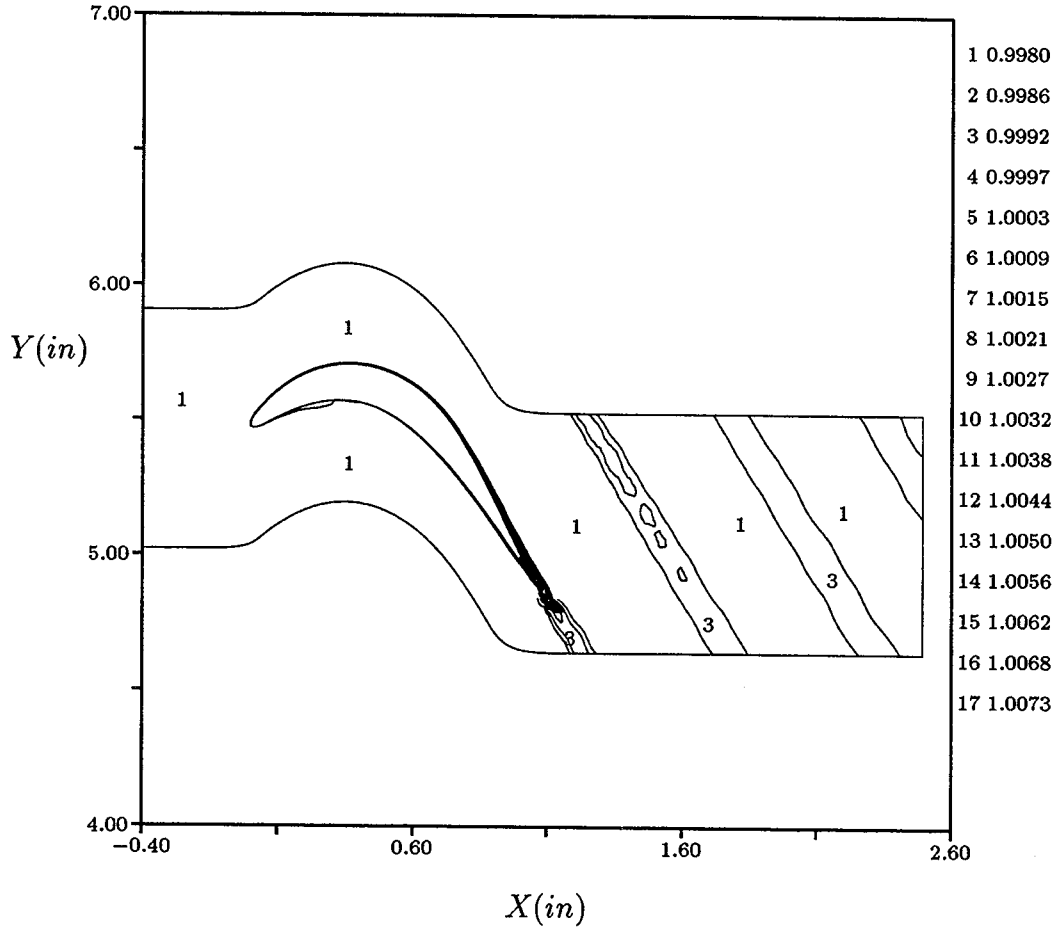

Figure 16: Instantaneous entropy contours for the PAK B turbine blade - $Re = 120,000$, fixed transition

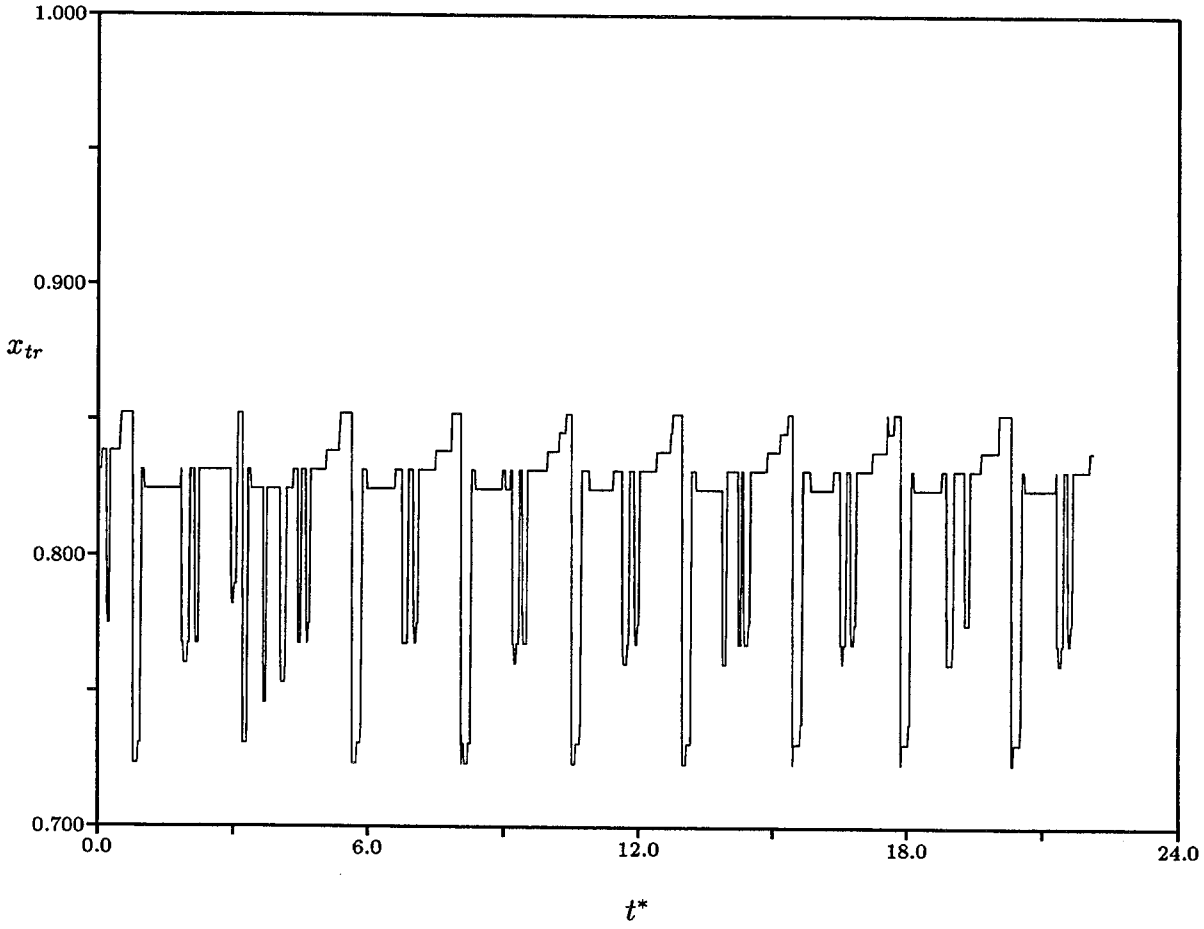

Figure 17: Suction surface transition location for the PAK B turbine blade - $Re = 200,000$

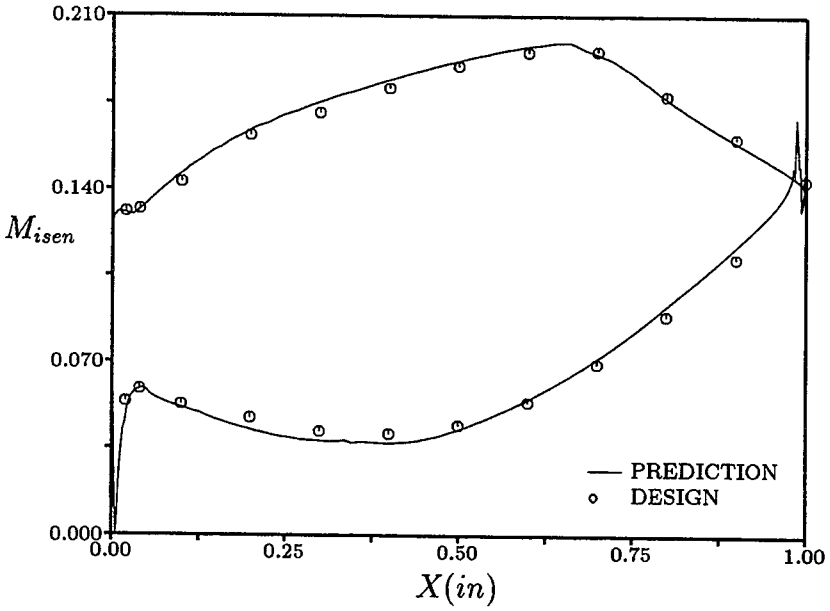

Figure 18: Surface (isentropic) Mach number distribution for the PAK B turbine blade - $Re = 200,000$, fixed transition

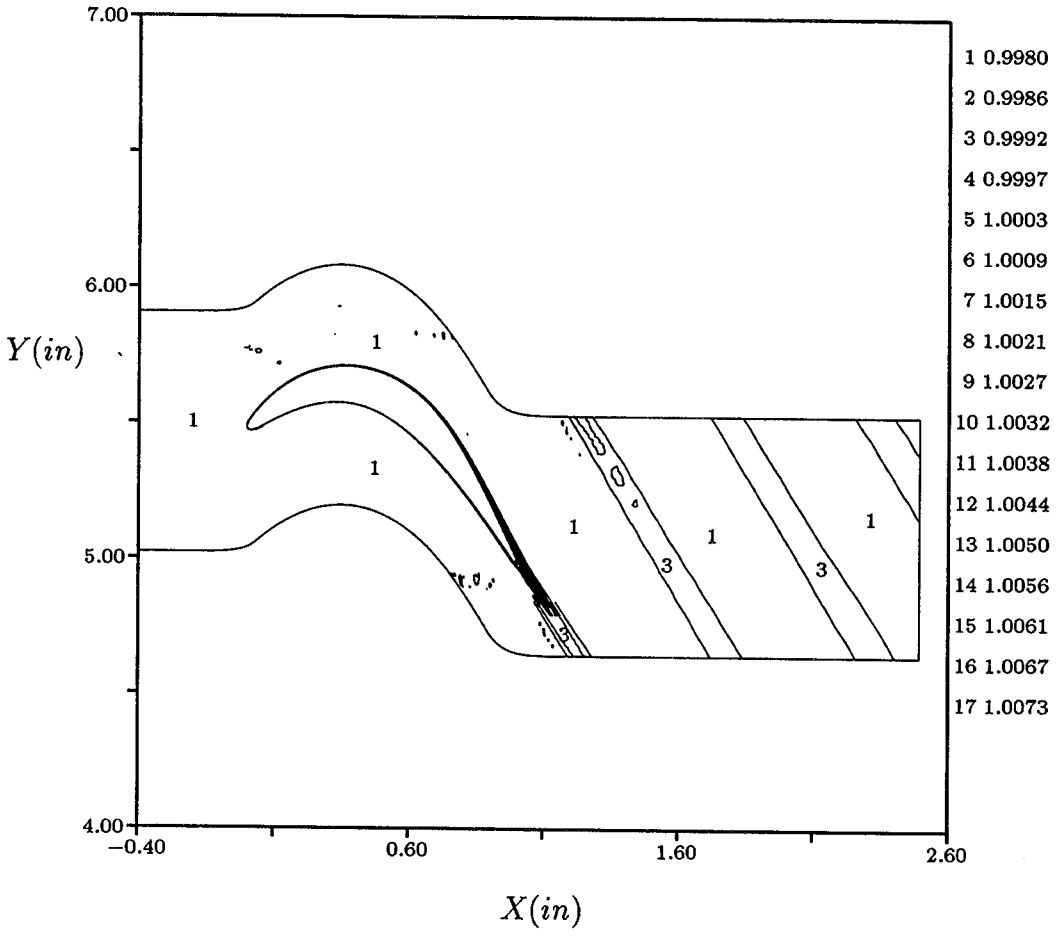

Figure 19: Instantaneous entropy contours for the PAK B turbine blade - $Re = 200,000$, fixed transition

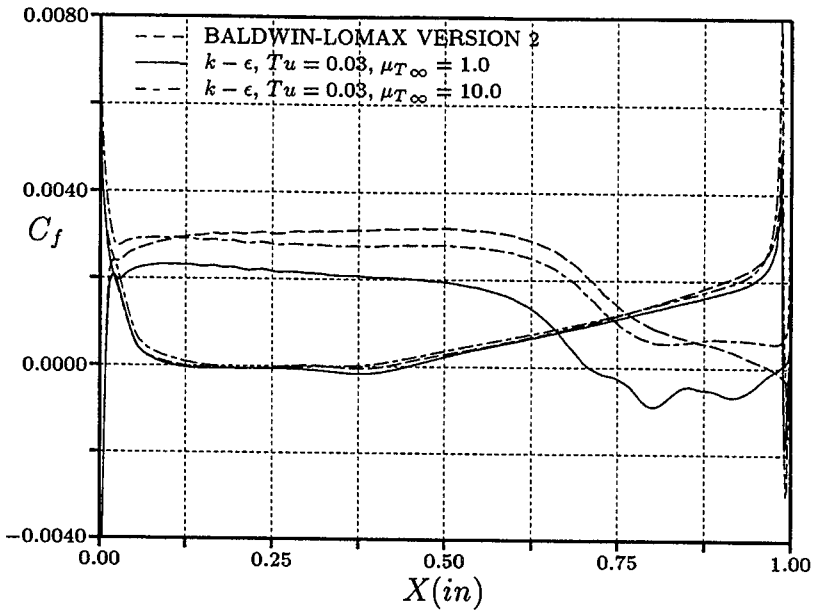

Figure 20: Turbulence model effects on the skin friction for PAK B turbine blade - $Re = 80,000$; $Tu = 3\%$

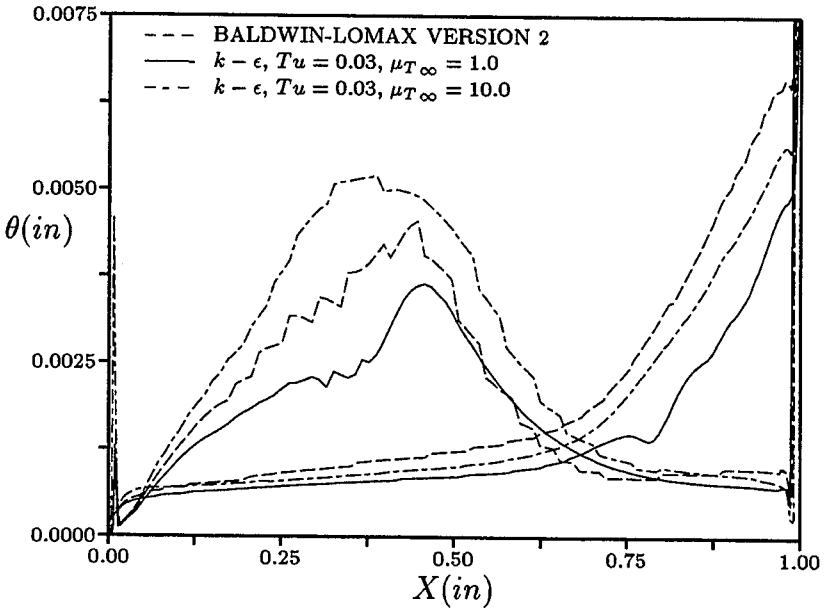

Figure 21: Turbulence model effects on the momentum thickness for the PAK B turbine blade - $Re = 80,000$; $Tu = 3\%$

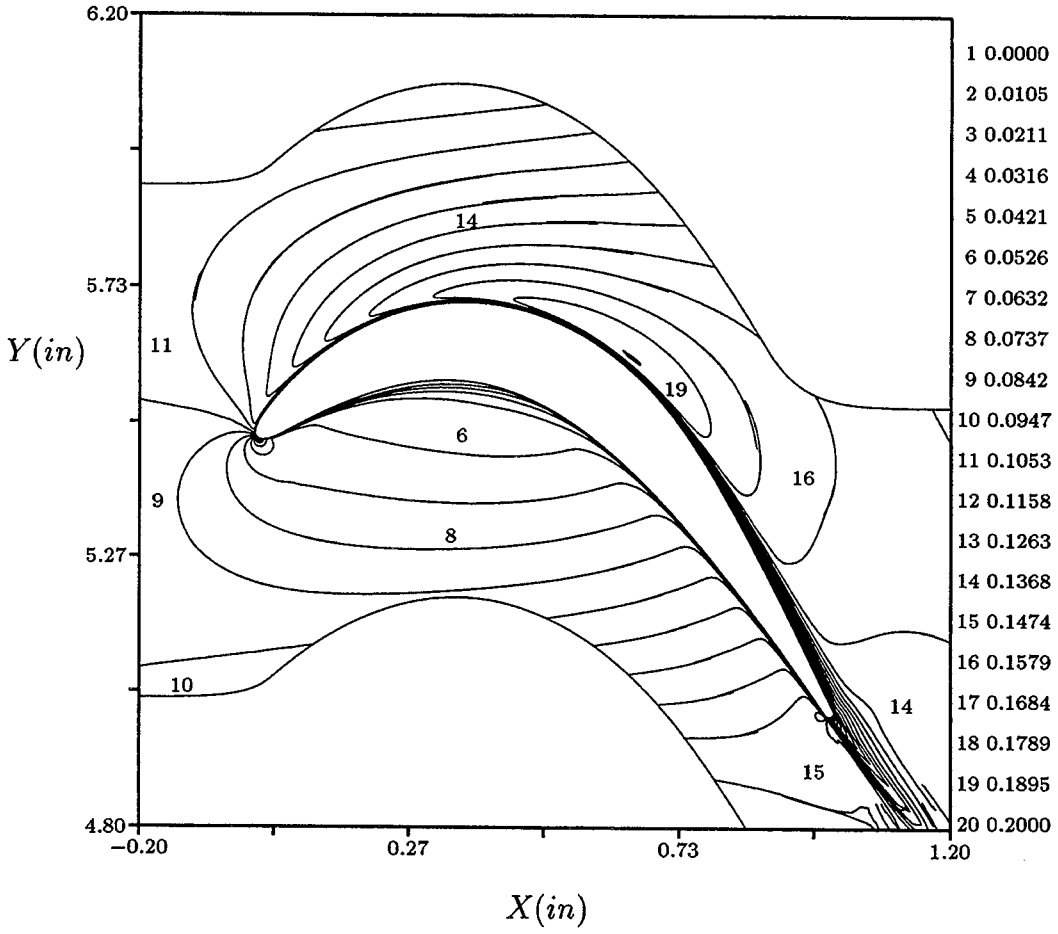

Figure 22: Mach number contours for the PAK B turbine blade - $Re = 80,000$; $Tu = 3\%$; $\mu_{T_\infty} = 10.0$

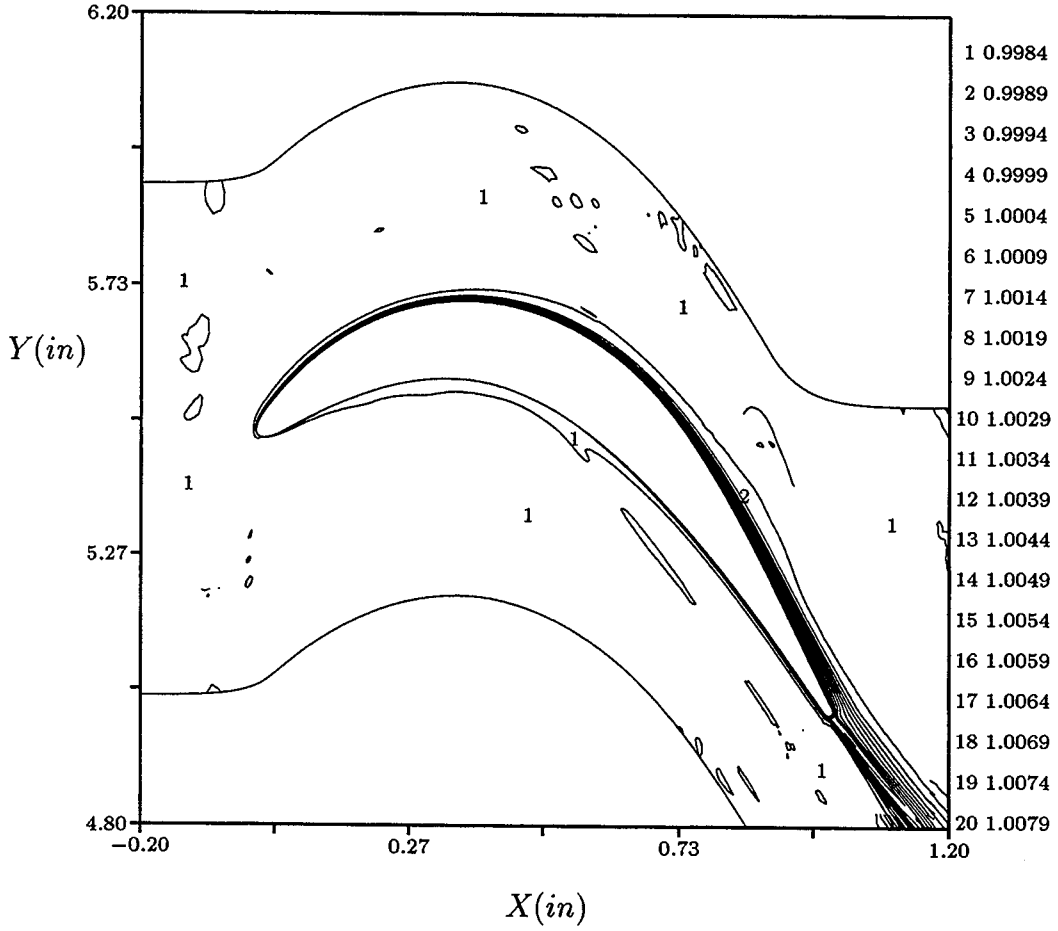

Figure 23: Entropy contours for the PAK B turbine blade - $Re = 80,000$; $Tu = 3\%$; $\mu_{T_\infty} = 10.0$

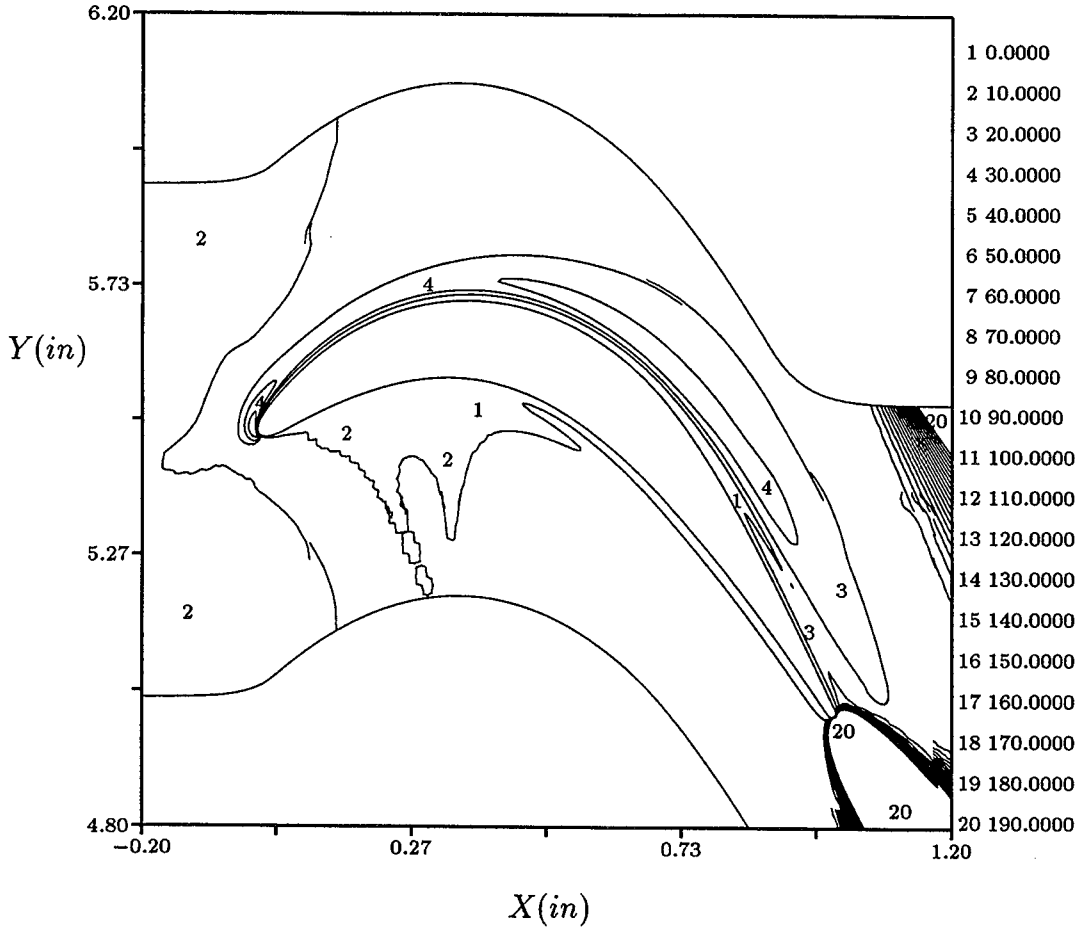

Figure 24: Turbulent viscosity contours for the PAK B turbine blade - $Re = 80,000$; $Tu = 3\%$; $\mu_{T_\infty} = 10.0$

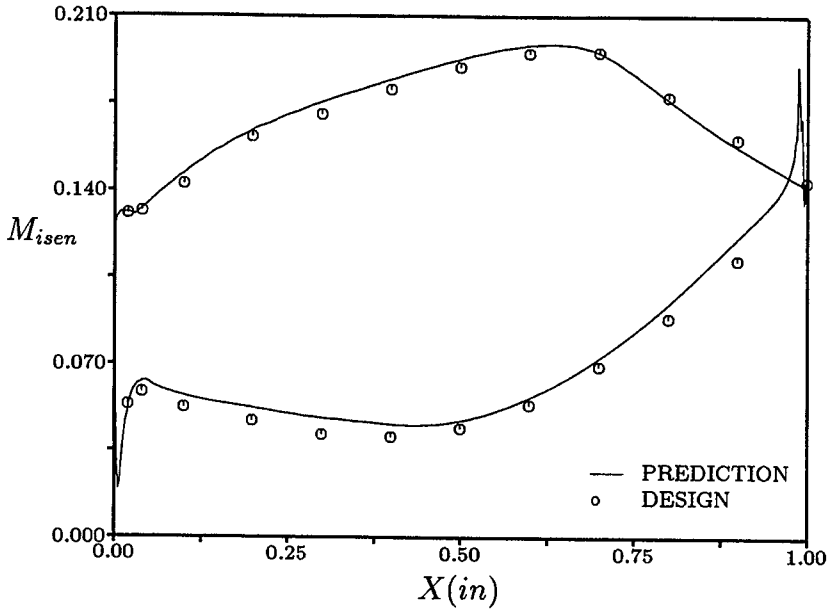

Figure 25: Surface (isentropic) Mach number - $Re = 80,000$; $Tu = 3\%$; $\mu_{T\infty} = 10.0$

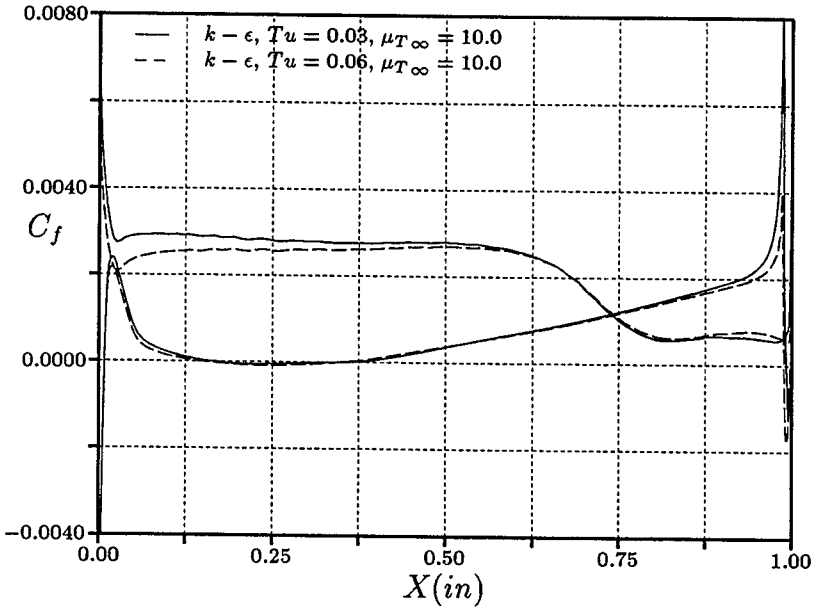

Figure 26: Free stream turbulence effects on the skin friction for PAK B turbine blade - $Re = 80,000$; Tu =3%,6%

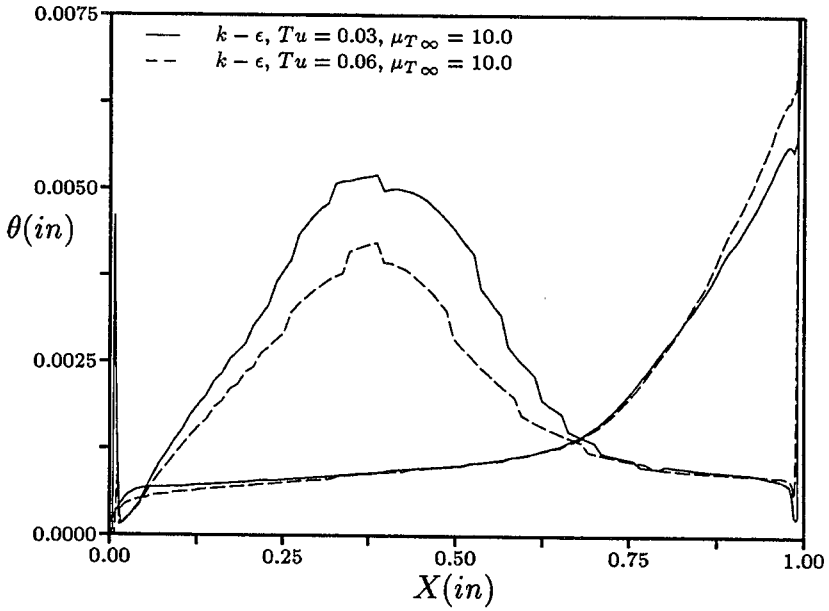

Figure 27: Free stream turbulence effects on the momentum thickness for the PAK B turbine blade - $Re = 80,000$; Tu =3%,6%

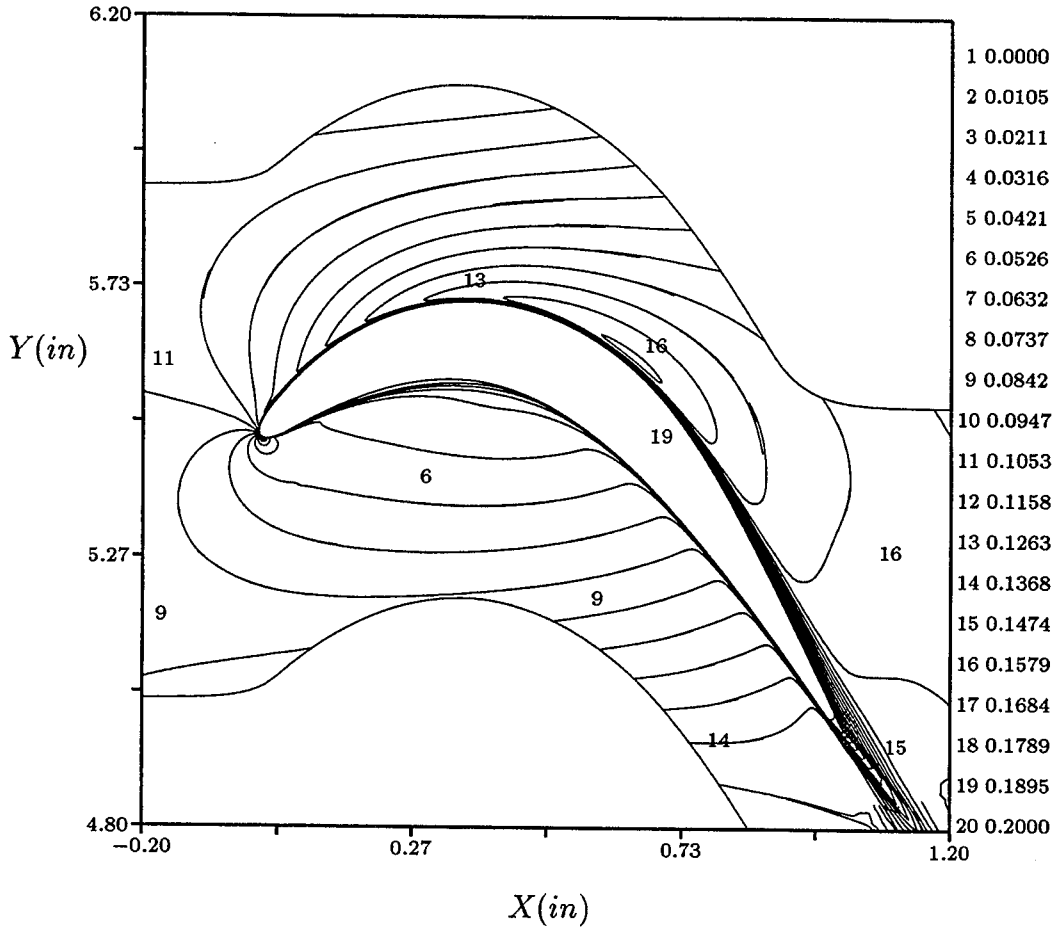

Figure 28: Mach number contours for the PAK B turbine blade - $Re = 80,000$; $Tu = 6\%$; $\mu_{T\infty} = 10.0$

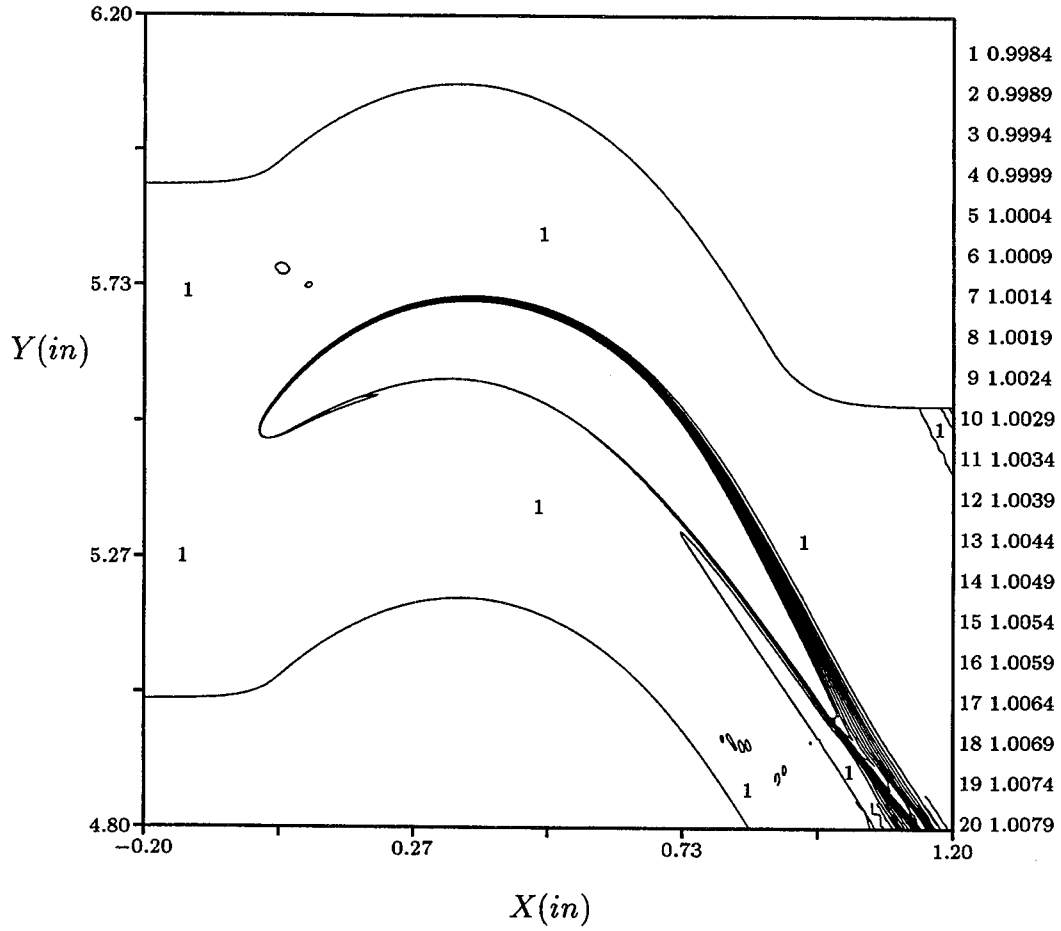

Figure 29: Entropy contours for the PAK B turbine blade - $Re = 80,000$; $Tu = 6\%$; $\mu_{T\infty} = 10.0$

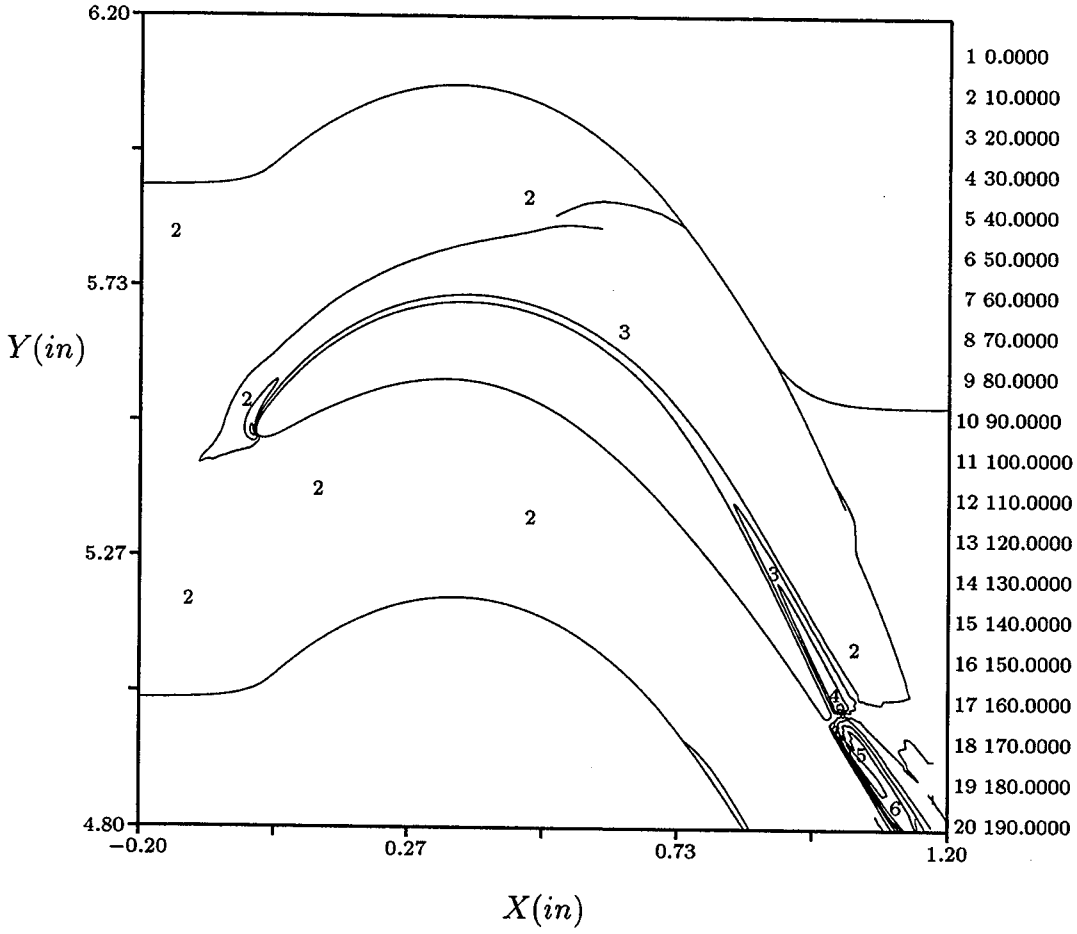

Figure 30: Turbulent viscosity contours for the PAK B turbine blade - $Re = 80,000$; $Tu = 6\%$; $\mu_{T_\infty} = 10.0$

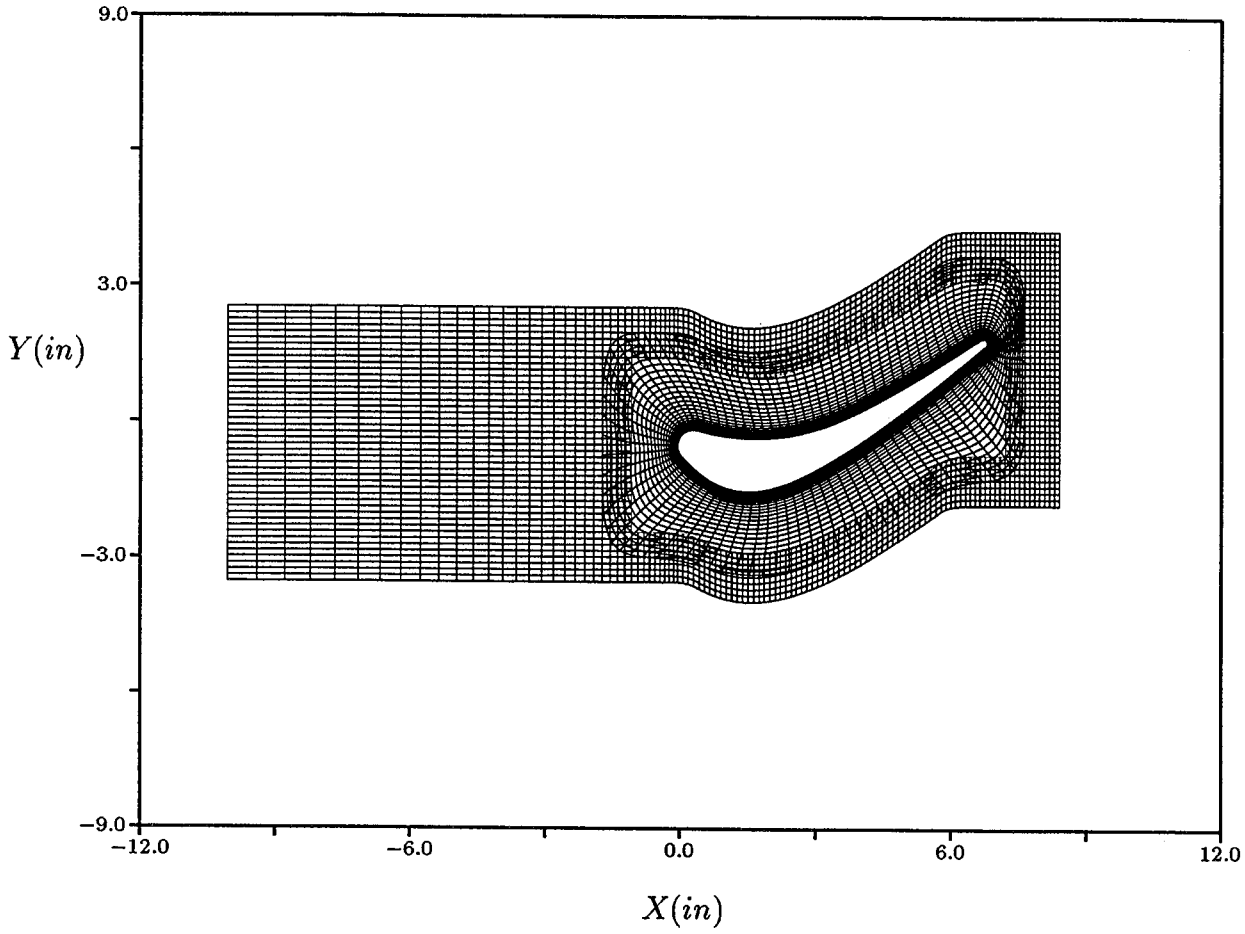

Figure 31: Modified LSRR geometry used to generate wake

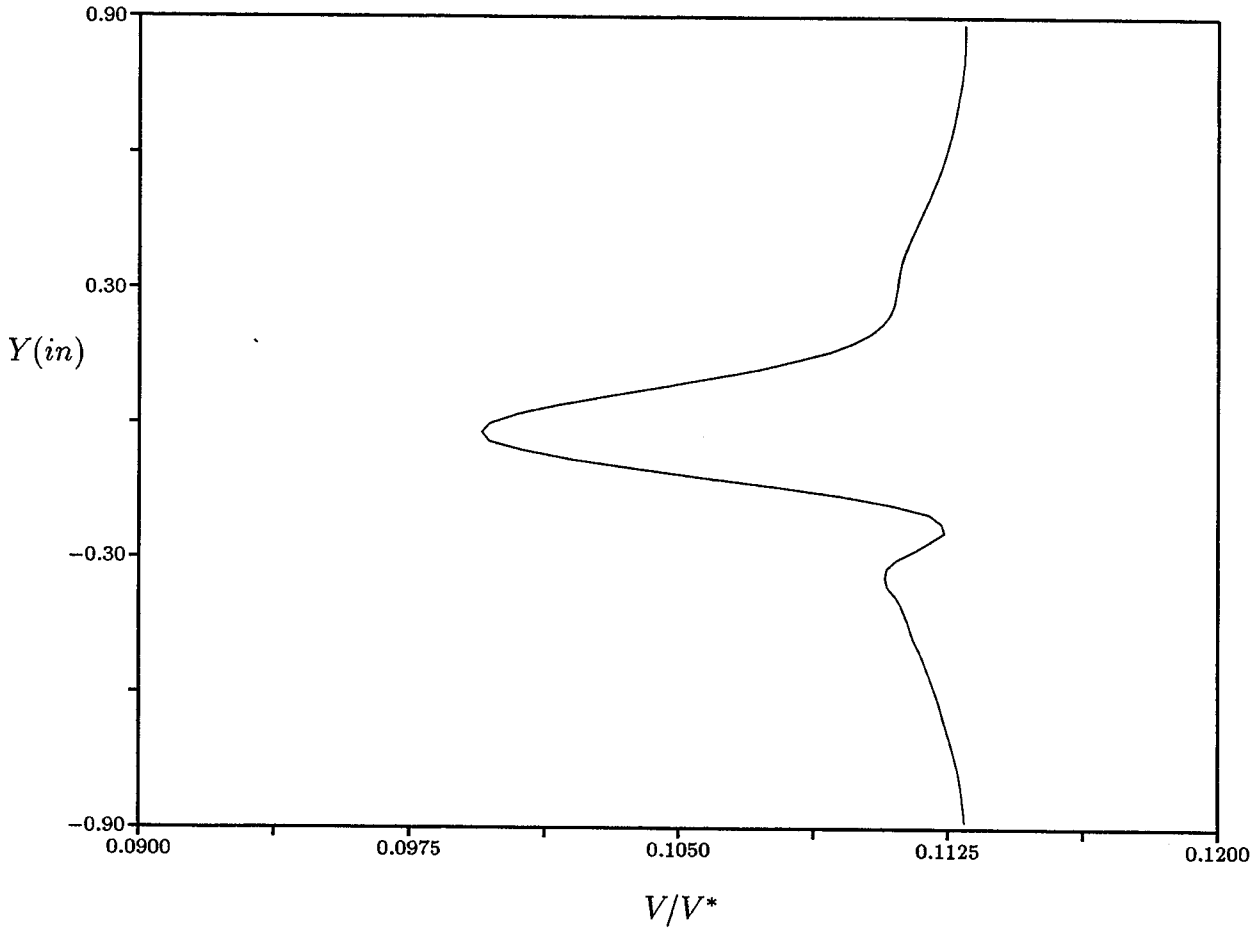

Figure 32: Wake generated by LSRR geometry

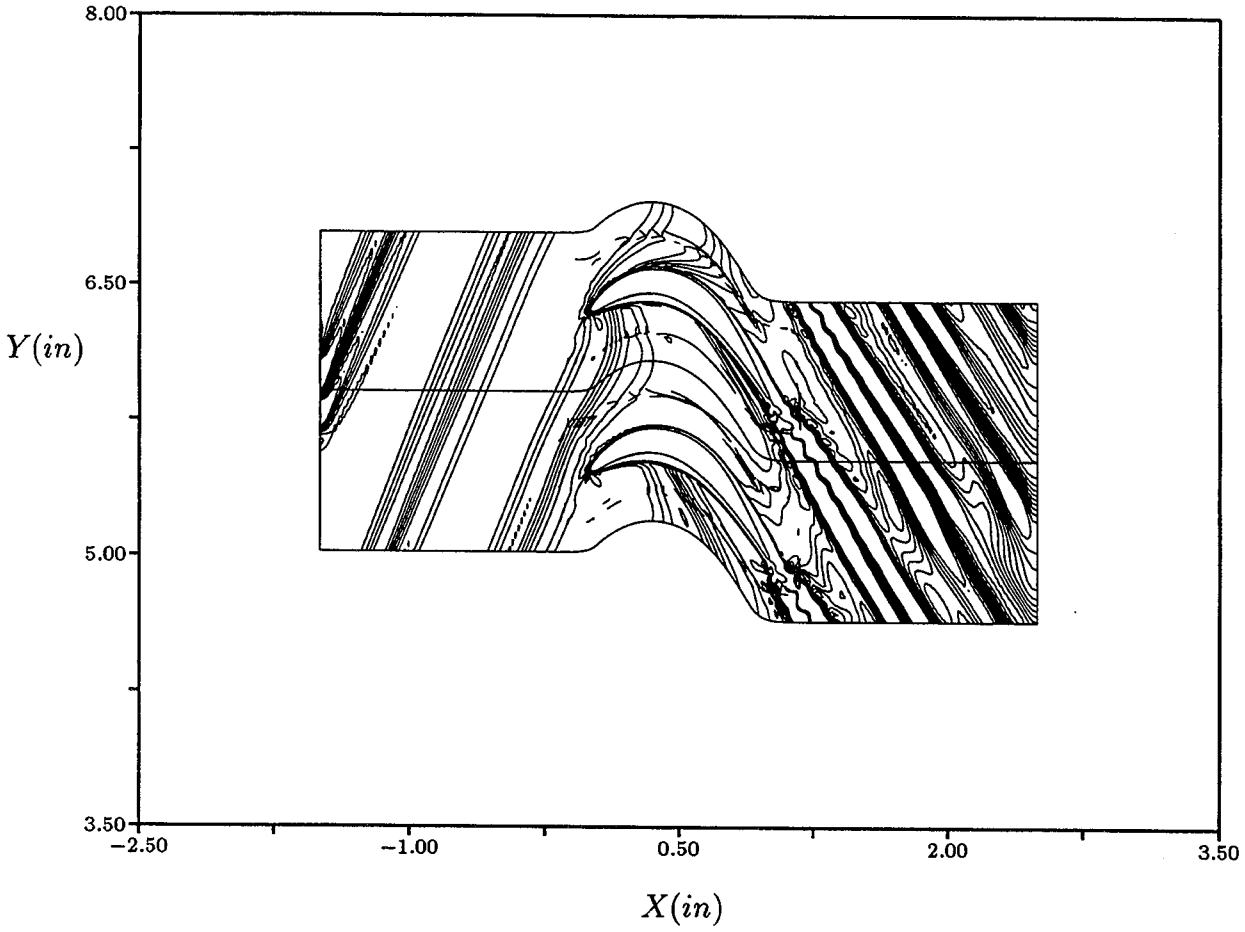

Figure 33: Perturbation vorticity contours for the PAK B turbine - $Re = 40,000$, LSRR stator wake, fixed transition

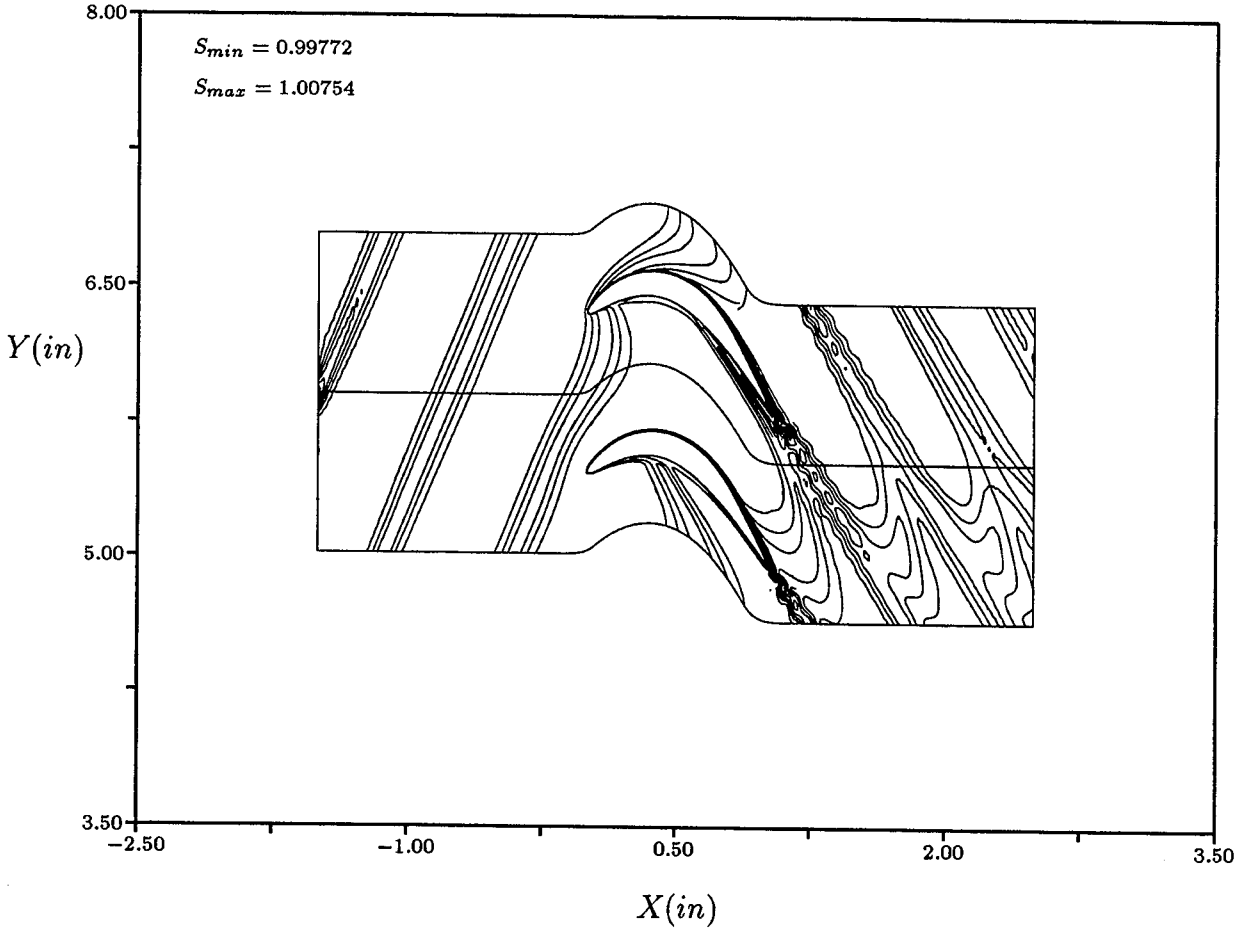

Figure 34: Instantaneous entropy contours for the PAK B turbine - $Re = 40,000$, LSRR stator wake, fixed transition

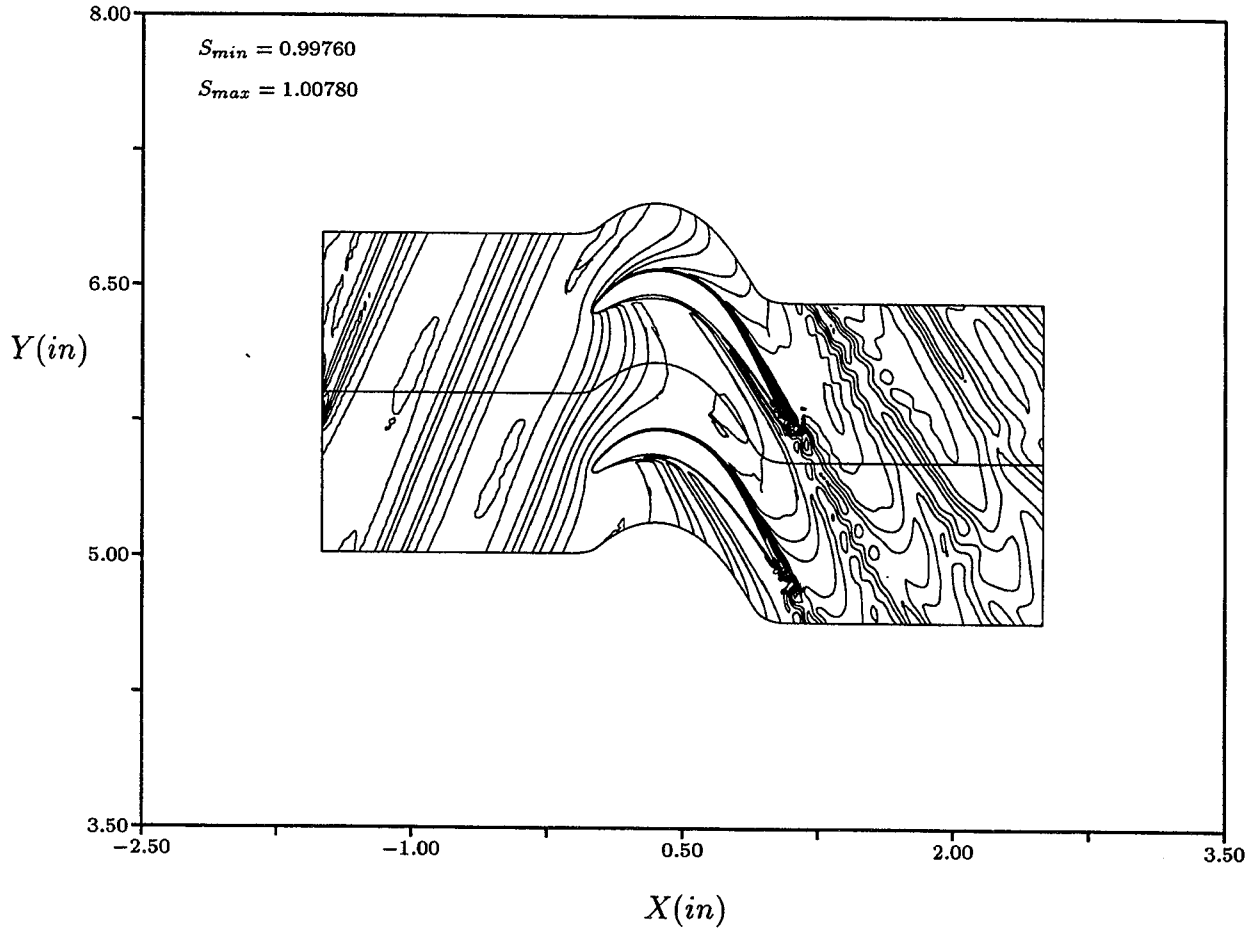

Figure 35: Instantaneous entropy contours for the PAK B turbine - $Re = 40,000$, LSRR stator wake, floating transition

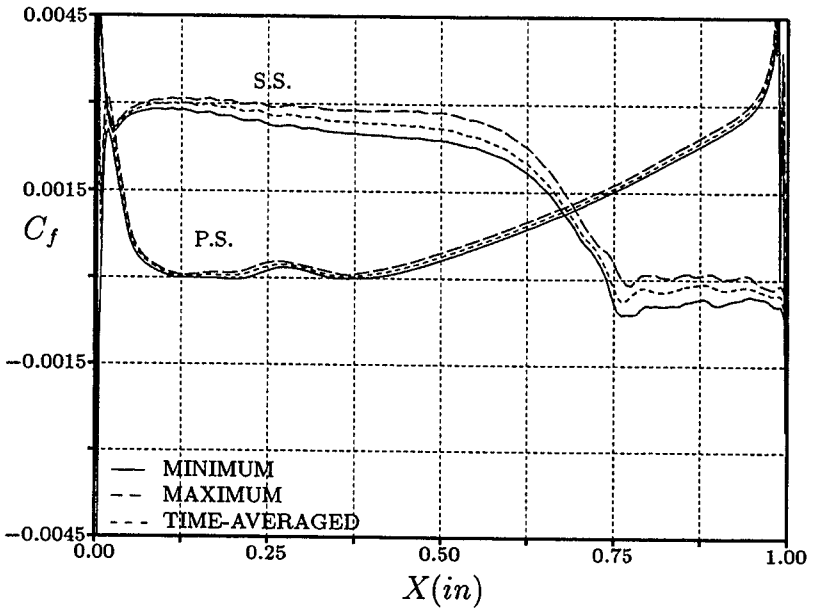

Figure 36: Unsteady skin friction envelope for the PAK B turbine - $Re = 40,000$, LSRR stator wake, fixed transition

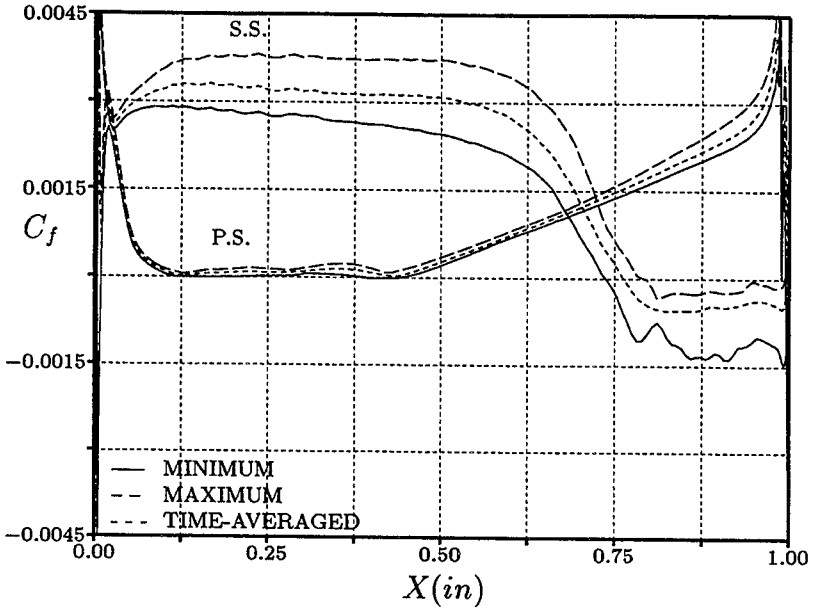

Figure 37: Unsteady skin friction envelope for the PAK B turbine - $Re = 40,000$, LSRR stator wake, floating transition

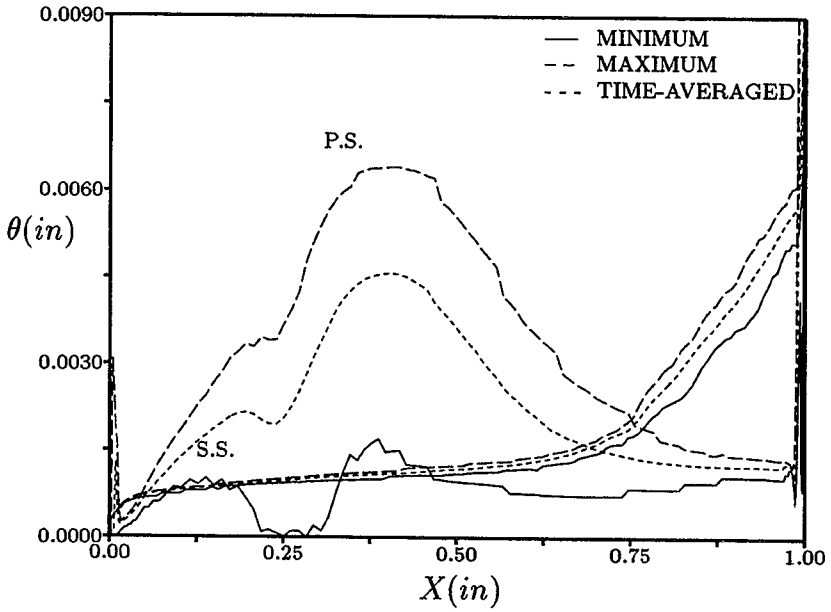

Figure 38: Unsteady momentum thickness envelope for the PAK B turbine - $Re = 40,000$, LSRR stator wake, fixed transition

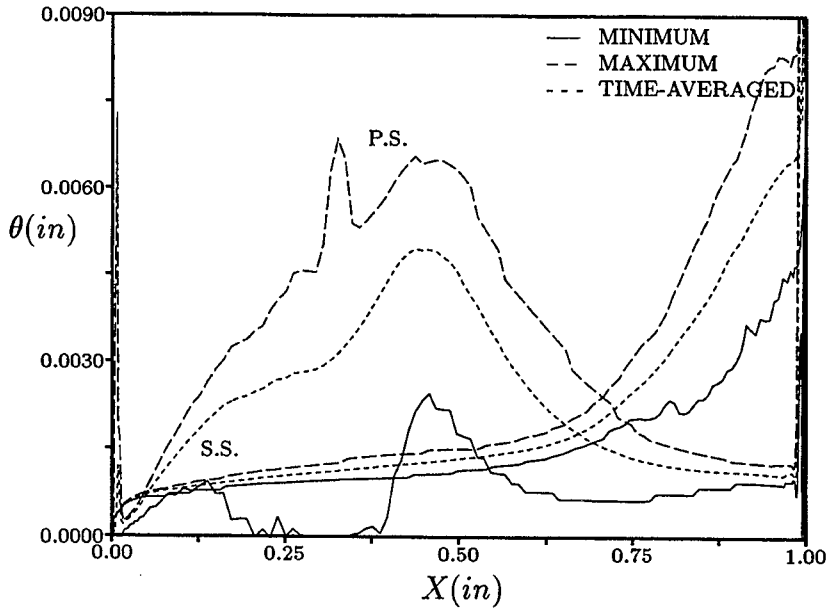

Figure 39: Unsteady momentum thickness envelope for the PAK B turbine - $Re = 40,000$, LSRR stator wake, floating transition

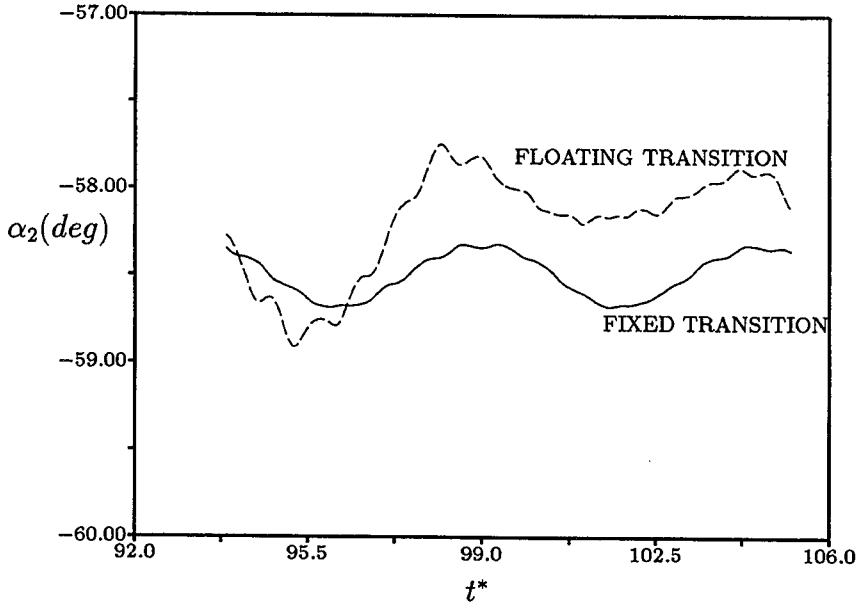

Figure 40: Exit flow angle variation for the PAK B turbine - $Re = 40,000$, LSRR stator wake

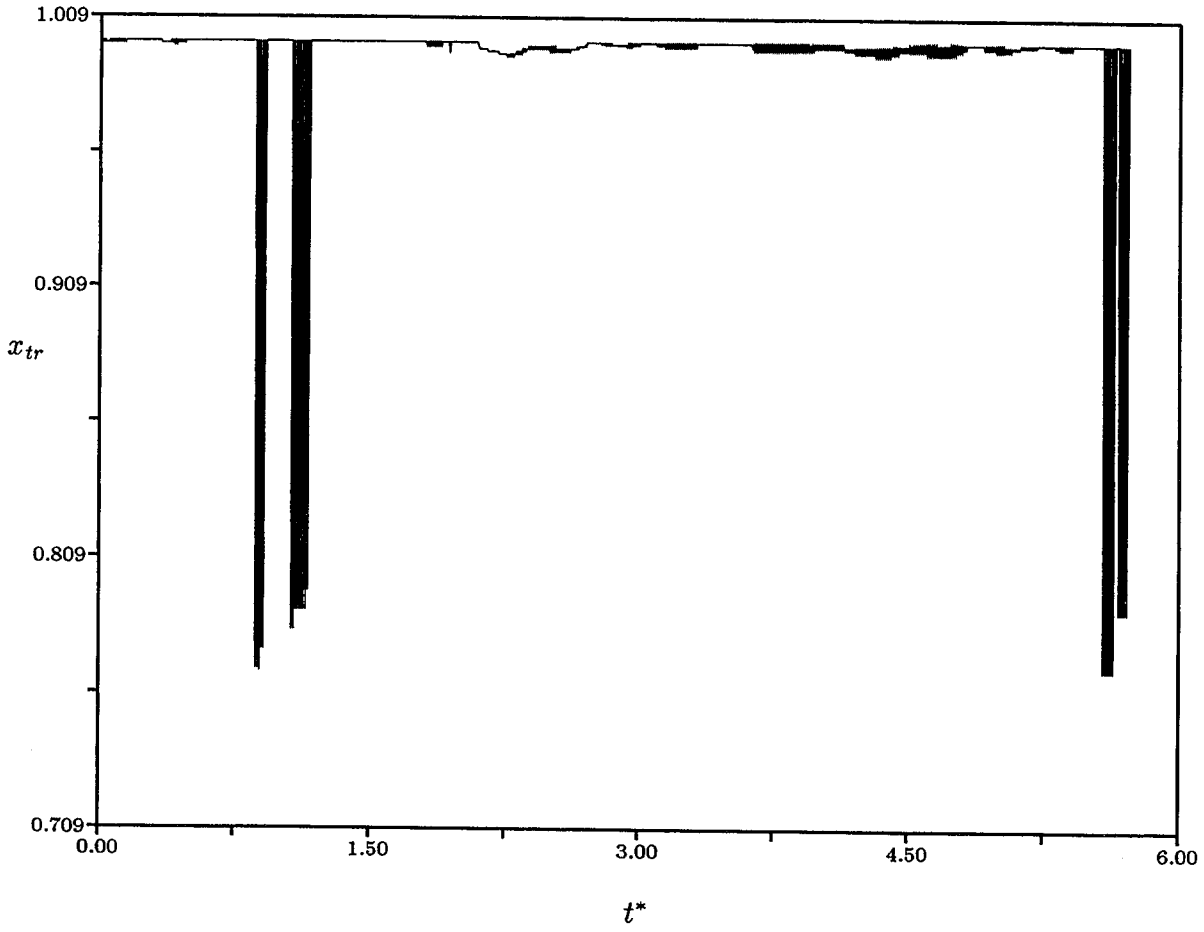

Figure 41: Time-variation of suction surface transition location - $Re = 40,000$, LSRR stator wake

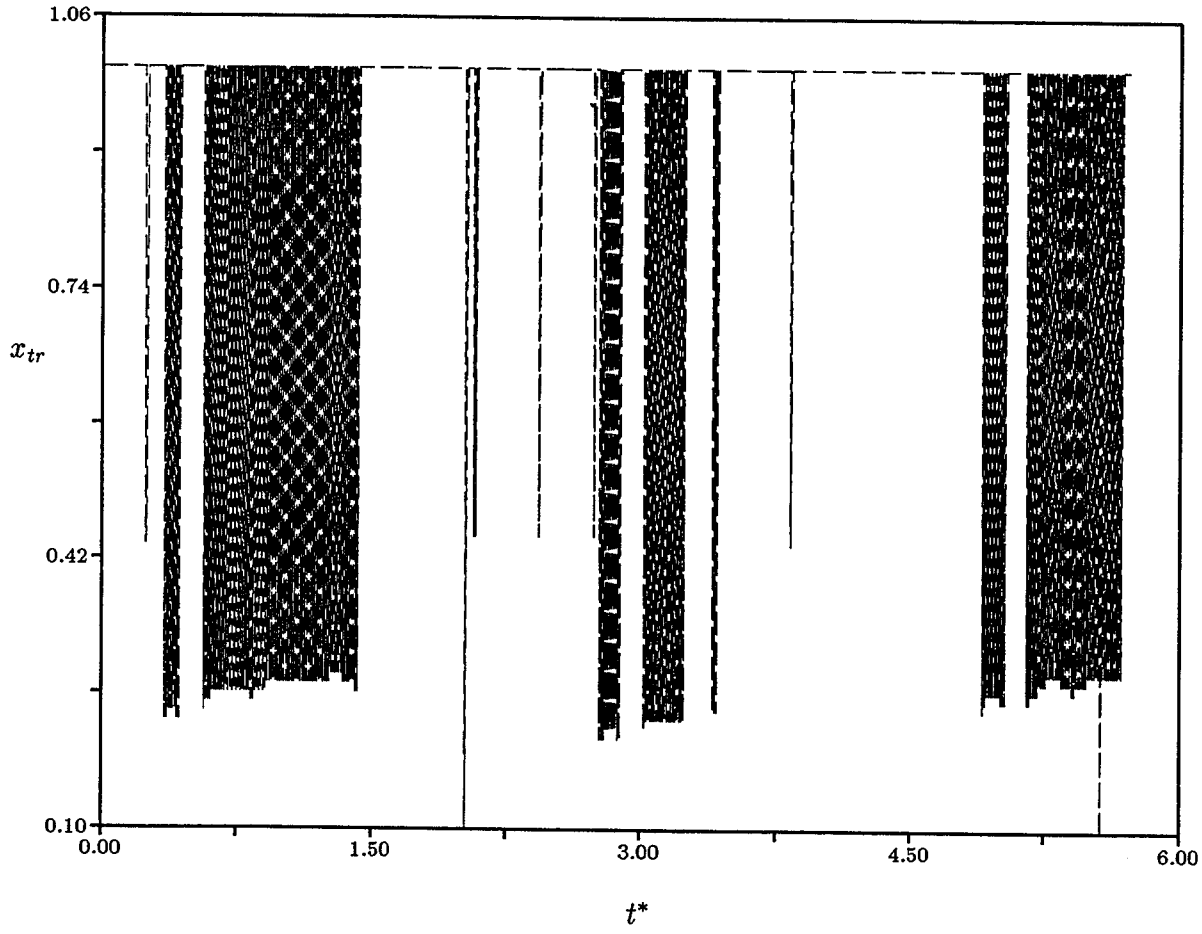

Figure 42: Time-variation of pressure surface transition location - $Re = 40,000$, LSRR stator wake

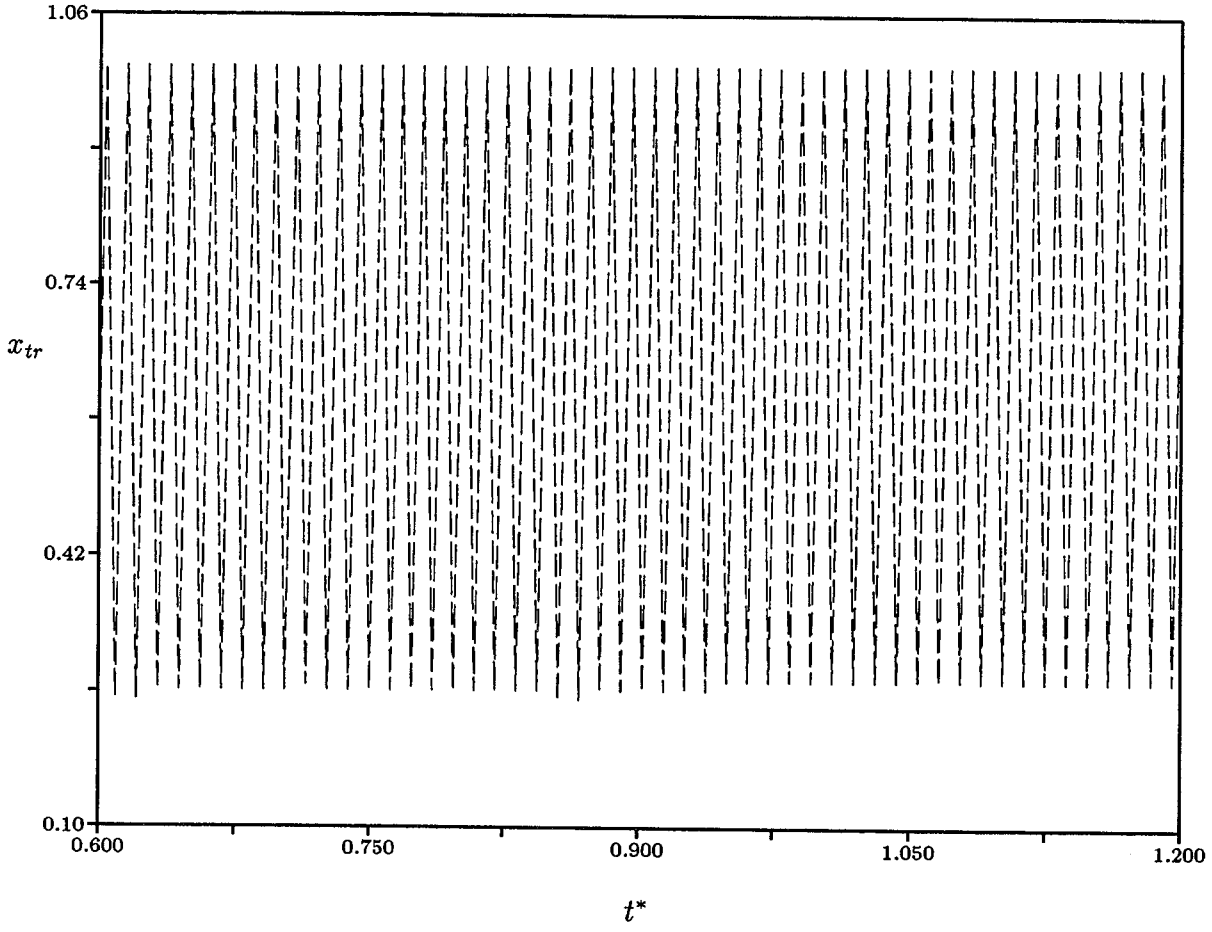

Figure 43: Close-up of time-variation of pressure surface transition location - $Re = 40,000$, LSRR stator wake

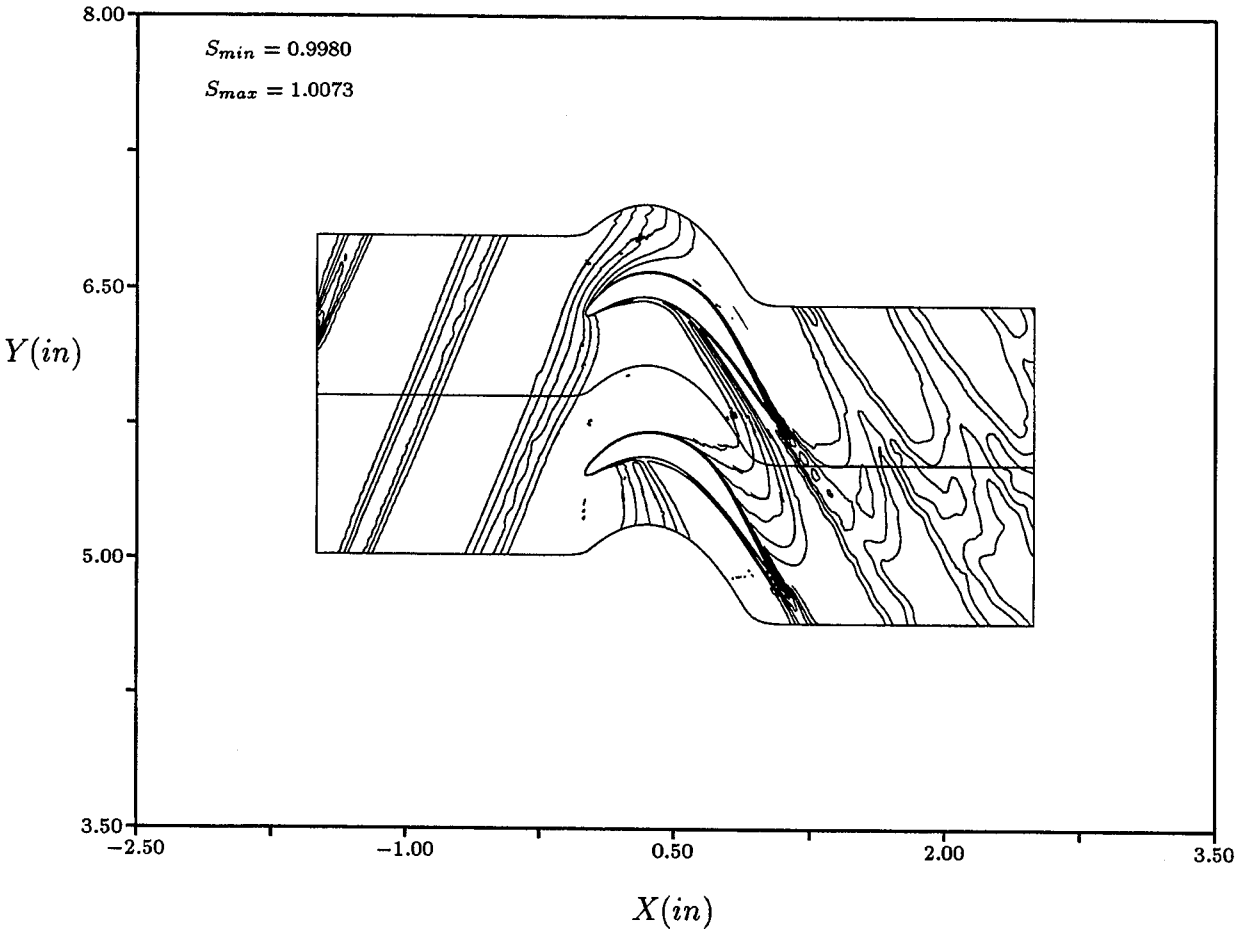

Figure 44: Instantaneous entropy contours for the PAK B turbine blade - $Re = 120,000$, LSRR stator wake, fixed transition

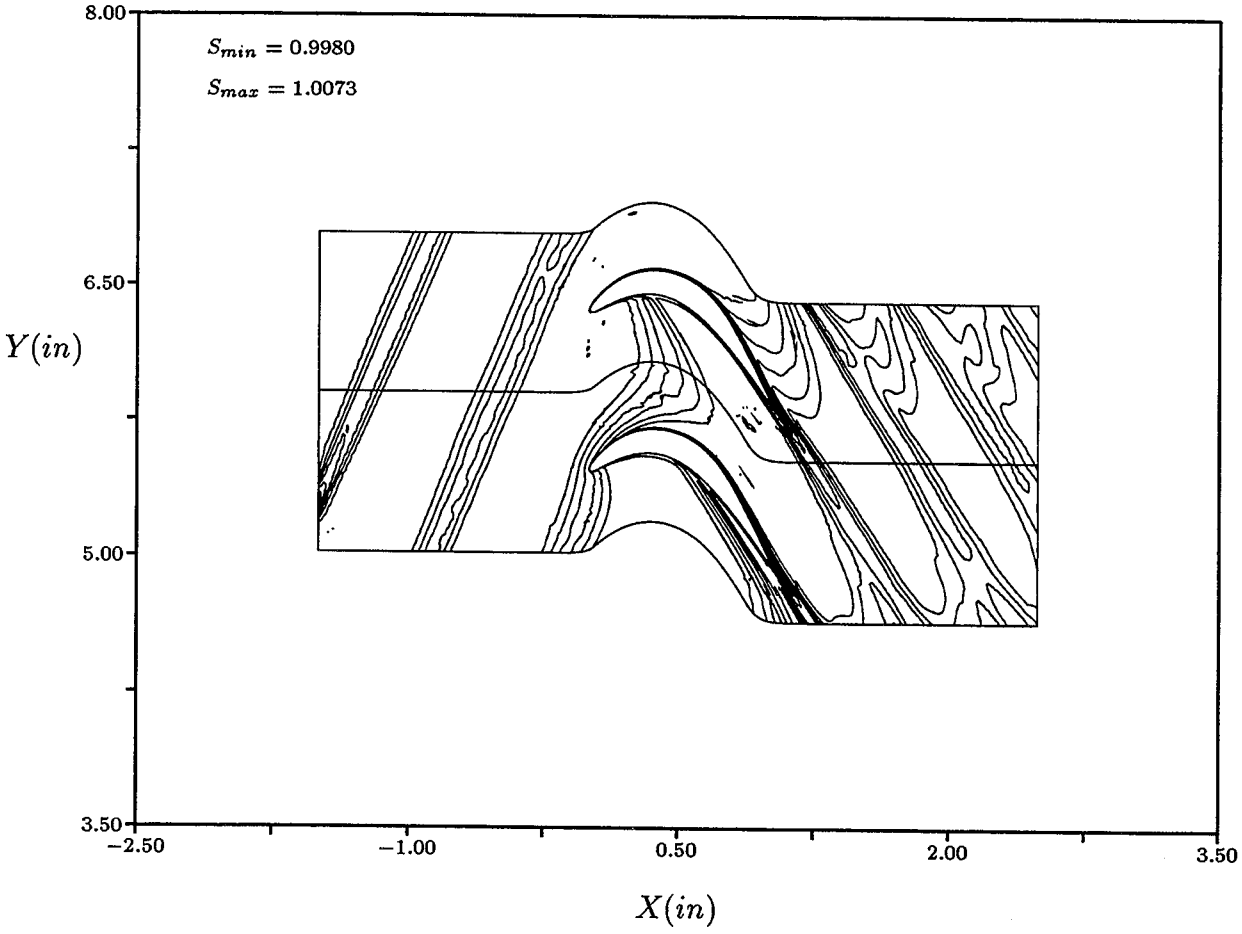

Figure 45: Instantaneous entropy contours for the PAK B turbine blade - $Re = 120,000$, LSRR stator wake, floating transition

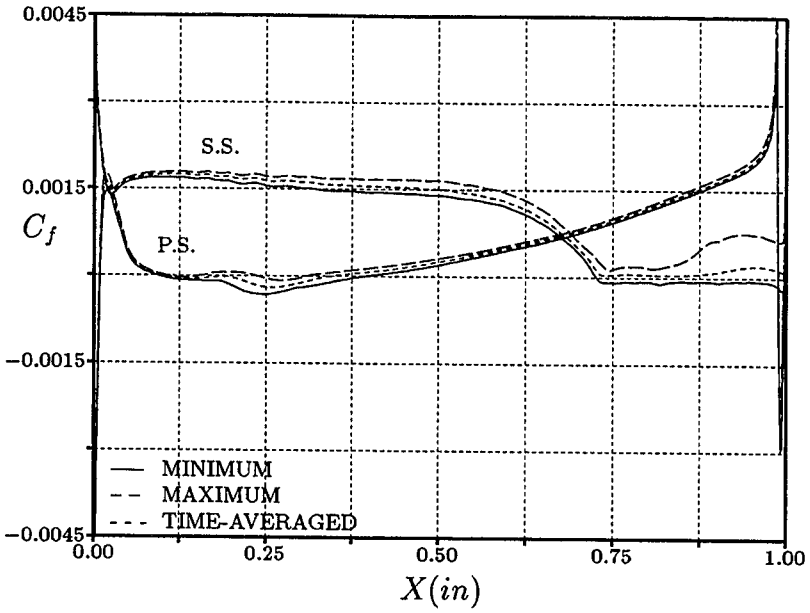

Figure 46: Unsteady skin friction envelope for the PAK B turbine blade - $Re = 120,000$, LSRR stator wake, fixed transition

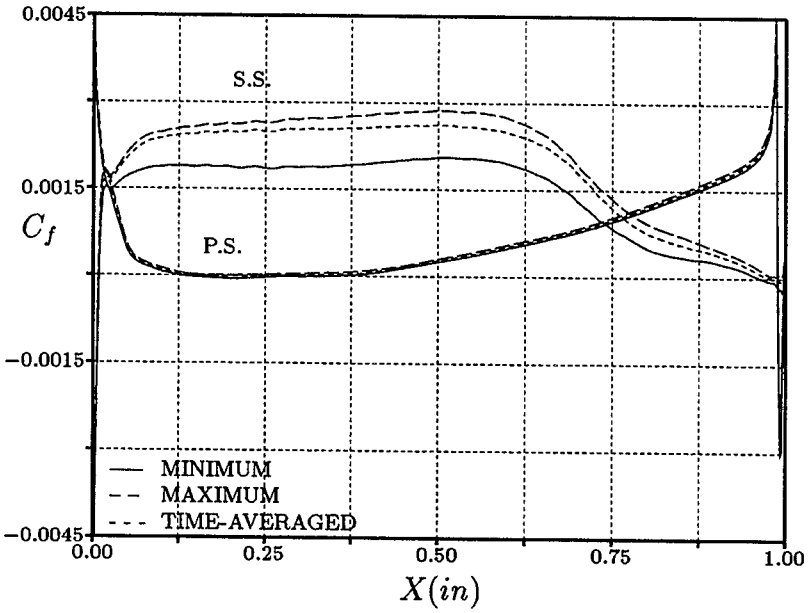

Figure 47: Unsteady skin friction envelope for the PAK B turbine blade - $Re = 120,000$, LSRR stator wake, floating transition

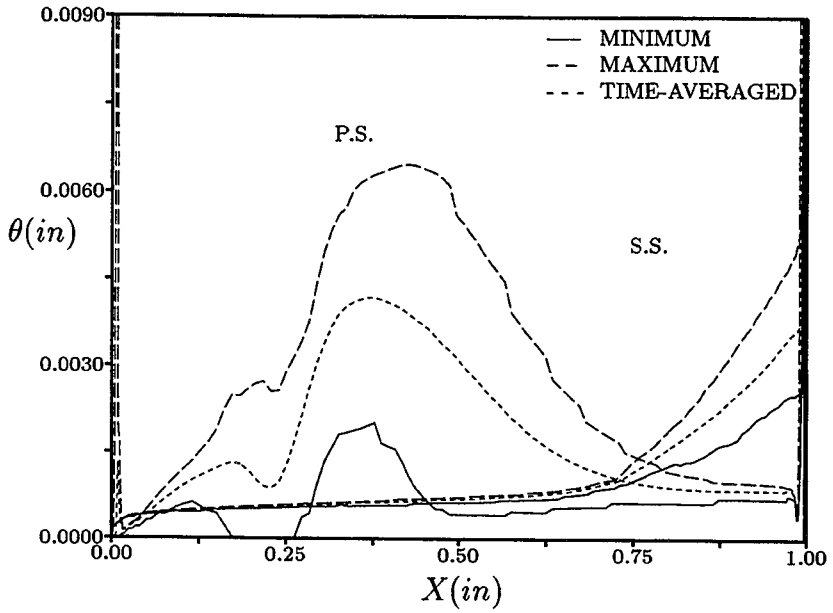

Figure 48: Unsteady momentum thickness envelope for the PAK B turbine blade - $Re = 120,000$, LSRR stator wake, fixed transition

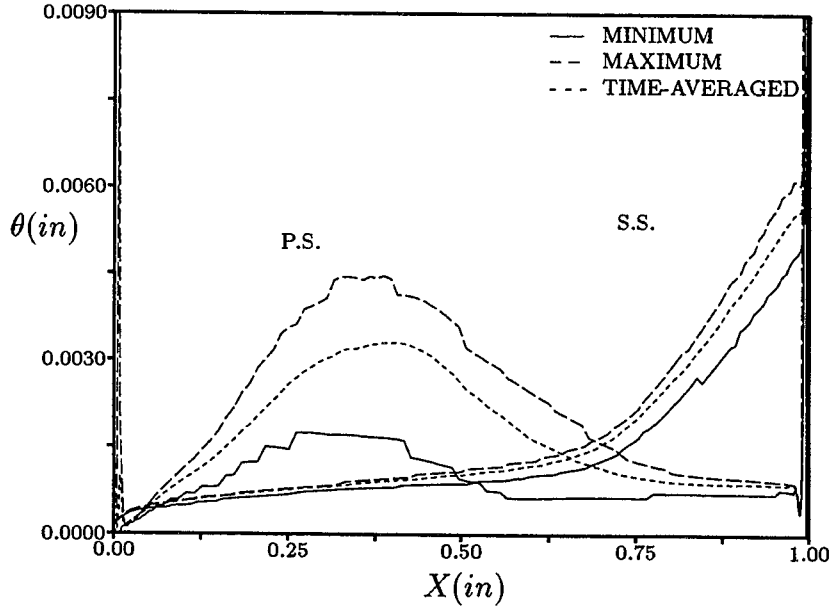

Figure 49: Unsteady momentum thickness envelope for the PAK B turbine blade - $Re = 120,000$, LSRR stator wake, floating transition

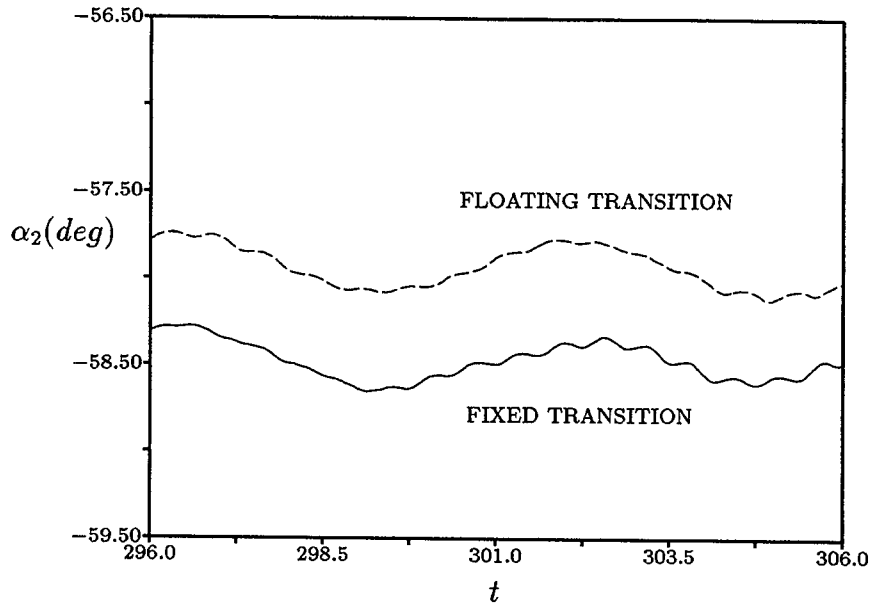

Figure 50: Exit flow angle variation for the PAK B turbine blade - $Re = 120,000$, LSRR stator wake

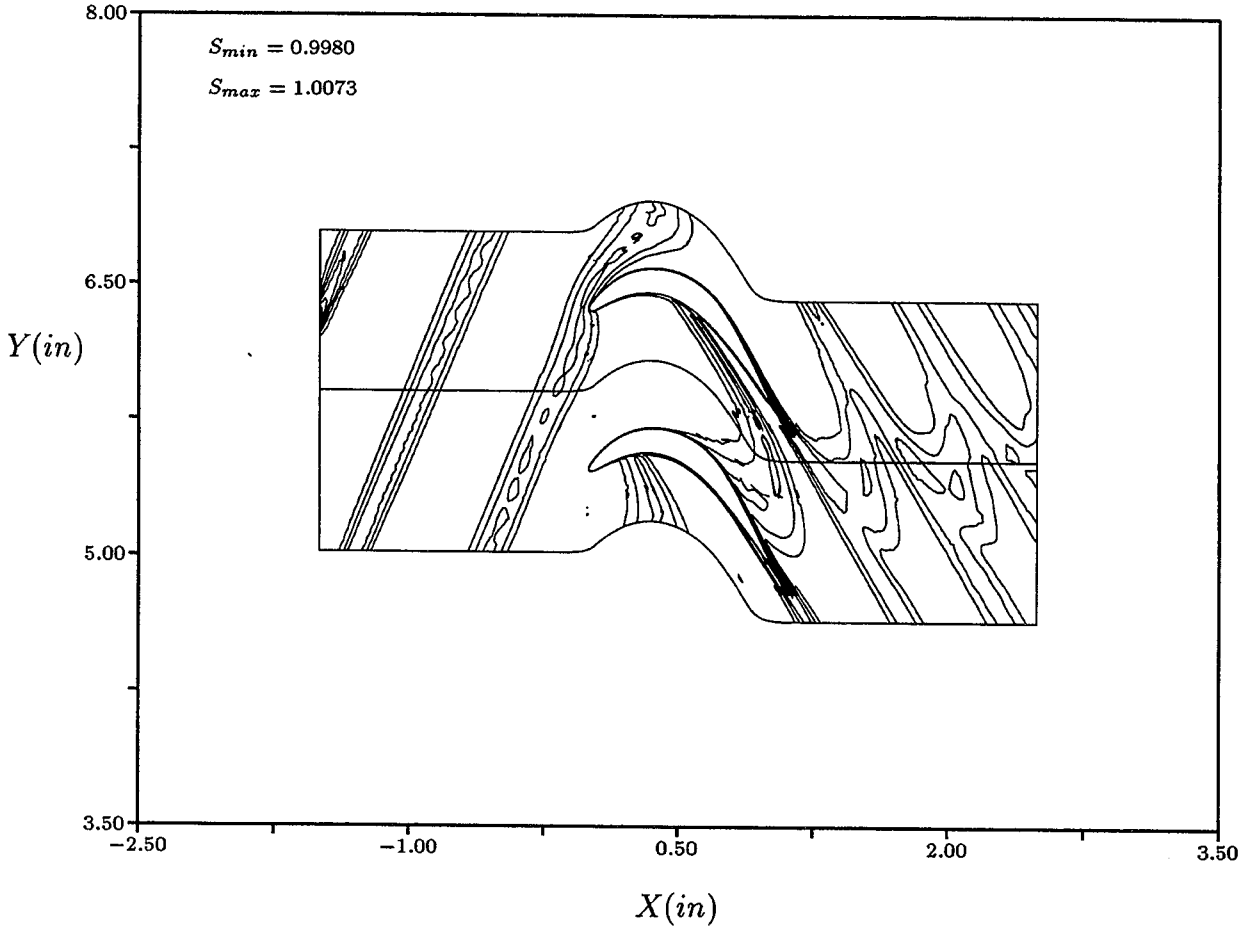

Figure 51: Instantaneous entropy contours for the PAK B turbine blade - $Re = 200,000$, LSRR stator wake, fixed transition

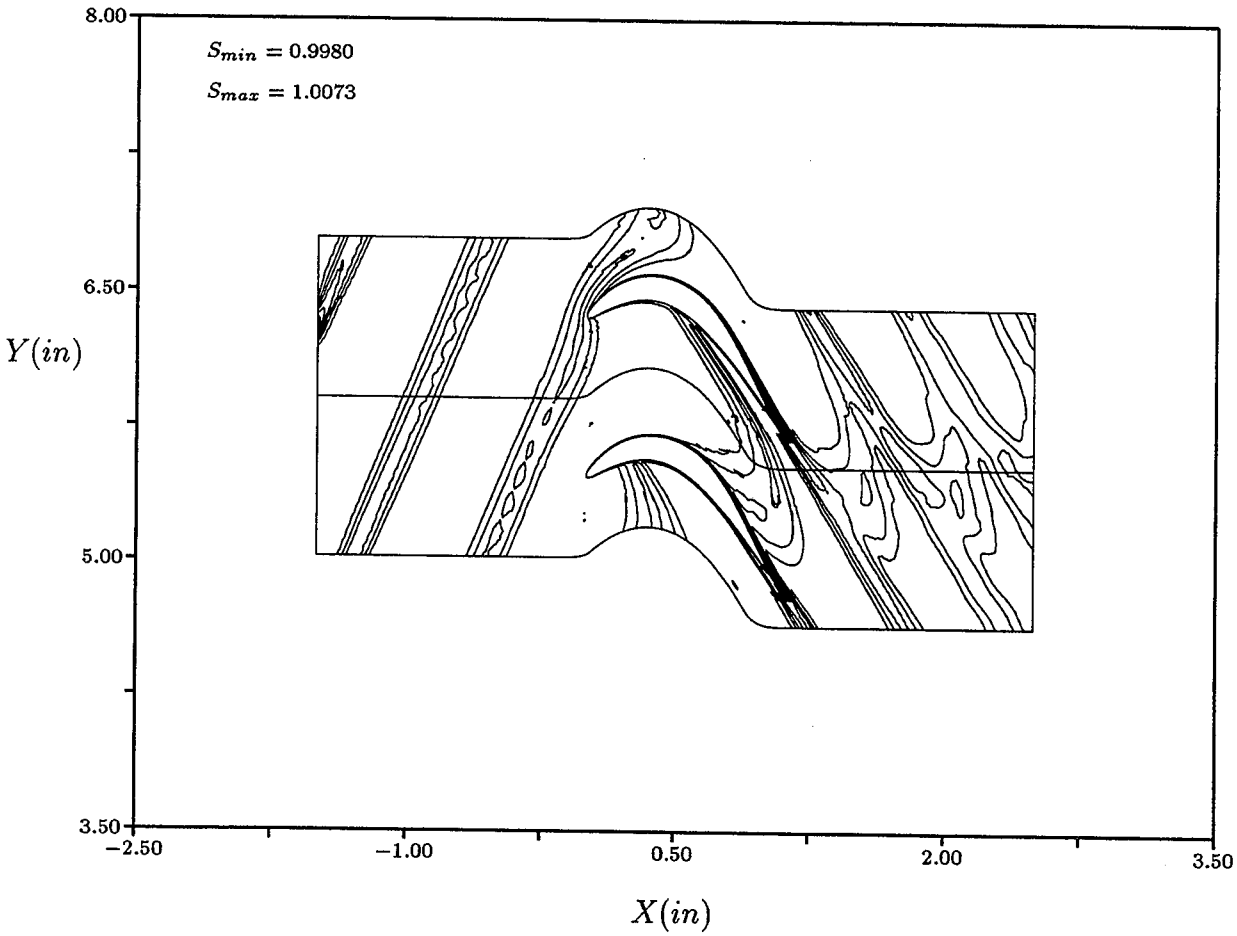

Figure 52: Instantaneous entropy contours for the PAK B turbine blade - $Re = 200,000$, LSRR stator wake, floating transition

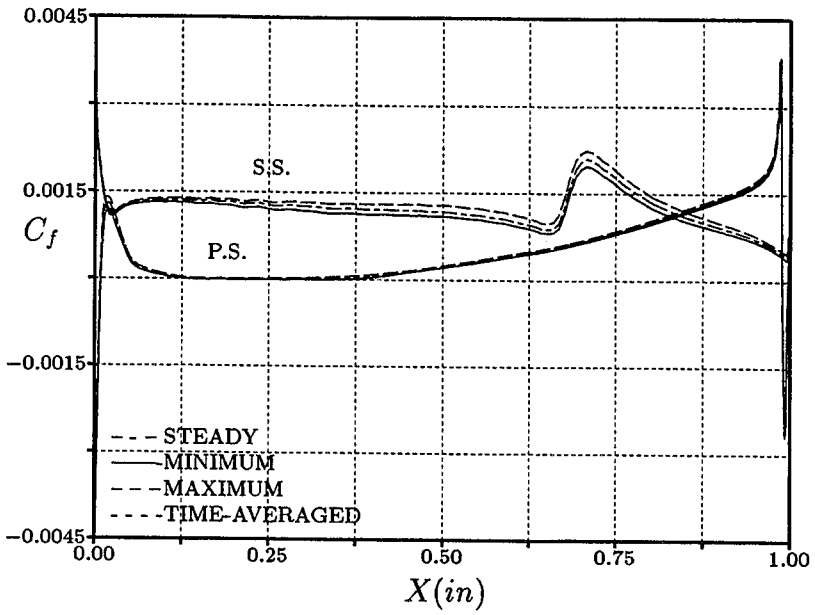

Figure 53: Unsteady skin friction envelope for the PAK B turbine blade - $Re = 200,000$, LSRR stator wake, fixed transition

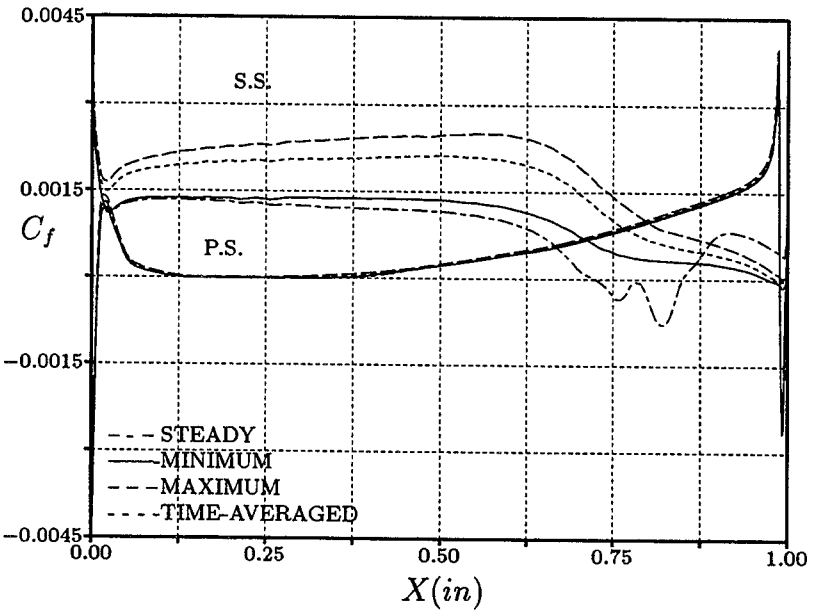

Figure 54: Unsteady skin friction envelope for the PAK B turbine blade - $Re = 200,000$, LSRR stator wake, floating transition

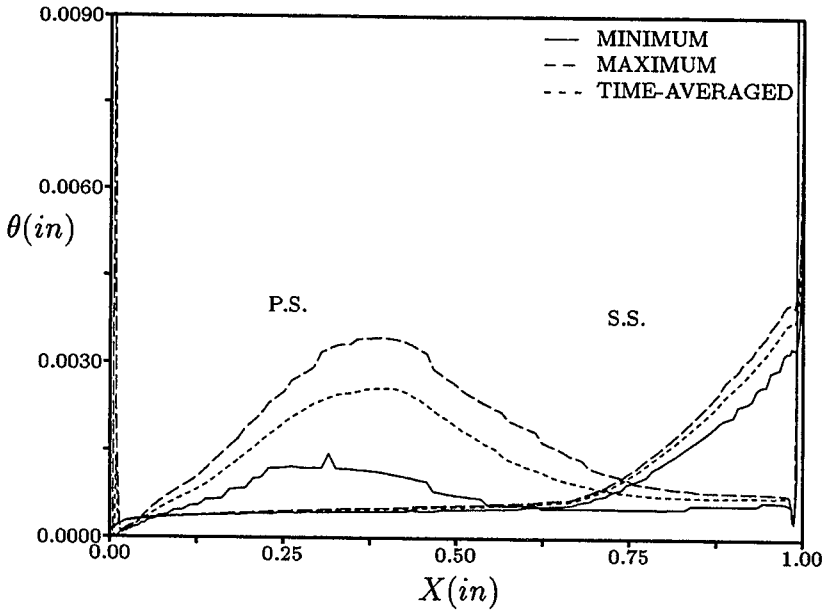

Figure 55: Unsteady momentum thickness envelope for the PAK B turbine blade - Re = 200,000, LSRR stator wake, fixed transition

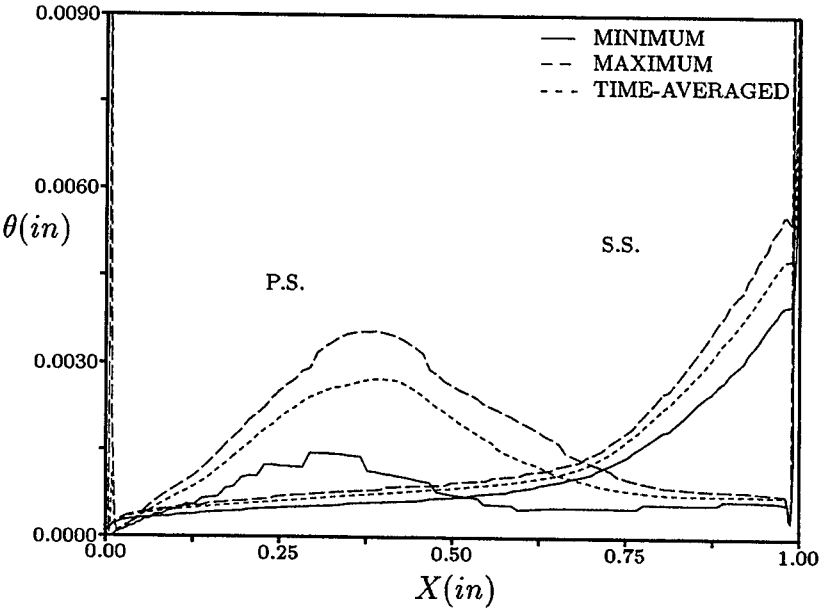

Figure 56: Unsteady momentum thickness envelope for the PAK B turbine blade - Re = 200,000, LSRR stator wake, floating transition

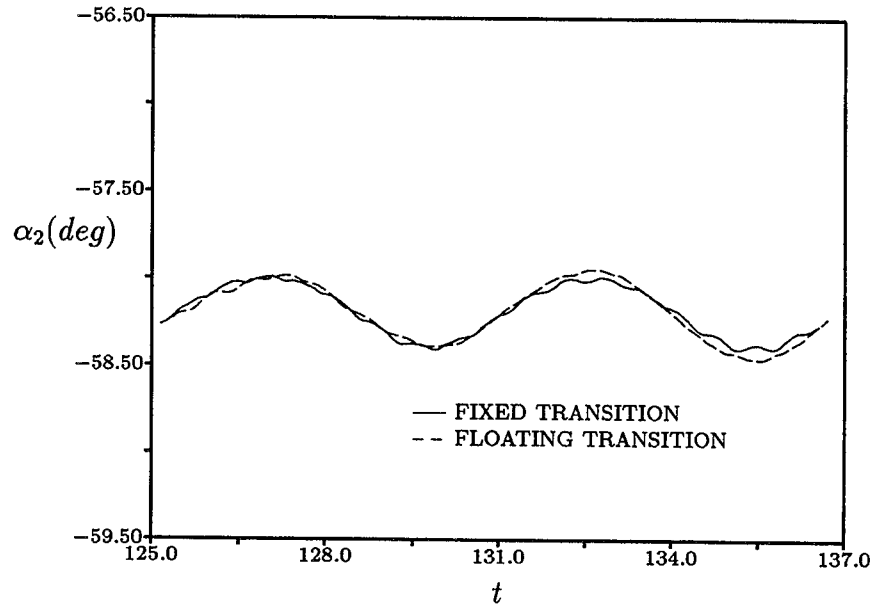

Figure 57: Exit flow angle variation for the PAK B turbine blade - $Re = 200,000$, LSRR stator wake

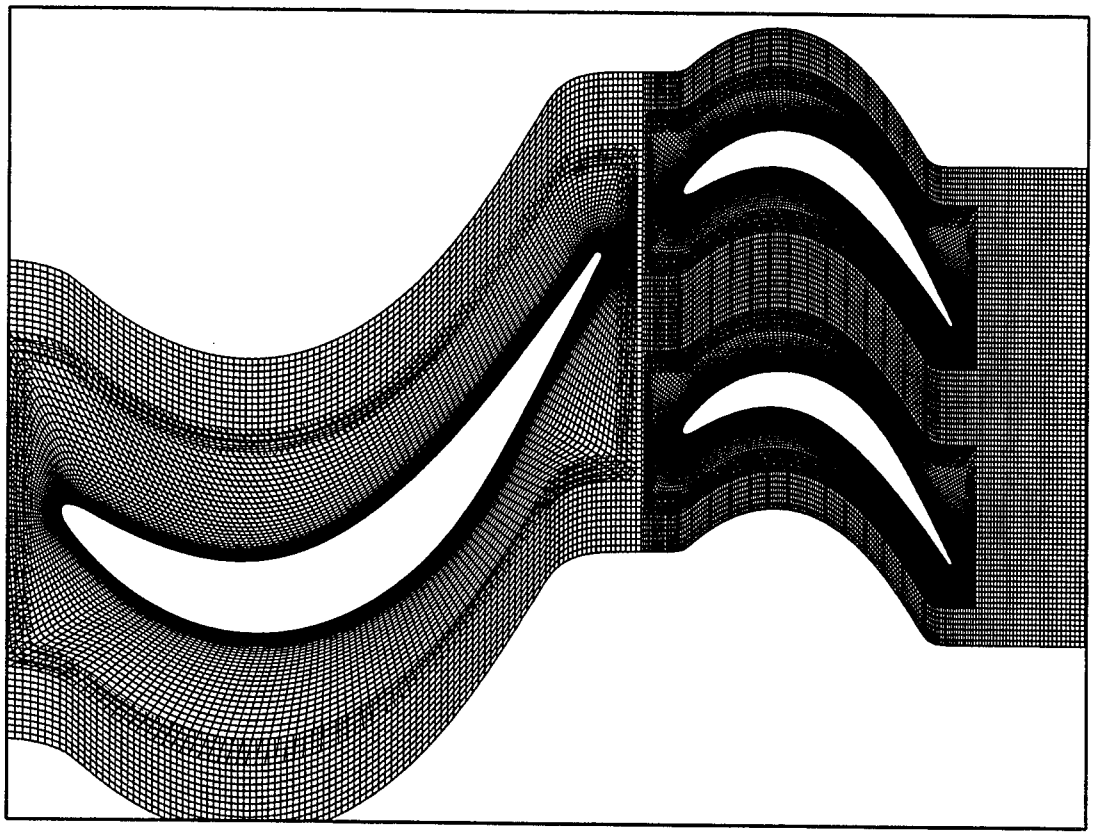

Figure 58: Computational grid for the PAK B turbine stage

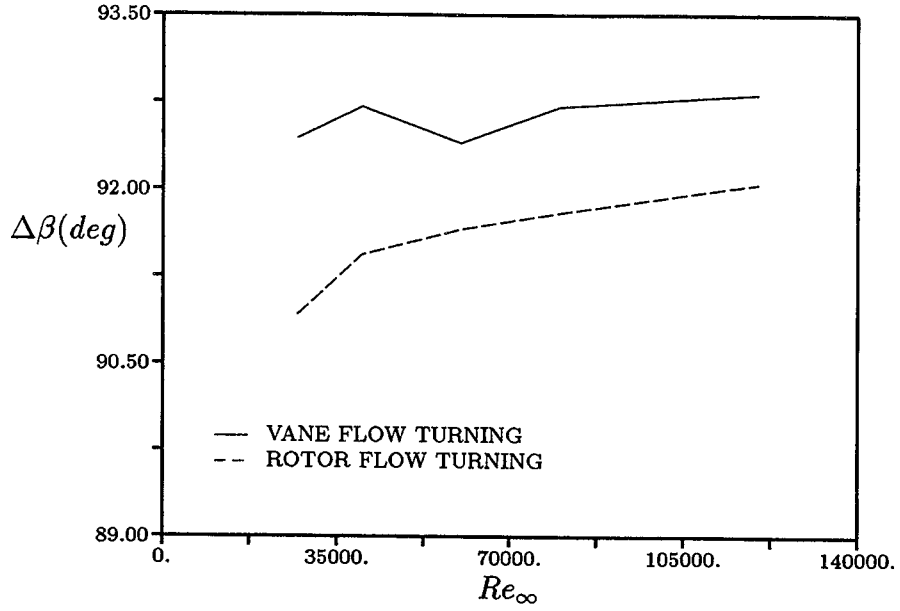

Figure 59: Flow turning angles; Baldwin-Lomax - turbulent

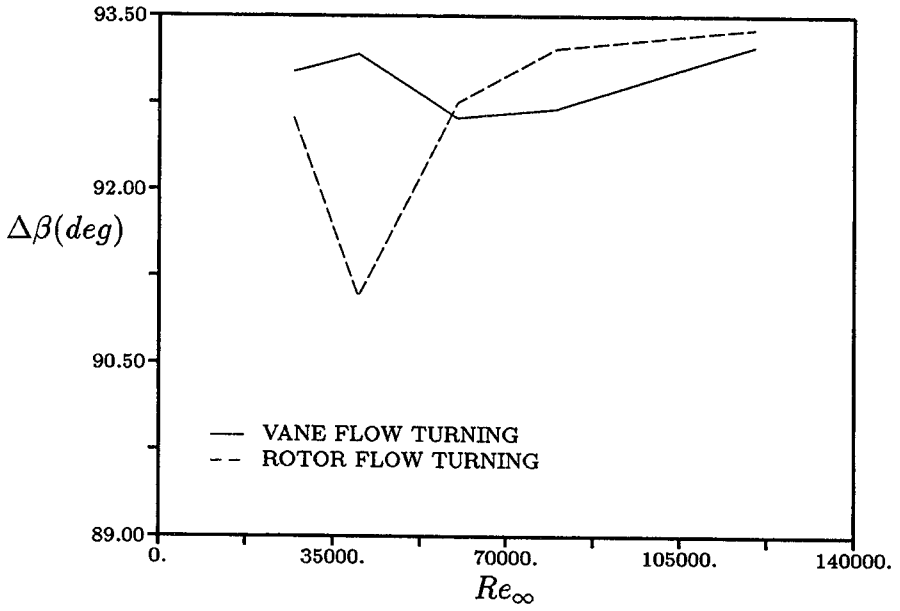

Figure 60: Flow turning angles; Baldwin-Lomax - floating transition

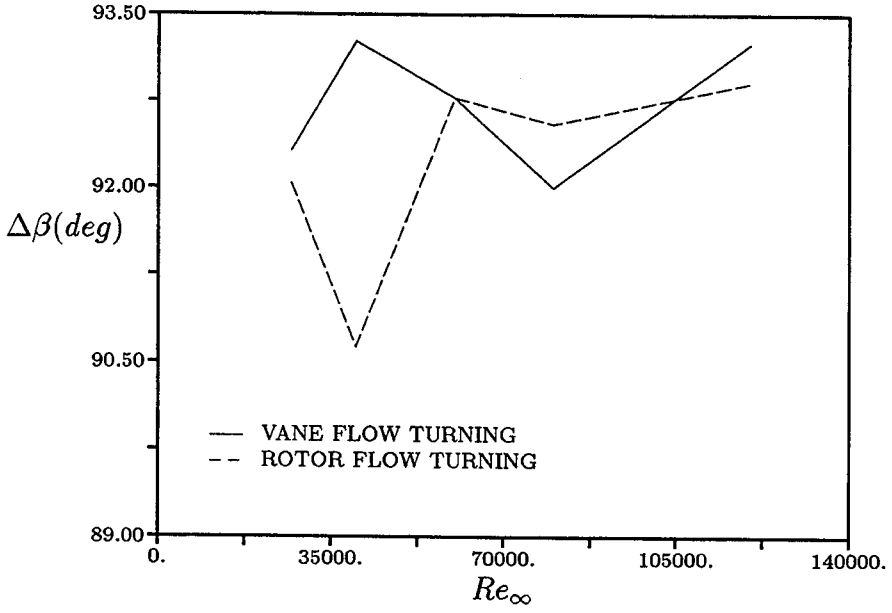

Figure 61: Flow turning angles; Baldwin-Lomax - fixed transition

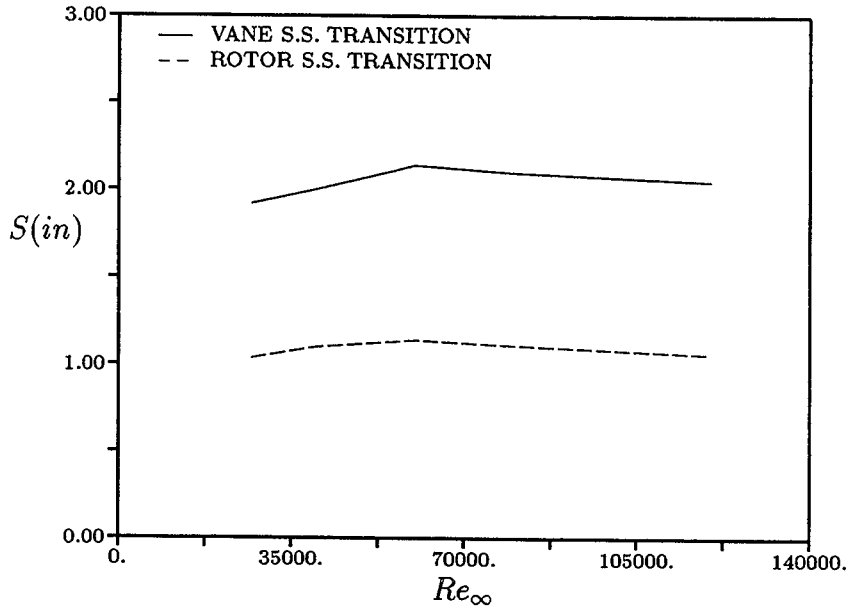

Figure 62: Suction surface transition locations

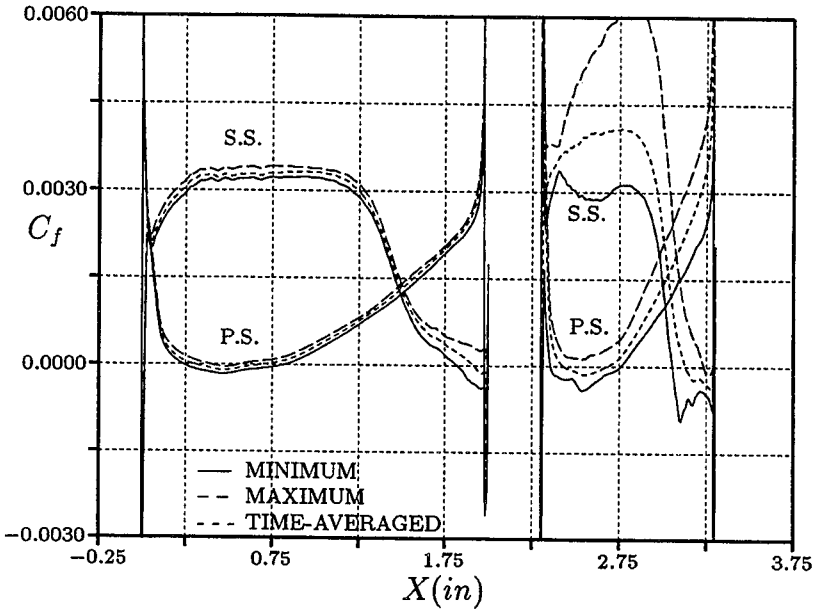

Figure 63: Skin friction envelope for the PAK B turbine stage - $Re = 27,000$; B-L, turbulent

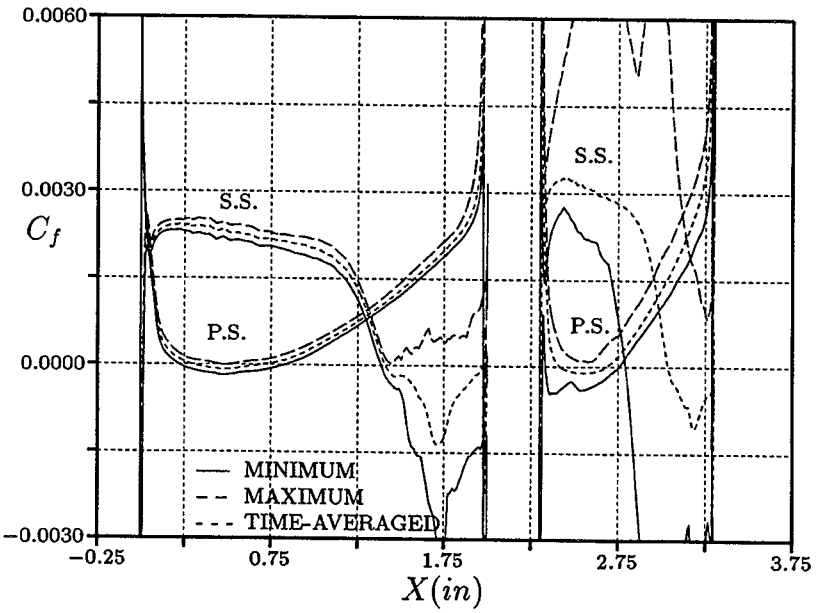

Figure 64: Skin friction envelope for the PAK B turbine stage - $Re = 27,000$; B-L, floating transition

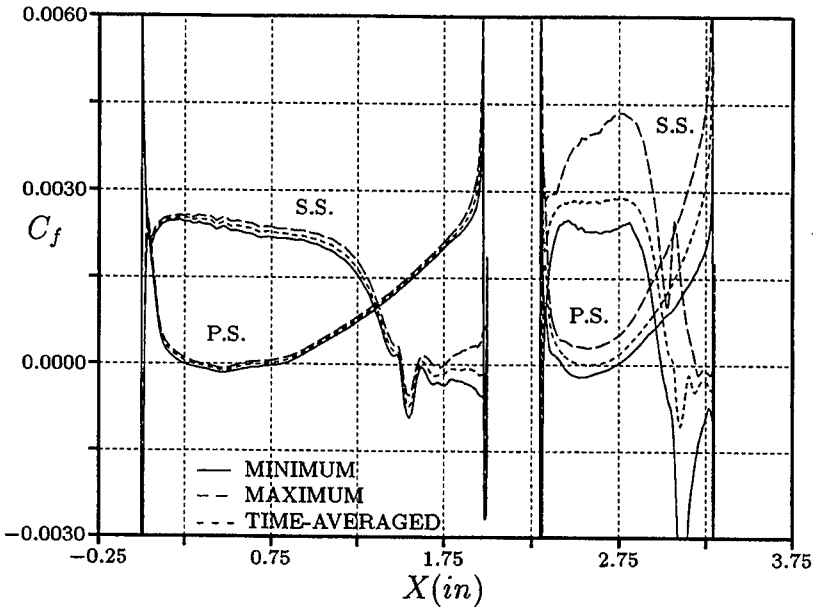

Figure 65: Skin friction envelope for the PAK B turbine stage - $Re = 27,000$; B-L, fixed transition

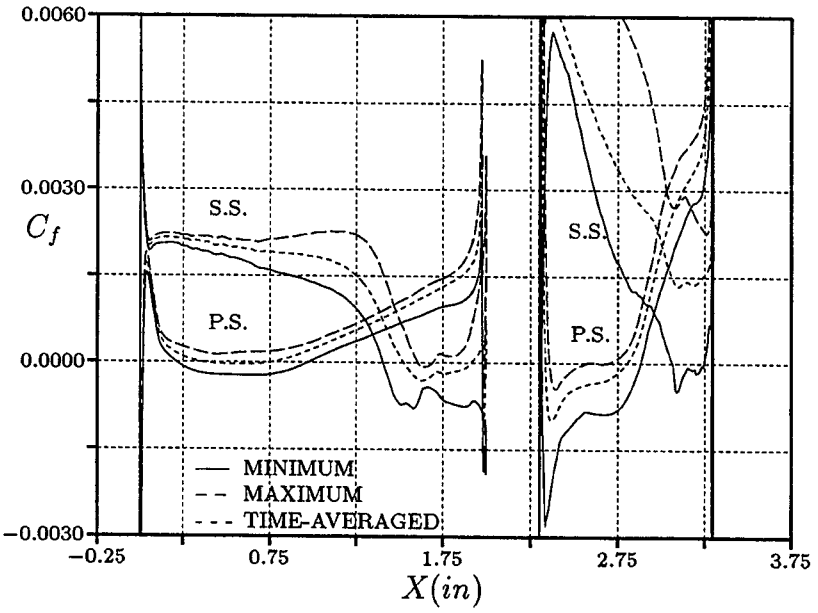

Figure 66: Skin friction envelope for the PAK B turbine stage - $Re = 27,000$; $k - \epsilon$ model

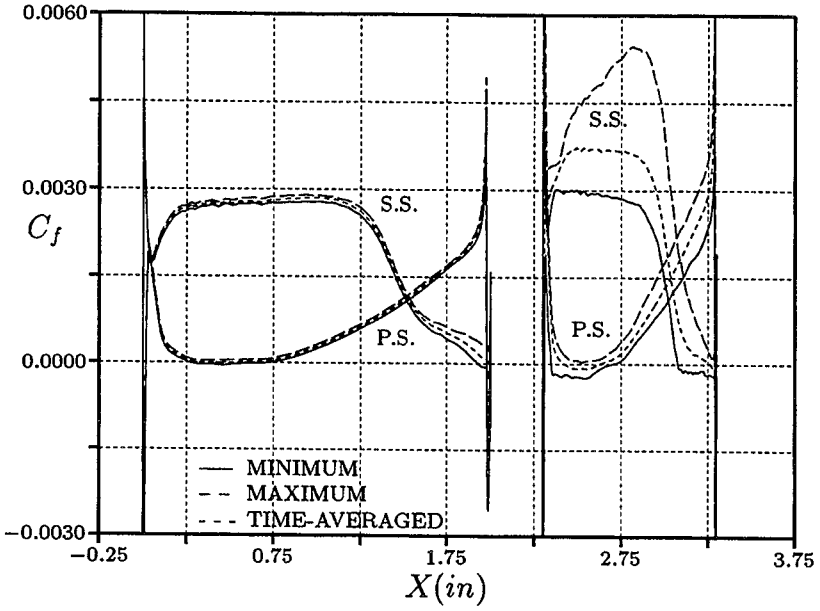

Figure 67: Skin friction envelope for the PAK B turbine stage - $Re = 40,000$; B-L, turbulent

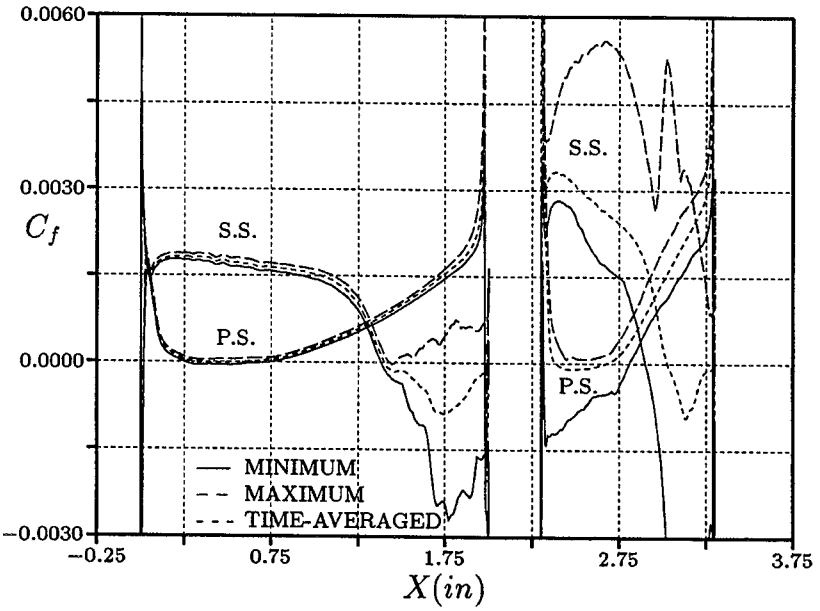

Figure 68: Skin friction envelope for the PAK B turbine stage - $Re = 40,000$; B-L, floating transition

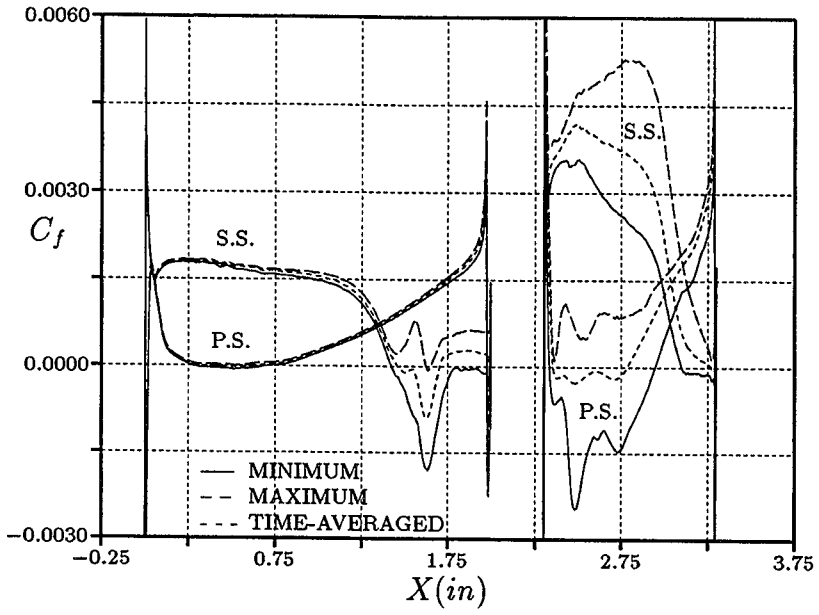

Figure 69: Skin friction envelope for the PAK B turbine stage - $Re = 40,000$; B-L, fixed transition

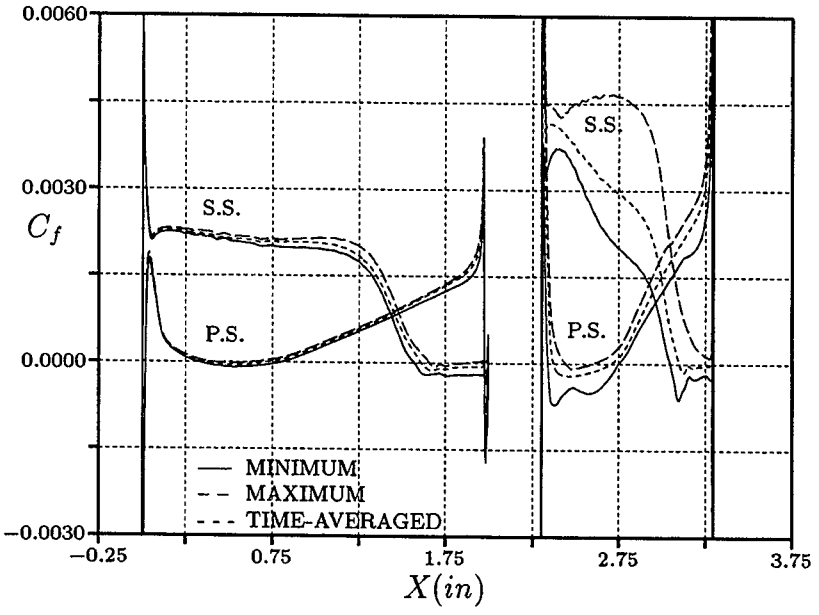

Figure 70: Skin friction envelope for the PAK B turbine stage - $Re = 40,000$; $k - \epsilon$ model

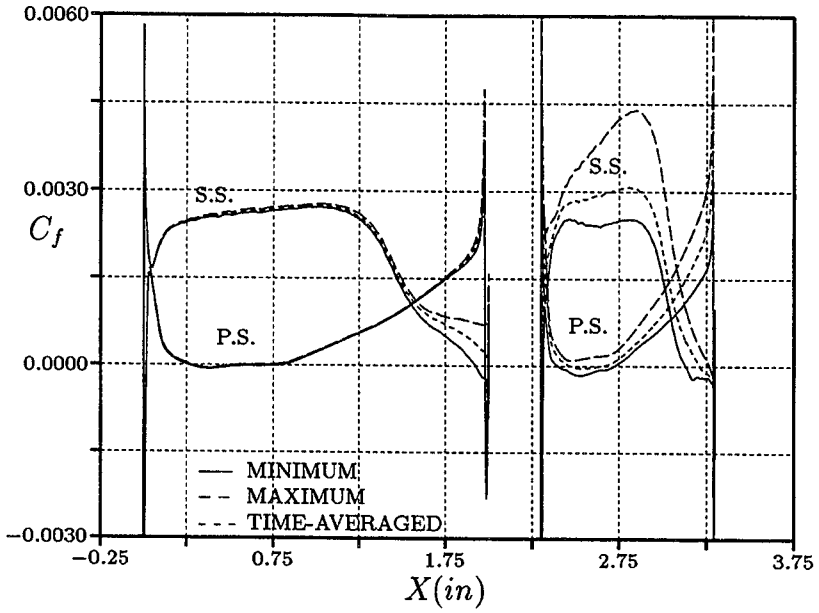

Figure 71: Skin friction envelope for the PAK B turbine stage - $Re = 60,000$; B-L, turbulent

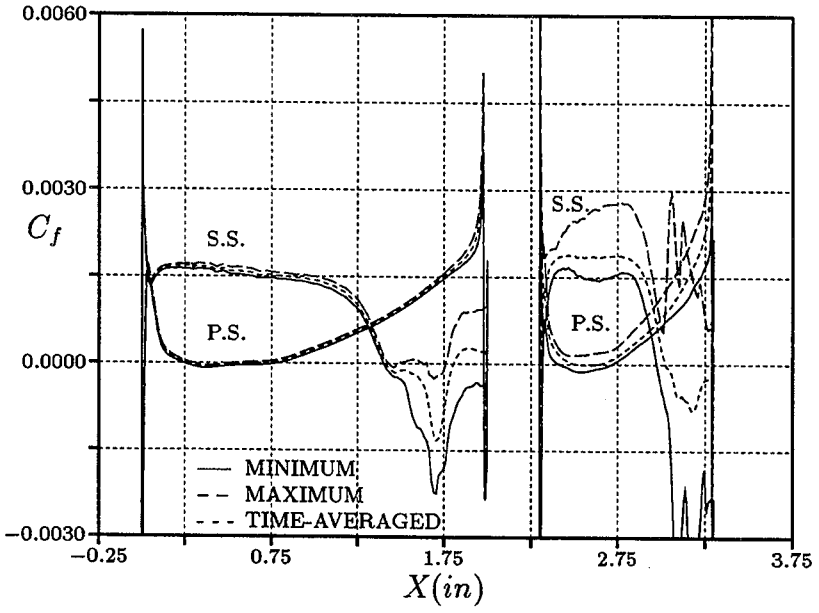

Figure 72: Skin friction envelope for the PAK B turbine stage - $Re = 60,000$; B-L, floating transition

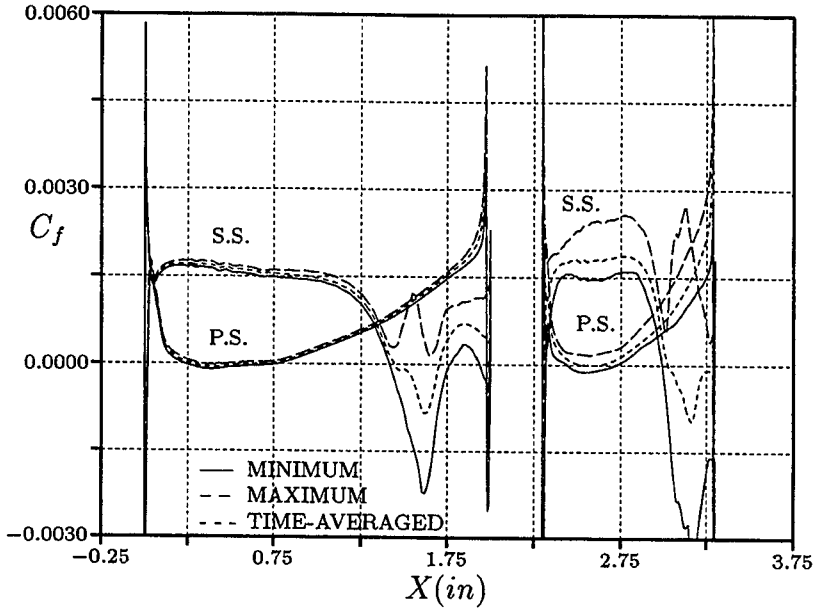

Figure 73: Skin friction envelope for the PAK B turbine stage - $Re = 60,000$; B-L, fixed transition

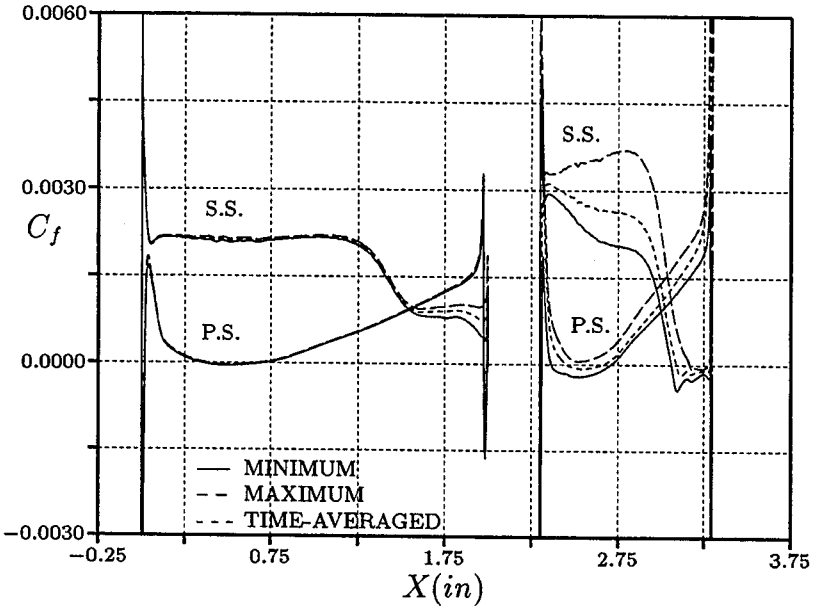

Figure 74: Skin friction envelope for the PAK B turbine stage - $Re = 60,000$; $k - \epsilon$ model

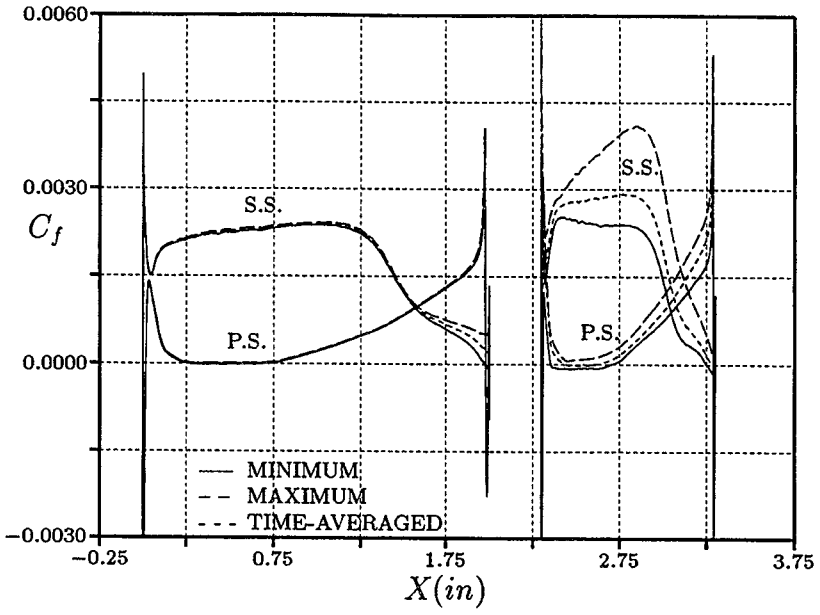

Figure 75: Skin friction envelope for the PAK B turbine stage - $Re = 80,000$; B-L, turbulent

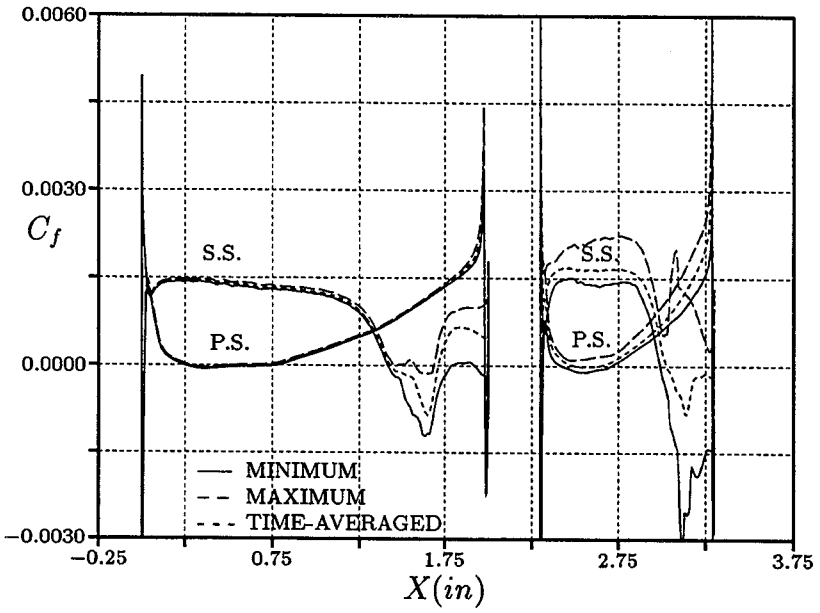

Figure 76: Skin friction envelope for the PAK B turbine stage - $Re = 80,000$; B-L, floating transition

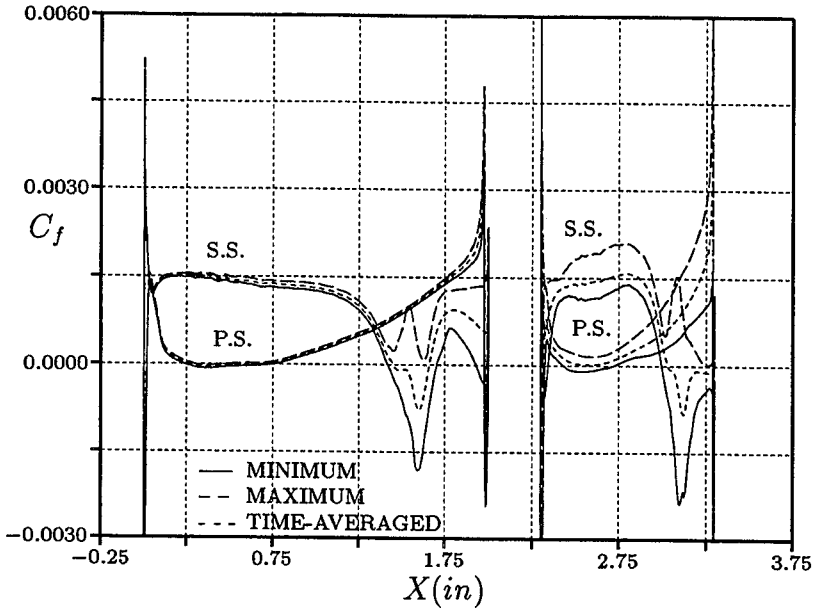

Figure 77: Skin friction envelope for the PAK B turbine stage - $Re = 80,000$; B-L, fixed transition

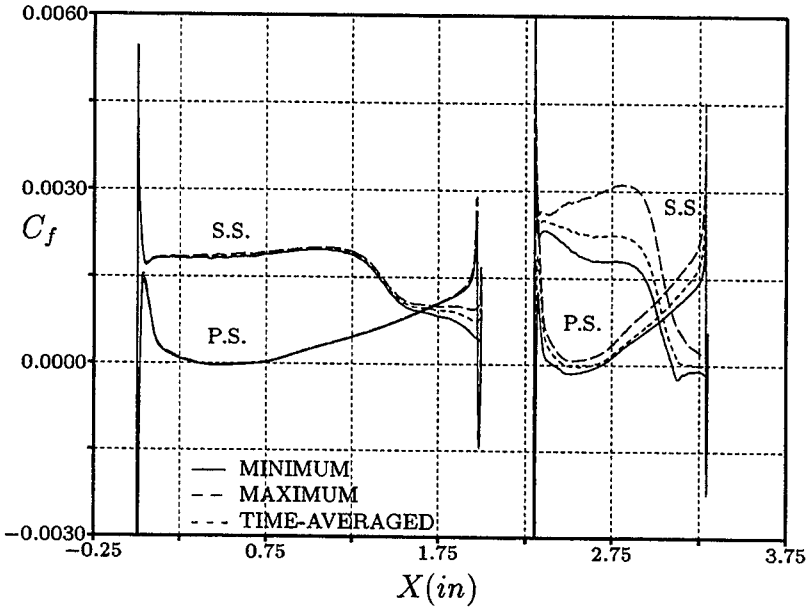

Figure 78: Skin friction envelope for the PAK B turbine stage - $Re = 80,000$; $k - \epsilon$ model

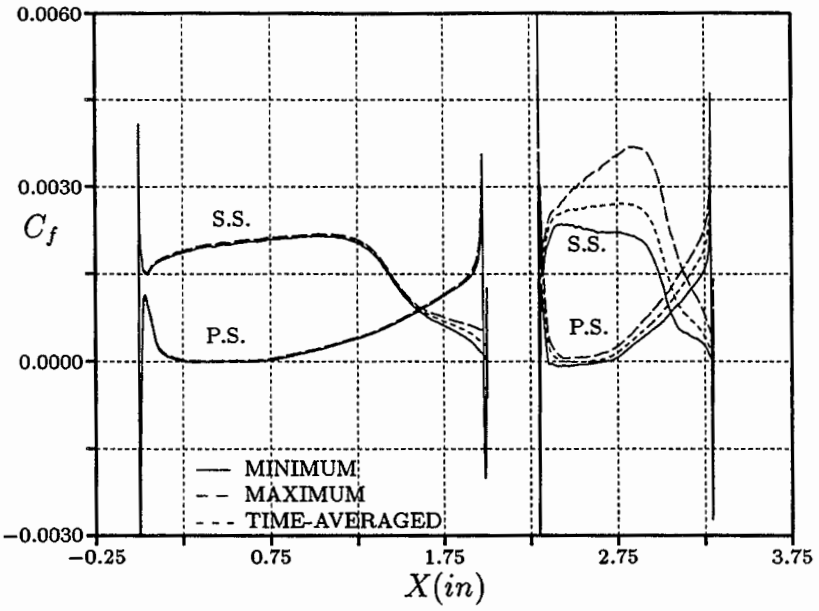

Figure 79: Skin friction envelope for the PAK B turbine stage - $Re = 120,000$; B-L, turbulent

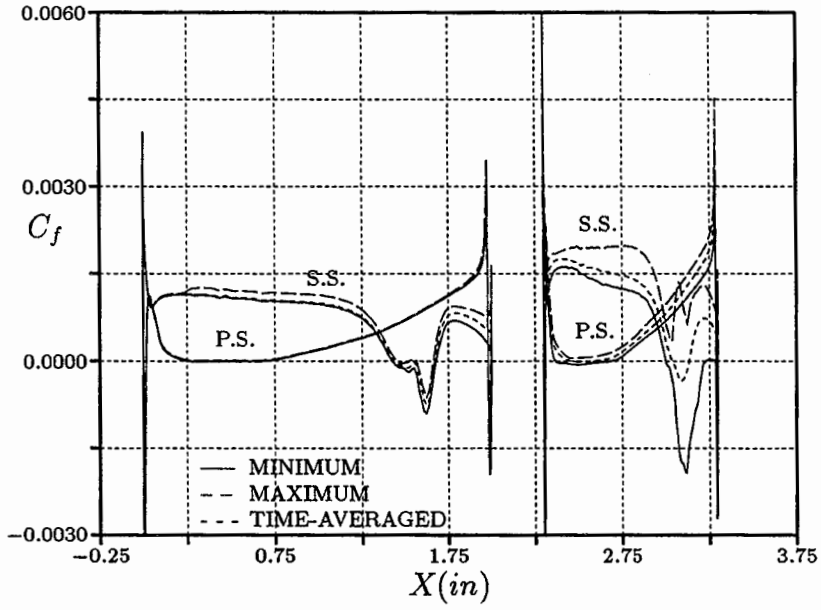

Figure 80: Skin friction envelope for the PAK B turbine stage - $Re = 120,000$; B-L, floating transition

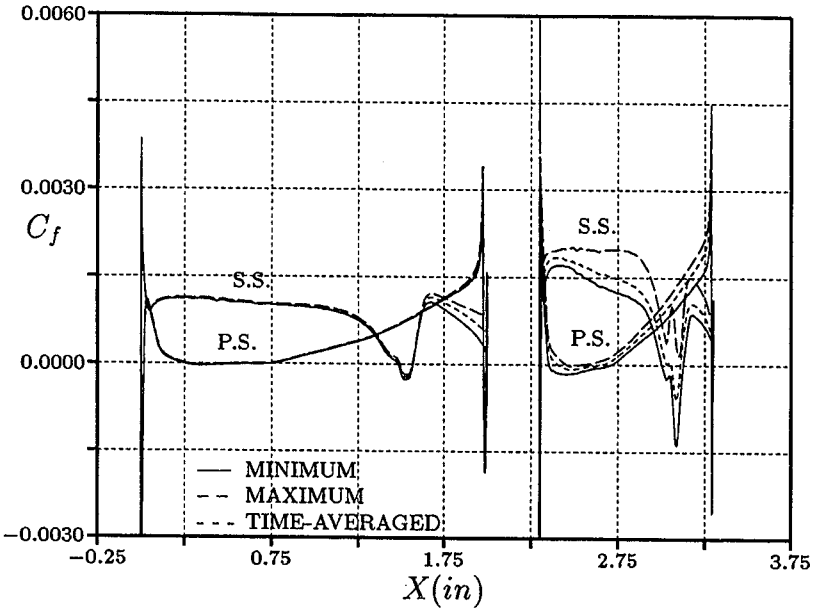

Figure 81: Skin friction envelope for the PAK B turbine stage - $Re = 120,000$; B-L, fixed transition

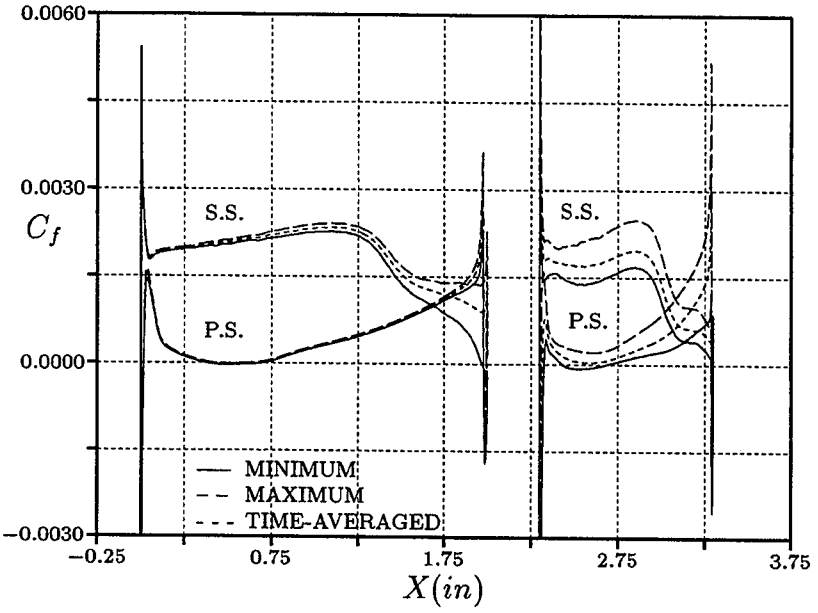

Figure 82: Skin friction envelope for the PAK B turbine stage - $Re = 120,000$; $k - \epsilon$ model

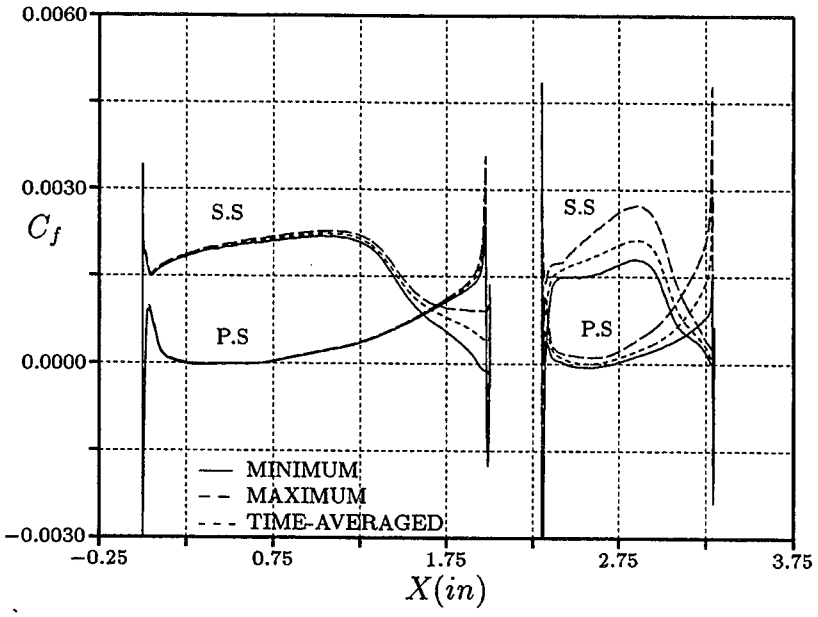

Figure 83: Skin friction envelope for the PAK B turbine stage - $Re = 200,000$; B-L, turbulent

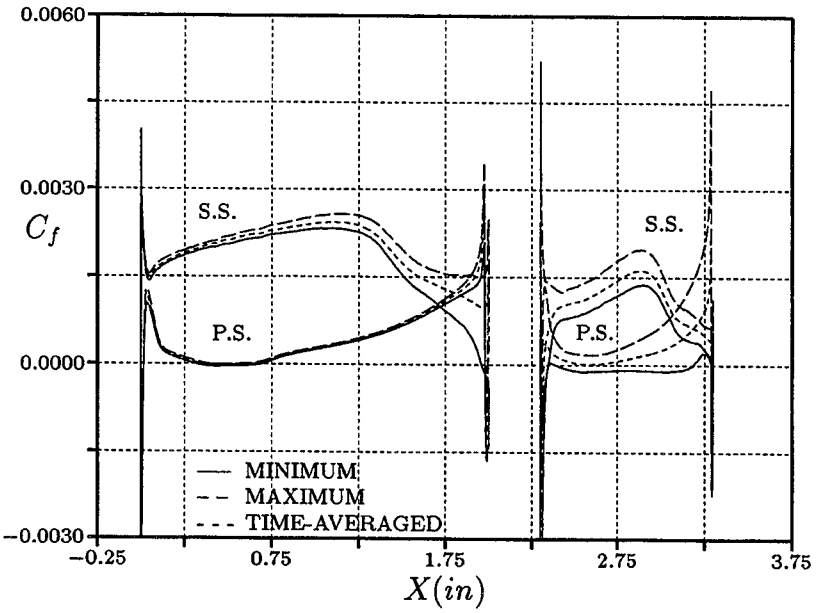

Figure 84: Skin friction envelope for the PAK B turbine stage - $Re = 200,000$; $k - \epsilon$ model

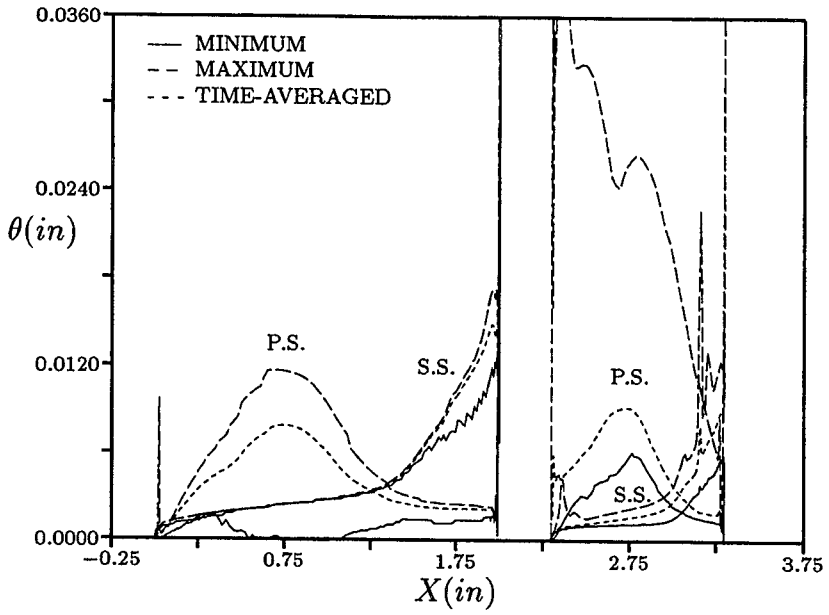

Figure 85: Momentum thickness envelope for the PAK B turbine stage - $Re = 27,000$; B-L, turbulent

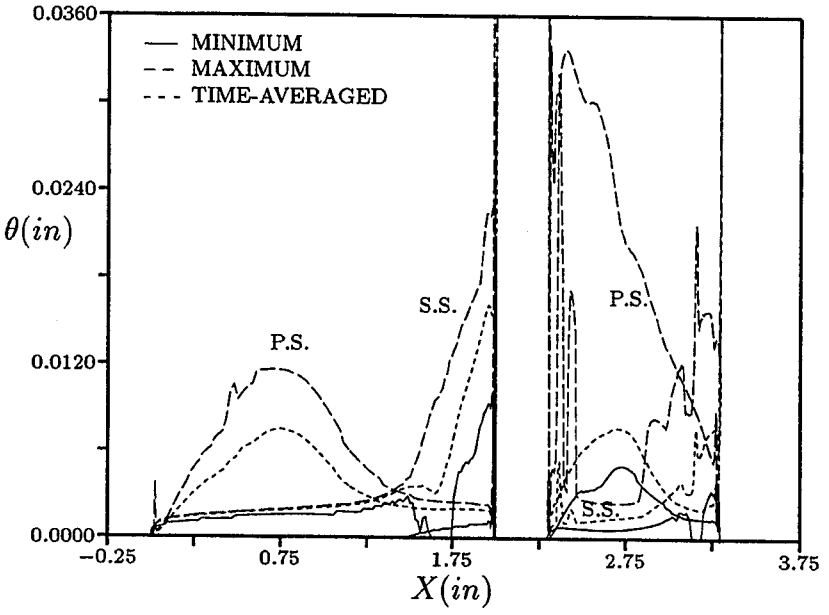

Figure 86: Momentum thickness envelope for the PAK B turbine stage - $Re = 27,000$; B-L, floating transition

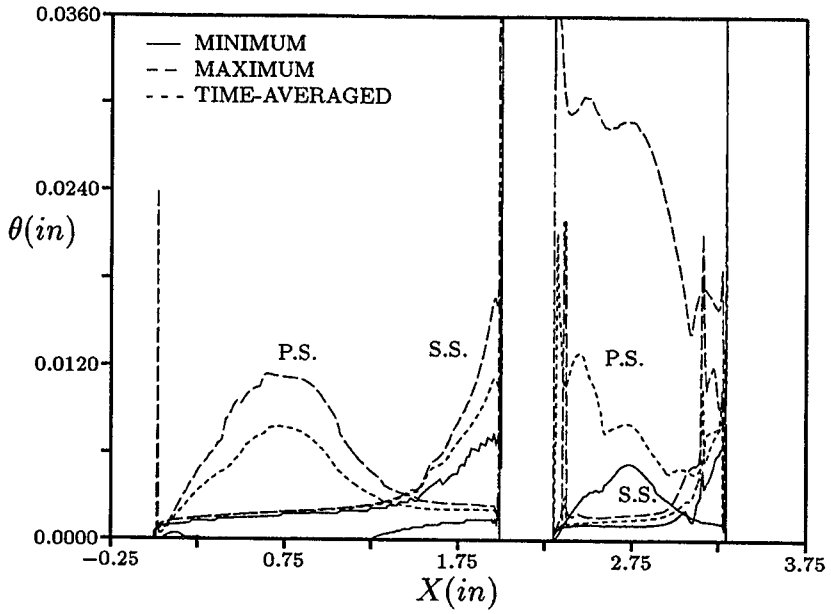

Figure 87: Momentum thickness envelope for the PAK B turbine stage - $Re = 27,000$; B-L, fixed transition

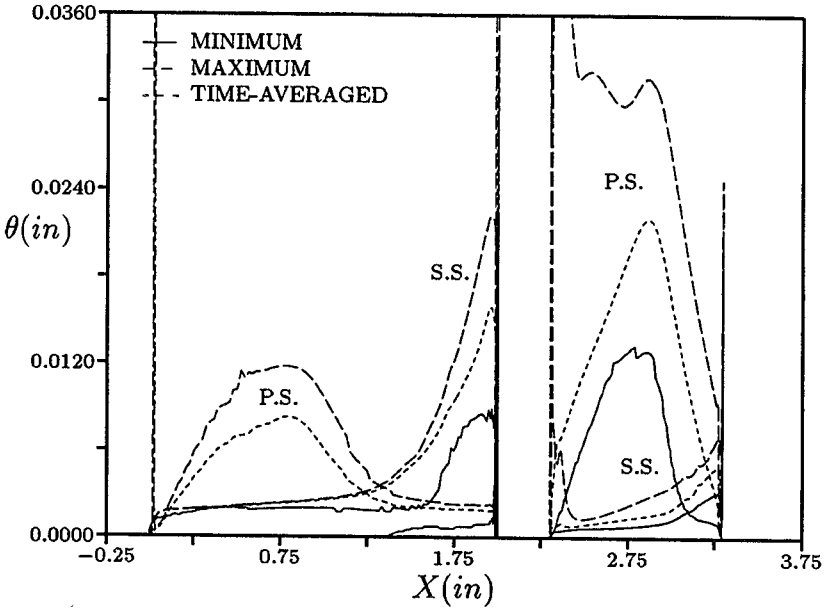

Figure 88: Momentum thickness envelope for the PAK B turbine stage - $Re = 27,000$; $k - \epsilon$ model

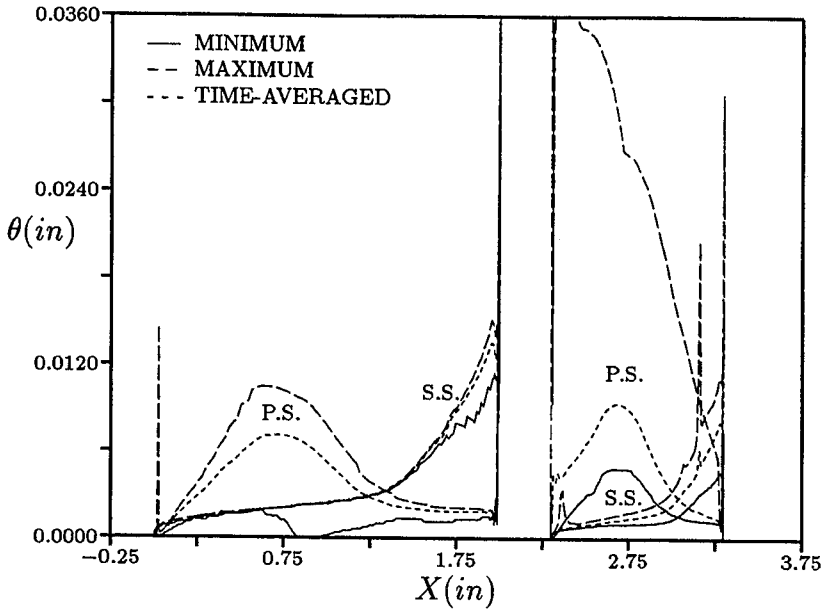

Figure 89: Momentum thickness envelope for the PAK B turbine stage - $Re = 40,000$; B-L, turbulent

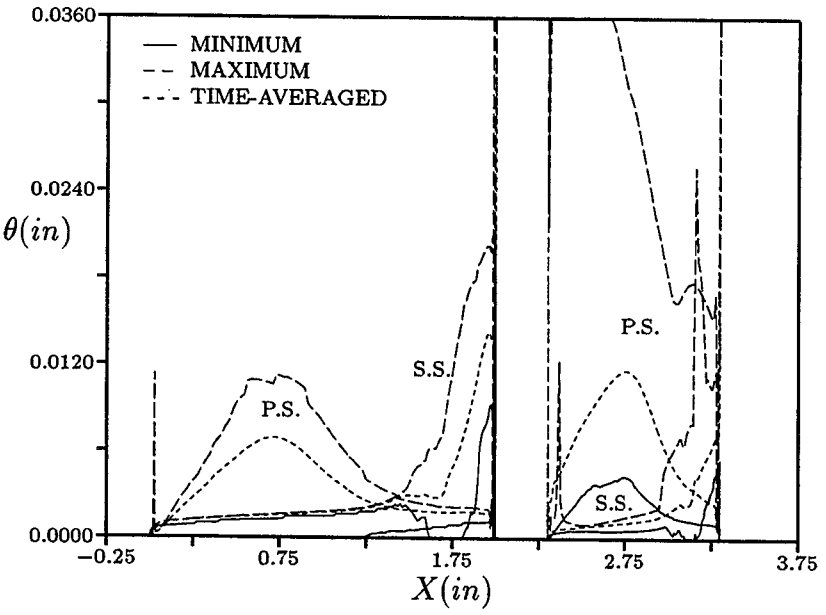

Figure 90: Momentum thickness envelope for the PAK B turbine stage - $Re = 40,000$; B-L, floating transition

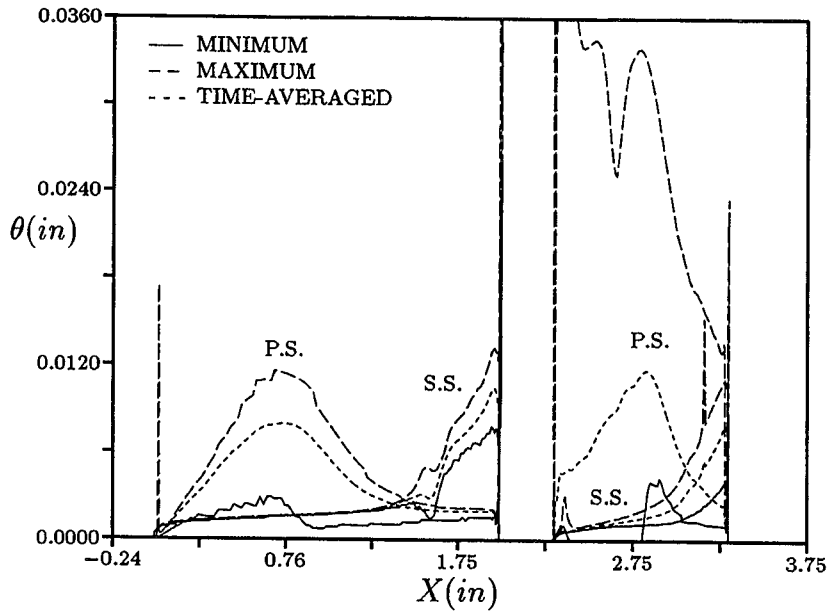

Figure 91: Momentum envelope for the PAK B turbine stage - $Re = 40,000$; B-L, fixed transition

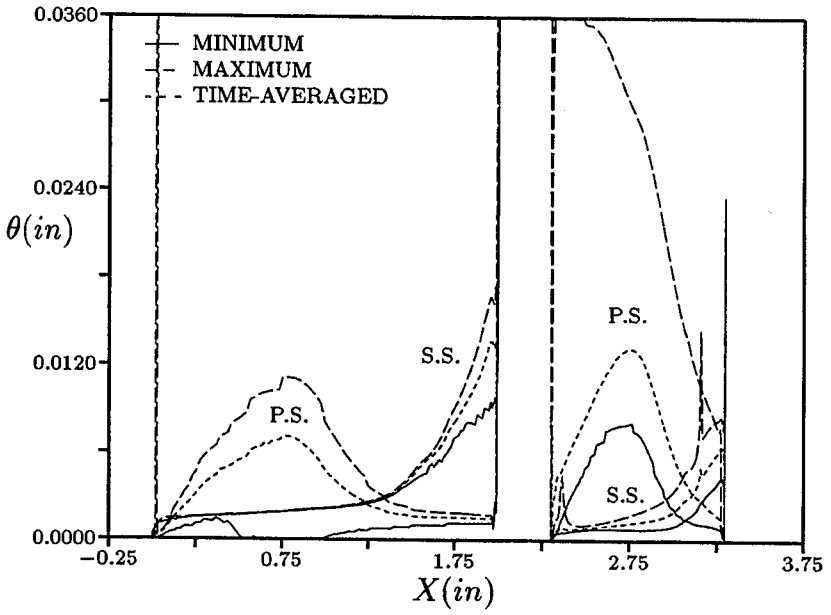

Figure 92: Momentum thickness envelope for the PAK B turbine stage - $Re = 40,000$; $k - \epsilon$ model

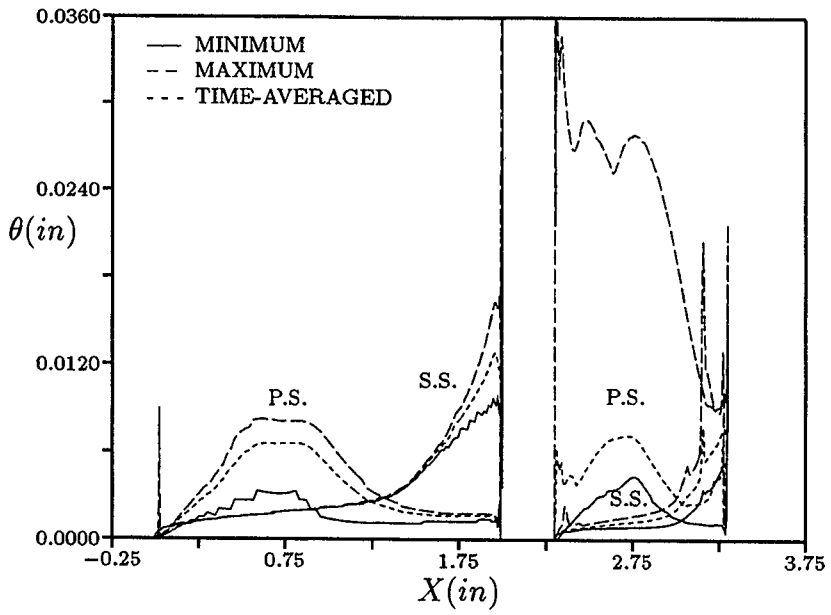

Figure 93: Momentum thickness envelope for the PAK B turbine stage - $Re = 60,000$; B-L, turbulent

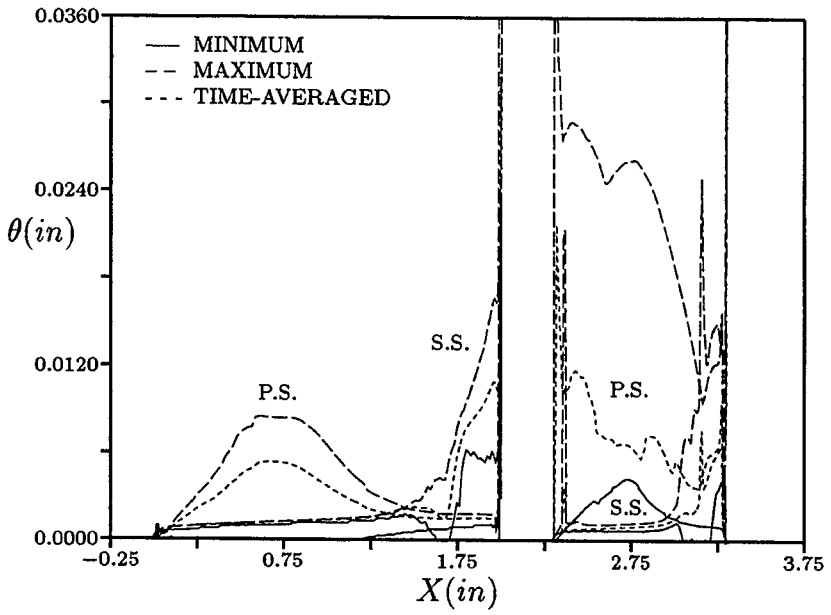

Figure 94: Momentum thickness envelope for the PAK B turbine stage - $Re = 60,000$; B-L, floating transition

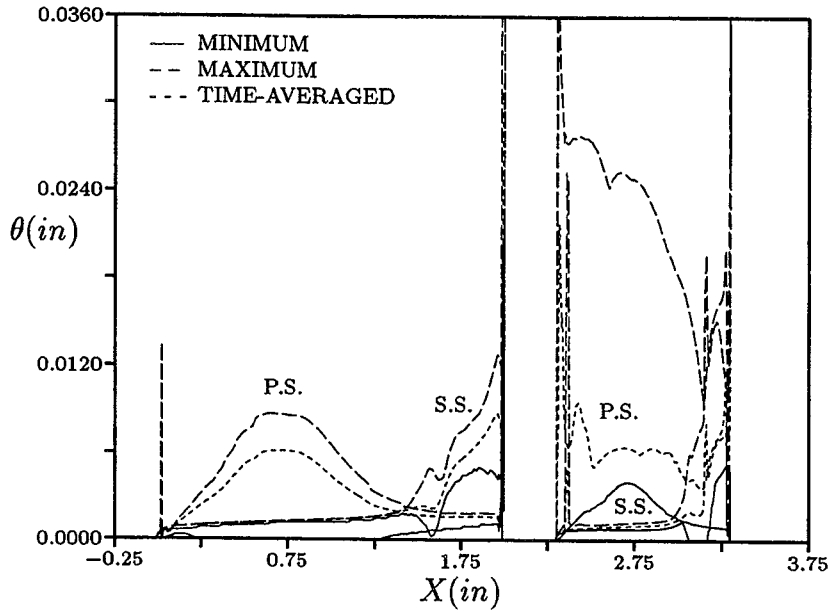

Figure 95: Momentum thickness envelope for the PAK B turbine stage - $Re = 60,000$; B-L, fixed transition

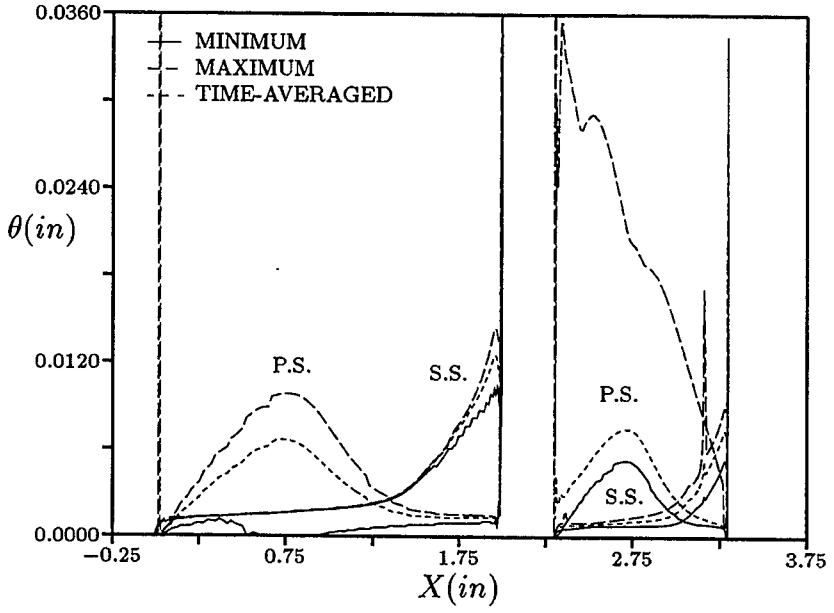

Figure 96: Momentum thickness envelope for the PAK B turbine stage - $Re = 60,000$; $k - \epsilon$ model

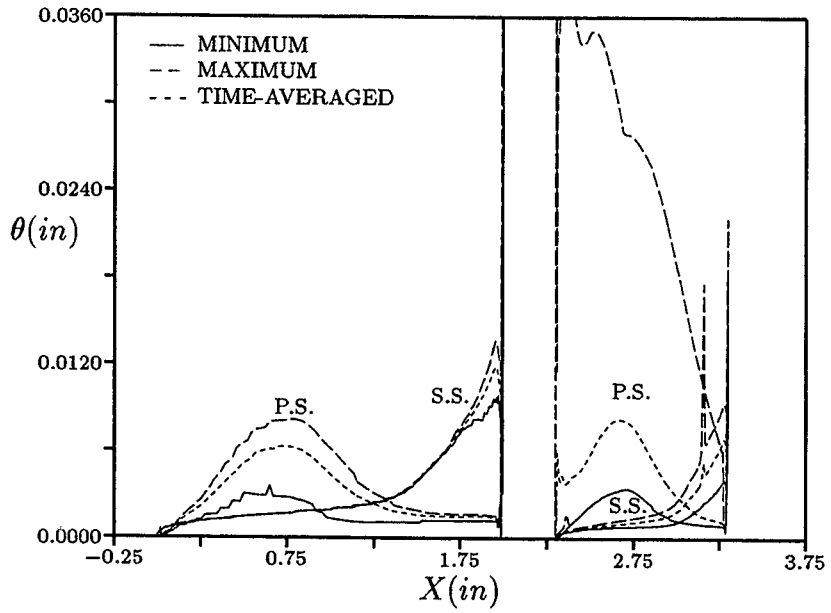

Figure 97: Momentum thickness envelope for the PAK B turbine stage - $Re = 80,000$; B-L, turbulent

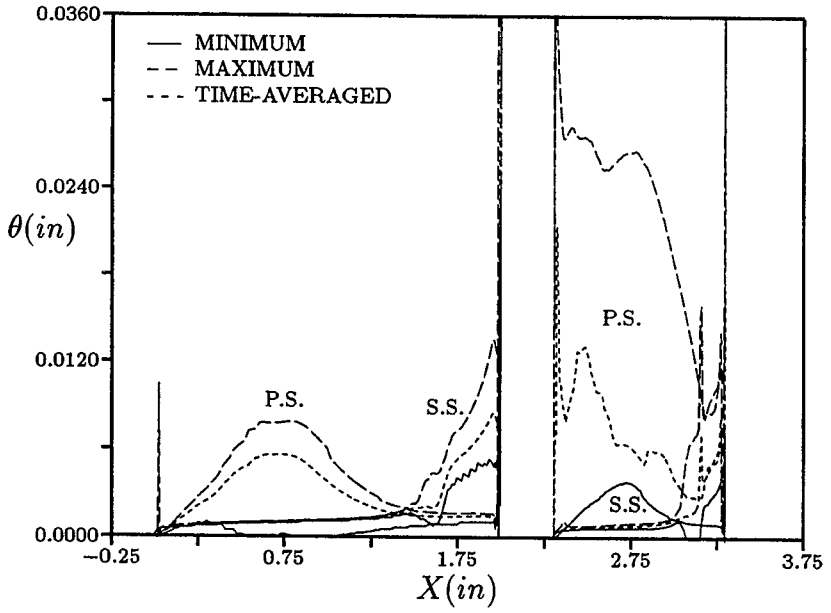

Figure 98: Momentum thickness envelope for the PAK B turbine stage - $Re = 80,000$; B-L, floating transition

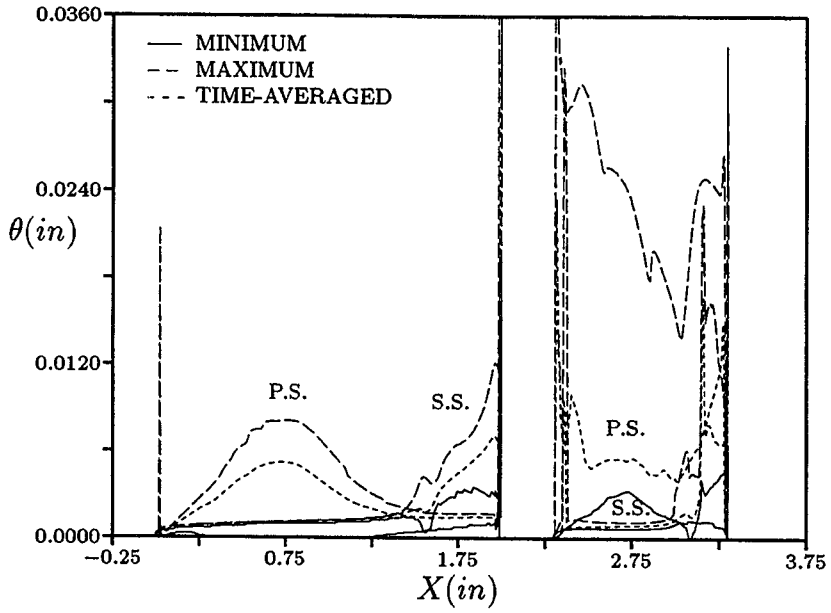

Figure 99: Momentum thickness envelope for the PAK B turbine stage - $Re = 80,000$; B-L, fixed transition

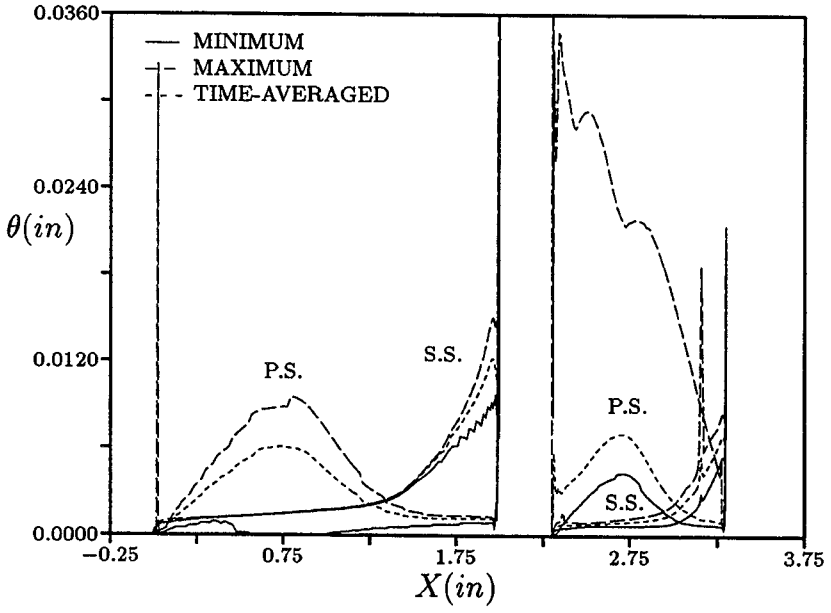

Figure 100: Momentum thickness envelope for the PAK B turbine stage - $Re = 80,000$; $k-\epsilon$ model

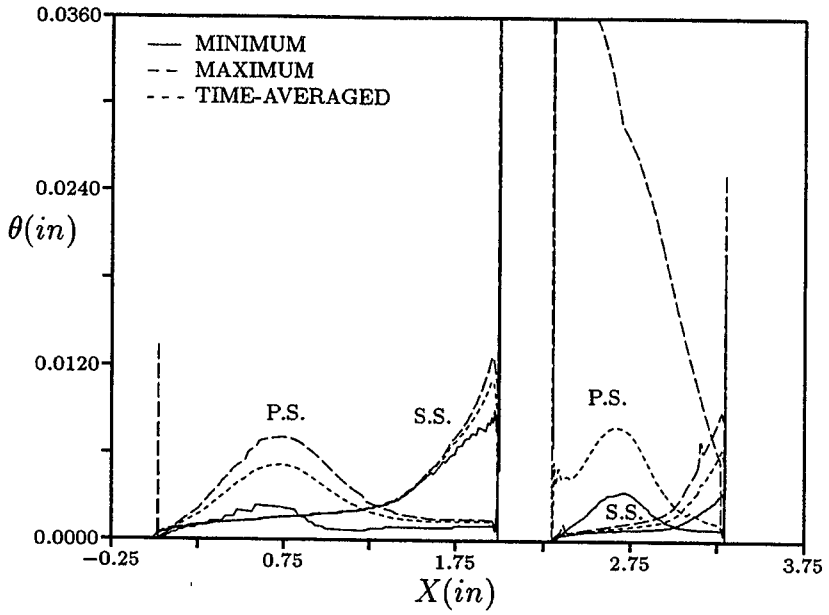

Figure 101: Momentum thickness envelope for the PAK B turbine stage - $Re = 120,000$; B-L, turbulent

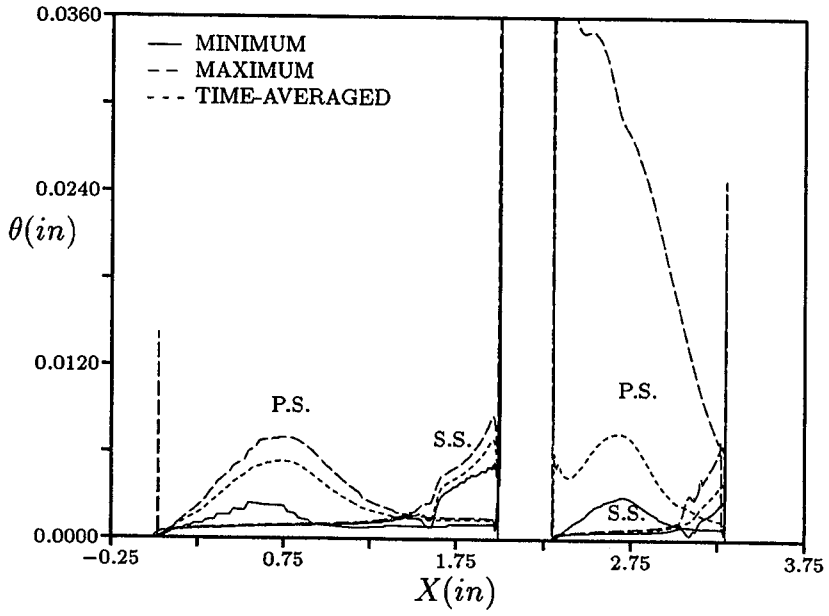

Figure 102: Momentum thickness envelope for the PAK B turbine stage - $Re = 120,000$; B-L, floating transition

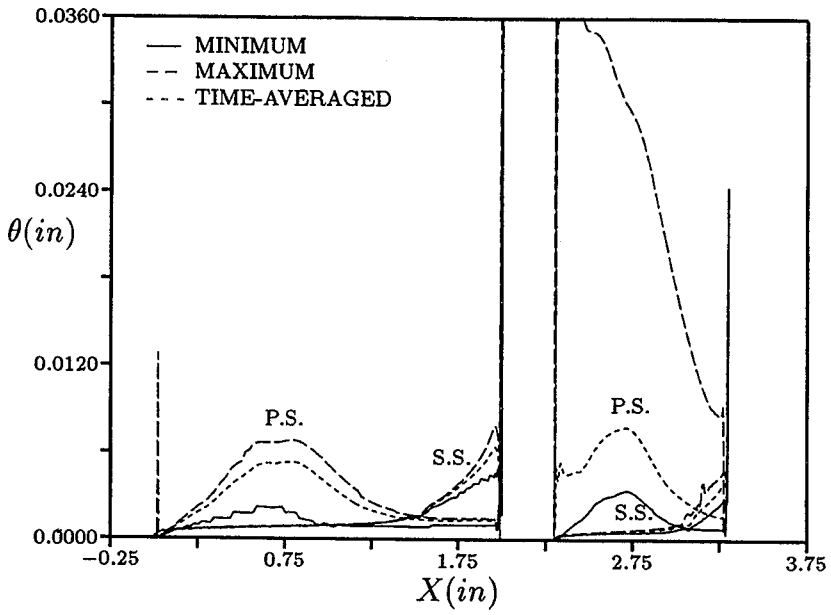

Figure 103: Momentum thickness envelope for the PAK B turbine stage - $Re = 120,000$; B-L, fixed transition

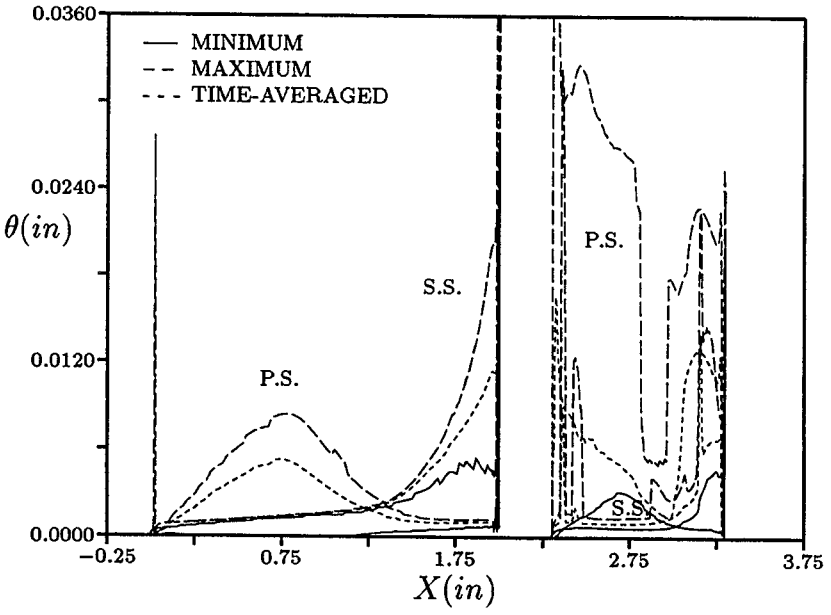

Figure 104: Momentum thickness envelope for the PAK B turbine stage - $Re = 120,000$; $k - \epsilon$ model

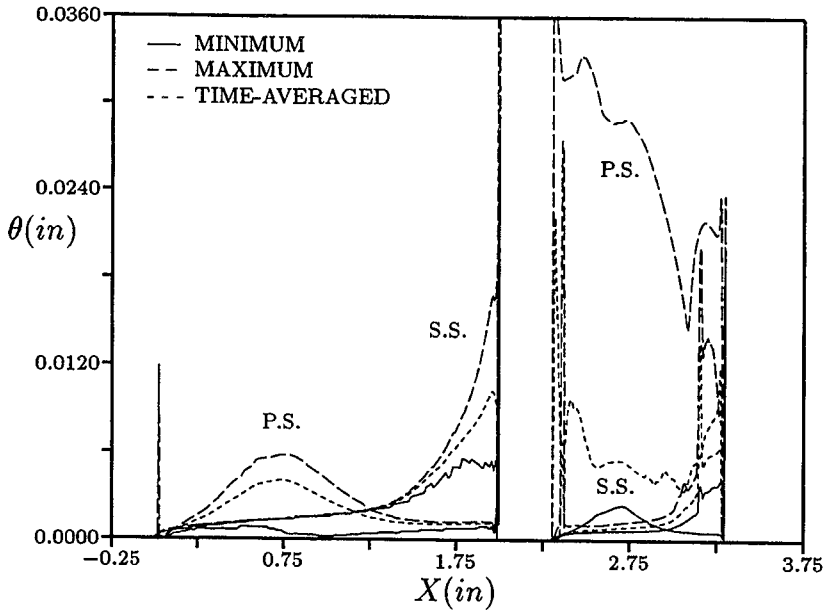

Figure 105: Momentum thickness envelope for the PAK B turbine stage - $Re = 200,000$; B-L, turbulent

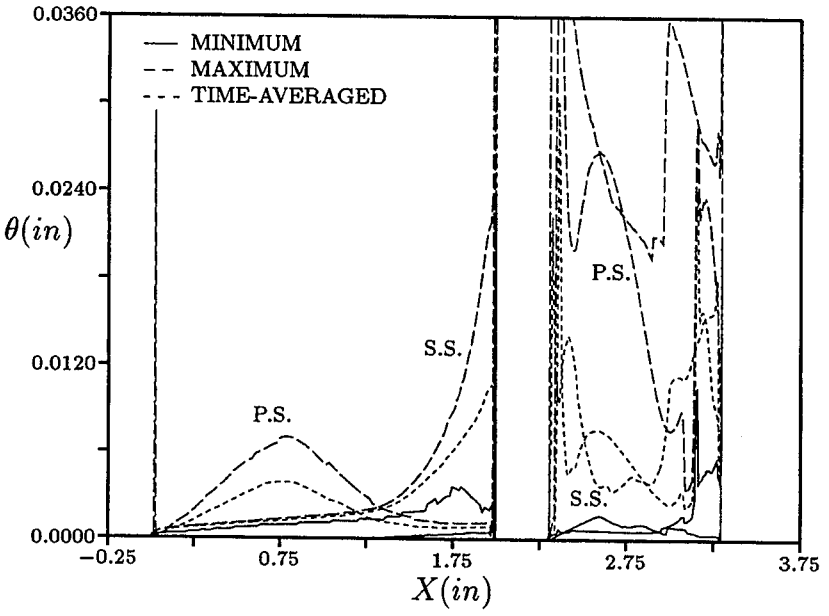

Figure 106: Momentum thickness envelope for the PAK B turbine stage - $Re = 200,000$; $k - \epsilon$ model

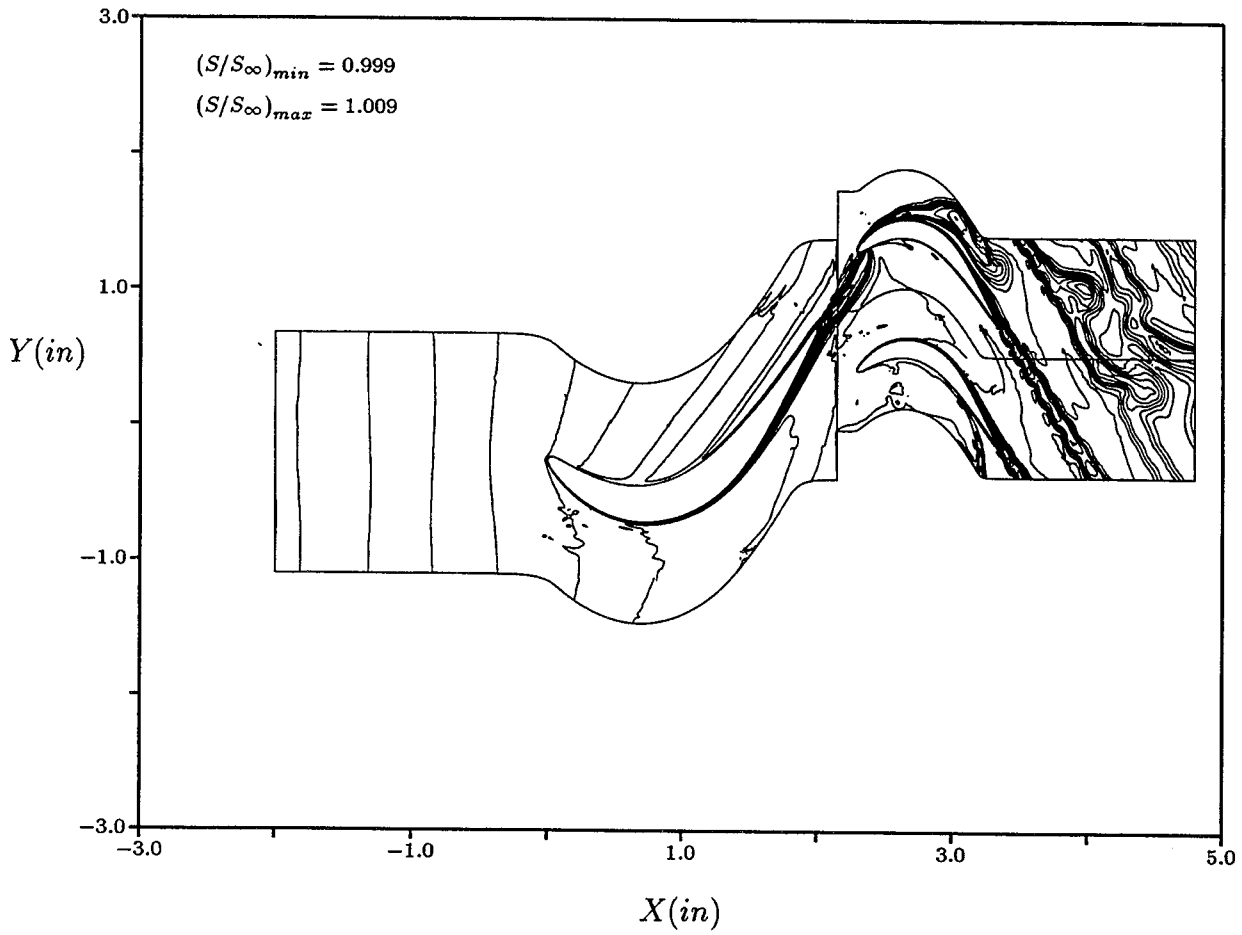

Figure 107: Instantaneous entropy contours for PAK B turbine stage, $Re = 40,000$, turbulent

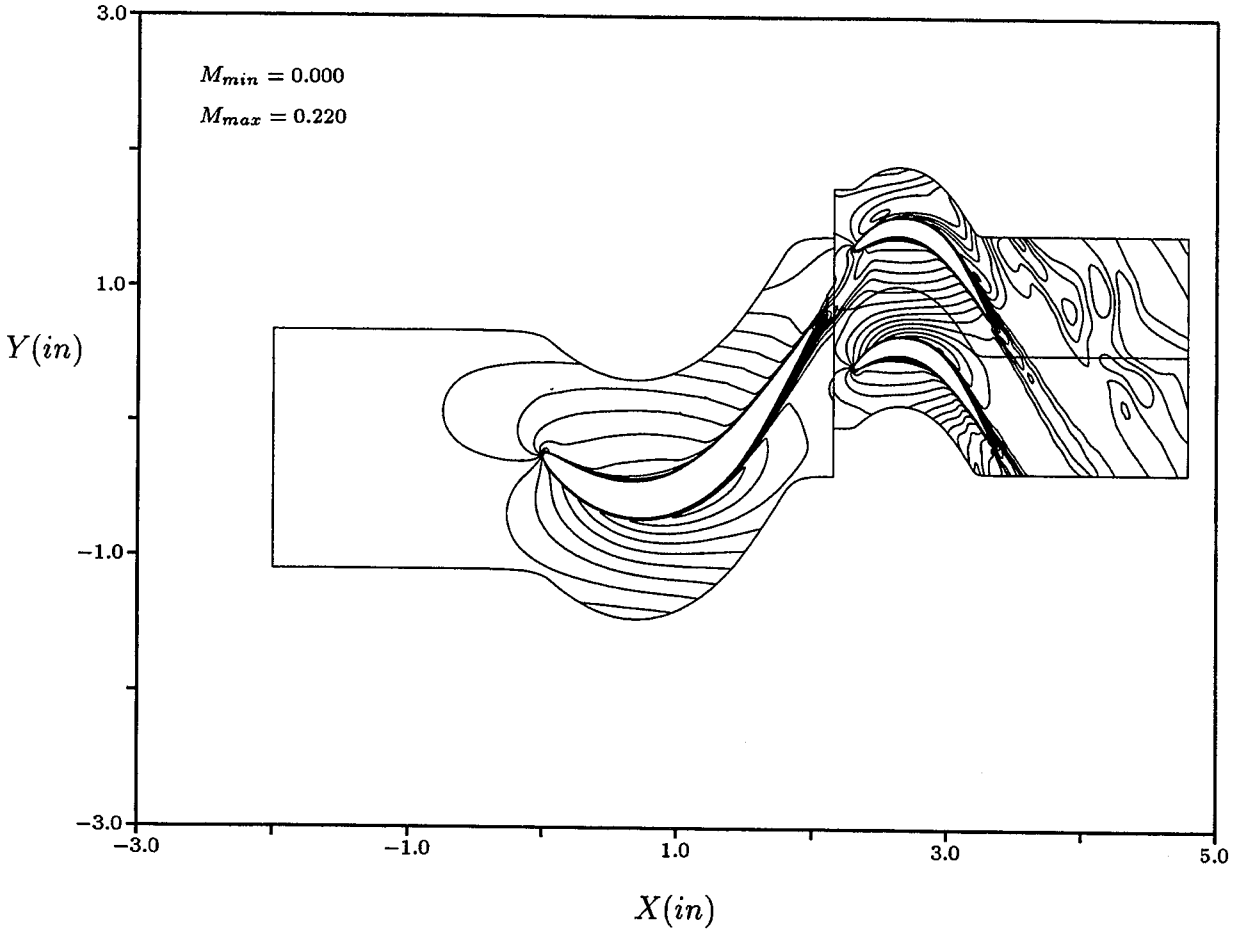

Figure 108: Instantaneous Mach number contours for PAK B turbine stage, $Re = 40,000$, turbulent

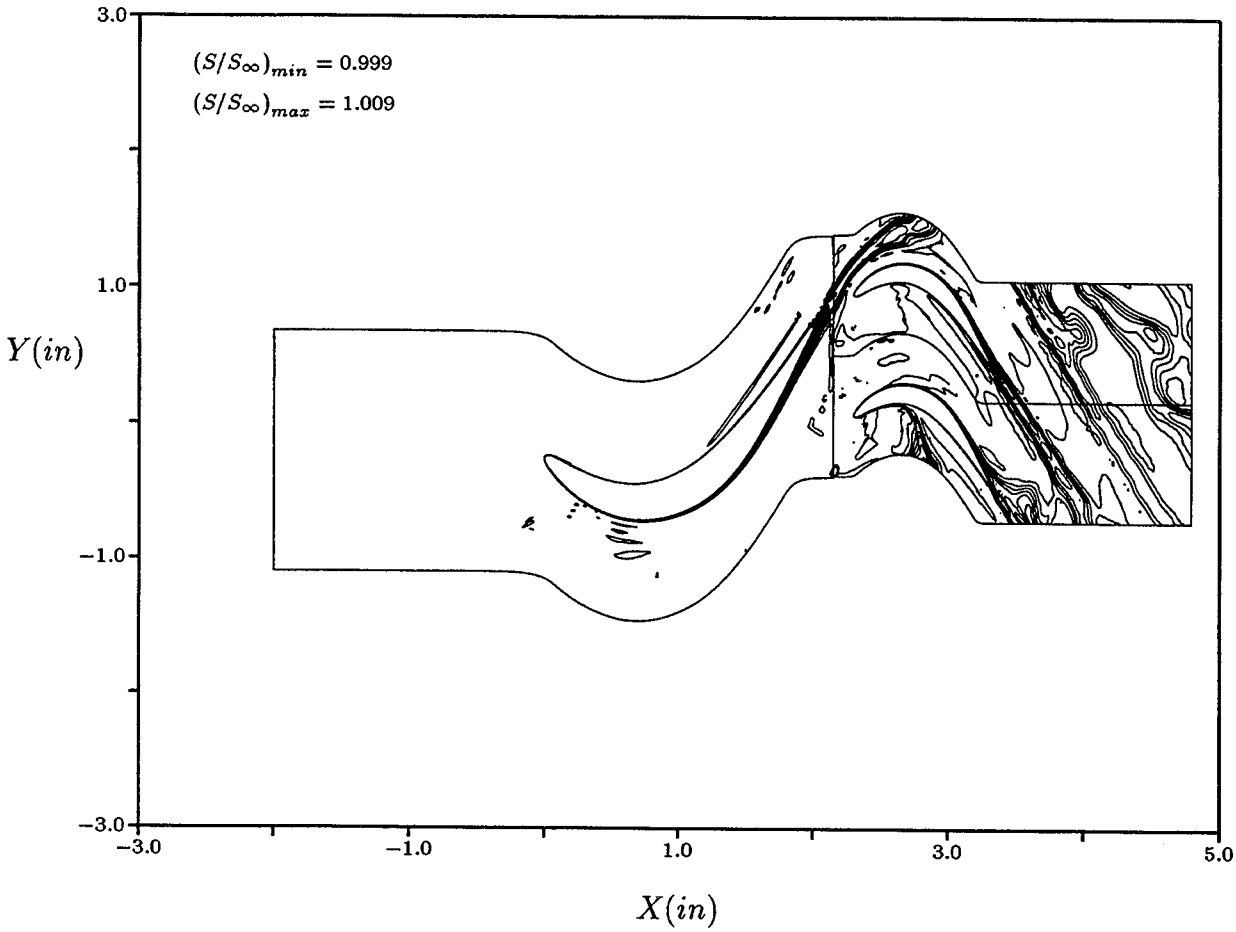

Figure 109: Unsteady entropy contours for PAK B turbine stage, $Re = 120,000$, turbulent

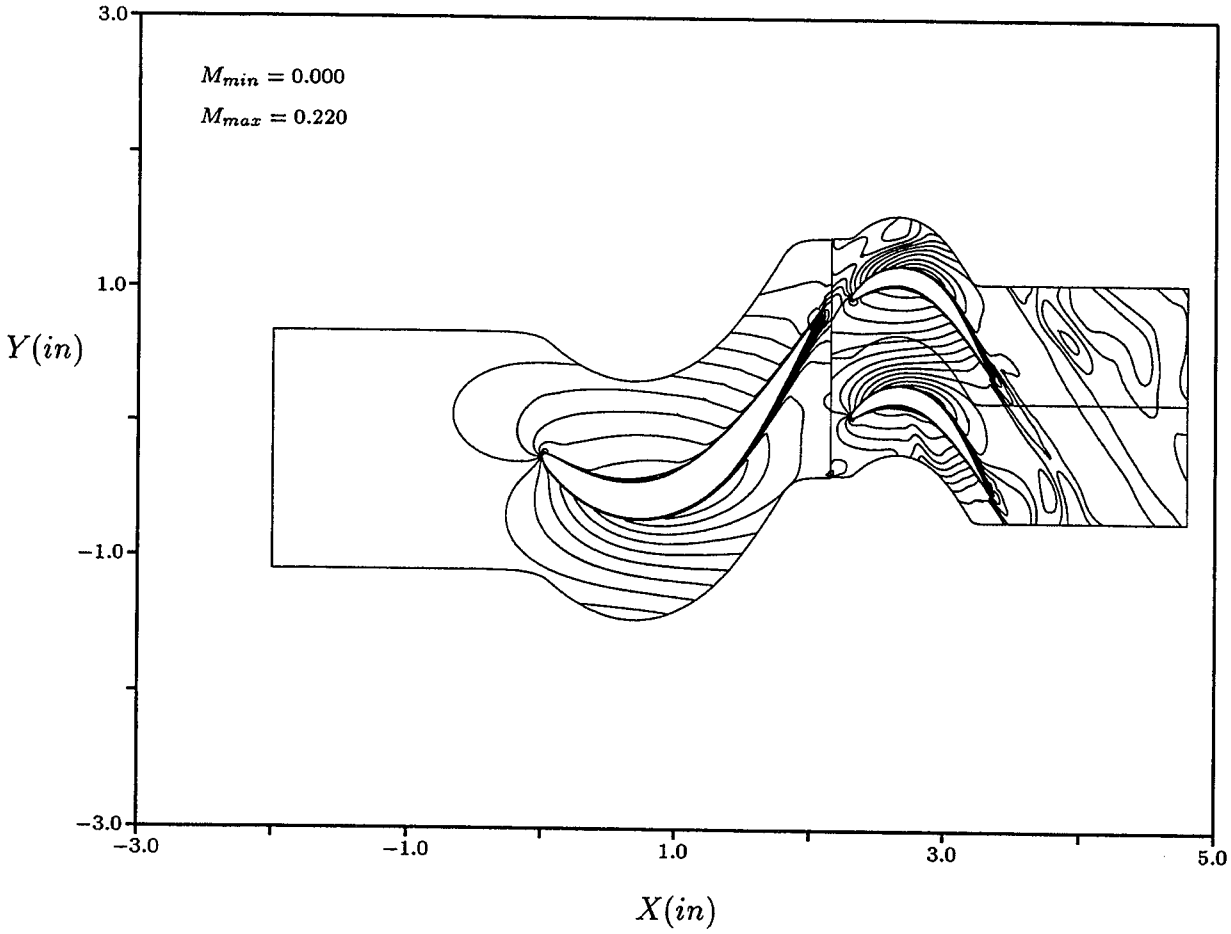

Figure 110: Unsteady Mach number contours for PAK B turbine stage, $Re = 120,000$, turbulent

REPORT DOCUMENTATION PAGE

Form Approved
OMB No. 0704-0188

1. AGENCY USE ONLY (*Leave blank*)	2. REPORT DATE	3. REPORT TYPE AND DATES COVERED
	September 1996	Final Contractor Report

4. TITLE AND SUBTITLE

Reynolds-Averaged Navier-Stokes Studies of Low Reynolds Number Effects on the Losses in a Low Pressure Turbine

5. FUNDING NUMBERS

WU–505–62–52
G–NAG3–1668

6. AUTHOR(S)

Daniel J. Dorney

7. PERFORMING ORGANIZATION NAME(S) AND ADDRESS(ES)

Western Michigan University
Department of Mechanical & Aeronautical Engineering
Kalamazoo, Michigan 49008–5065

8. PERFORMING ORGANIZATION REPORT NUMBER

E–10457

9. SPONSORING/MONITORING AGENCY NAME(S) AND ADDRESS(ES)

National Aeronautics and Space Administration
Lewis Research Center
Cleveland, Ohio 44135–3191

10. SPONSORING/MONITORING AGENCY REPORT NUMBER

NASA CR–198534

11. SUPPLEMENTARY NOTES

Project manager, David E. Ashpis, Internal Fluid Mechanics Division, NASA Lewis Research Center, organization code 2630, (216) 433–8317.

12a. DISTRIBUTION/AVAILABILITY STATEMENT

Unclassified - Unlimited
Subject Category 07

This publication is available from the NASA Center for AeroSpace Information, (301) 621–0390.

12b. DISTRIBUTION CODE

13. ABSTRACT ***(Maximum 200 words)***

Experimental data from jet-engine tests have indicated that unsteady blade-row interaction effects can have a significant impact on the efficiency of low-pressure turbine stages. Measured turbine efficiencies at takeoff can be as much as two points higher than those at cruise conditions. Preliminary studies indicate that Reynolds number effects may contribute to the lower efficiencies at cruise conditions. In the current study, numerical experiments have been performed to quantify the Reynolds number dependence of unsteady wake/separation bubble interaction on the performance of a low-pressure turbine.

14. SUBJECT TERMS

Turbomachinery; Low-pressure turbine; Turbulence modeling; Transition

15. NUMBER OF PAGES

109

16. PRICE CODE

A06

17. SECURITY CLASSIFICATION OF REPORT	18. SECURITY CLASSIFICATION OF THIS PAGE	19. SECURITY CLASSIFICATION OF ABSTRACT	20. LIMITATION OF ABSTRACT
Unclassified	Unclassified	Unclassified	